Fundamental Aspects of Imaging Matrix Assisted Laser Desorption/Ionisation Mass Spectrometry

Sally Jayne Atkinson

A thesis submitted in partial fulfilment of the requirements of
Sheffield Hallam University
for the degree of Doctor of Philosophy

January 2008

ACKNOWLEDGEMENTS

I would like to extend special thanks to my supervisor Prof. Malcolm Clench for his invaluable mentoring, extensive support and for providing opportunities to present my work internationally over the last 3 years.

I gratefully acknowledge sponsorship from RSC/EPSRC. I would like to thank Dr. Paul Loadman of the Institute of Cancer Therapeutics, University of Bradford for his support and provision of samples and Julie Wingate, Lyle Burton and Ron Bonner of Applied Biosystems/MDS Sciex for providing statistical software, software updates and useful information and advice.

I would also like to take this opportunity to thank friends and colleagues who have helped me throughout my PhD. I would like to thank Dr. Karen Warburton, Dr. Brendan Prideaux, Caroline Earnshaw, Tasneem Muharib, David Anderson, Paul Trim and Marie-Claude Djidja who have been extremely helpful and fun to work with. Special thanks to Martin Kirk, Gaynor Slingsby, Lyndsay Morris, Becky Straker, Kate Grant and Keri and Matt Bramford-Hale for their friendship, support and timely distractions from all things mass spectrometry related.

Last but by no means least, I would like to thank my family. Firstly, to Beth and Jack for providing me with motivation to complete my studies, secondly to my extended family for being so supportive throughout my PhD and previous studies. And finally, I would like to especially thank my parents, who have helped me as much as they could in every possible way. I am eternally grateful for their unwavering support and tolerance throughout the duration of my studies.

ABSTRACT

Matrix assisted laser desorption/ionisation mass spectrometry imaging is a recent addition to the existing family of molecular imaging technologies. It has the capacity to map the distribution of molecules within a biological tissue section, without the need for radionuclide or fluorescent labelling procedures.

The primary aim of the work presented in this thesis was to assess the use of a high repetition rate laser for MALDI-MS image analysis by developing methodologies for the detection of a number of different compounds from a variety of biological tissues. Additional investigations include and examination of strategies for normalisation and statistical interpretation of MALDI-MS image data.

The application of a solvent assisted indirect imaging approach for the analysis of drugs in skin is described. Studies have been carried out in order to gauge how the use of a solvent in the blotting process aids the indirect imaging technique. Further experiments have been performed to assess the level of analyte migration induced by incorporation of a sample wetting step.

In a direct tissue imaging experiment the distribution of a prodrug and its active metabolite has been determined in treated tumour tissue. Endogenous markers have been employed to assist in determining correlation between drug activation and hypoxic regions within tumours.

Different methods of data normalisation are investigated for their effects on image data, and statistical evaluation of MALDI-MS acquired image data have been examined in relation to extracting hidden variables from multidimensional image data sets.

CONTENTS

1.0 INTRODUCTION 1

1.1 Biochemical Imaging Sciences 3

1.2 Imaging Techniques 4

1.2.1 Nuclear Magnetic Resonance Imaging 5

1.2.2 Optical Imaging 8

1.2.3 Single Photon Emission Computed Tomography 14

1.2.4 Positron Emission Tomography 15

1.2.5 Whole Body Autoradiography 16

1.2.6 Mass Spectrometry Imaging 17

1.3 Ionisation and Mass Analysis in Mass Spectrometry Imaging 19

1.3.1 SIMS Imaging 21

1.3.2 MALDI-MS Imaging 24

1.3.2 DESI Imaging 27

1.3.5 Mass Analysis in Mass Spectrometry Imaging 29

1.4 Mass Spectrometry Imaging Processes 34

1.4.1 Sample Preparation in Mass Spectrometry Imaging 34

1.4.2 Mass Spectrometry Image Acquisition 36

1.4.3 Image Processing 40

1.4.4 Statistical Evaluation of Mass Spectrometry Image Data 40

1.5 MALDI-MS Imaging Research 41

1.6 Aims of Work 43

1.7 References 44

2 EVALUATION OF A HIGH REPETITION ND:YAG LASER 53

2.1 Introduction 54

2.2 Materials and Methods 58

2.2.1 Materials 58

2.2.2 Methods 58

2.2.2.1 Measuring Laser Spot Size 59

2.2.2.2 Laser Energy 59

2.2.2.3 Pulse Width 60

2.2.2.4 Beam Profile 60

2.2.2.5 Assessing the Effect of Laser Profile on MALDI Imaging 60

2.3 Results 62

2.3.1 Measuring Laser Spot Size 62

2.3.2 Measuring Laser Energy 64

2.3.3 Measuring Pulse Width 64

2.3.4 Measuring Beam Profile 66

2.3.5 Assessing the Effects of Laser Profile on MALDI Imaging 68

2.4 Conclusions 71

2.4 References 72

3 INDIRECT TISSUE IMAGING 73

3.1 Introduction 74

3.2 Materials and Methods 80

3.2.1 Materials 80

3.2.2 Methods 80

3.2.2.1 Assessment of Transfer Efficiency 80

3.2.2.2 Matrix Optimisation 81

3.2.2.3 Assessment of Lateral Diffusion 82

3.3 Results 84

3.3.1 Assessment of Transfer Efficiency 84

3.3.2 Matrix Optimisation 86

3.3.3 Assessment of Lateral Diffusion 90

3.4 Conclusion 92

3.5 References 93

4 MALDI-MS IMAGING FOR PRE-CLINICAL APPLICATIONS 95

4.1 Introduction 96

4.2 Materials and Methods 102

4.2.1 Materials 102

4.2.2 Methods 103

4.2.2.1 Matrix Optimisation 103

4.2.2.2 Detection of Compounds from Tumour Tissue 104

4.2.2.3 Assessing the Effects of DNA Binding on AQ4 Ionisation 104

4.2.2.4 Imaging of AQ4N and AQ4 in Tumours 105

4.3 Results 107

4.3.1 Matrix Optimisation 107

4.3.2 Detection of Compounds Directly from Tumour Tissue 111

4.3.3 Assessing the Effects of DNA Binding on AQ4 Ionisation 114

4.3.4 MALDI-MS Imaging of AQ4N and AQ4 in Tumours 117

4.3.5 Using Endogenous Markers to Define Hypoxic Tissue Regions 122

4.4 Conclusion 125

4.5 References 127

5 PRE-PROCESSING OF MALDI-MS IMAGE DATA 129

5.1 Introduction 130

5.1.1 Analytically Induced Variability 130

5.1.2 Sample Induced Variability 131

5.1.3 Adduct Processes 132

5.1.4 Matrix Coverage and Crystalisation 133

5.1.5 MALDI-MS Image Normalisation 135

5.2 Materials and Methods 137

5.2.1 Materials 137

5.2.2 Methods 139

5.2.2.1 Single Ion Count Normalisation 139

5.2.2.2 Total Ion Count Normalisation 140

5.2.2.3 TIC Normalisation followed by SIC normalisation 140

5.2.2.4 SIC Normalisation followed by TIC normalisation 141

5.2.2.5 Ion Species Specific Normalisation 141

5.2.2.6 Statistical Evaluation of Normalisation Procedures 144

5.3 Results 149

5.3.1 Normalisation of AQ4N Tumour Image Data 149

5.3.1.1 Assessing Linearity of Normalised Data 149

5.3.1.2 Assessing Correlation of Spectra after Normalisation 153

5.3.1.3 Assessing Adduct Relationships after Normalisation 155

5.3.2 Normalisation of Hydrocortisone Treated Skin Image Data 159

5.3.2.1 Assessing Linearity of Normalised Data 159

5.3.2.2 Assessing Correlation of Spectra after Normalisation 163

5.3.2.3 Assessing Adduct Relationships after Normalisation 165

5.4 Conclusion 168

5.5 References 169

6 MULTIVARIATE ANALYSIS IN MALDI-MS IMAGING 170

6.1 Introduction 171

6.1.1 Determining Principal Components to Separate Sample Groups 175

6.1.2 Data Pre-processing for Statistical Image Data Evaluation 179

6.2 Materials and Methods 180

6.2.1 Materials 180

6.2.1.1 Sample Preparation of the Saggital Rat Brain Section 182

6.2.1.2 Sample Preparation of the Drug Treated Porcine Skin 183

6.2.2 Methods 183

6.2.2.1 Extracting Sample Spectra for PCA 183

6.2.2.2 Principal Components Analysis 184

6.2.2.3 Separation of Sample Groups Based on PCA Scores 184

6.2.2.4 Determining Latent Variables in MALDI-MS Image Data 186

6.2.2.5 Assessment of Data Pre-processing for PCA 187

6.3 Results 188

6.3.1 Determining Ions of Interest by PCA 188

6.3.2 Determining Latent Variables in MALDI-MS Image data by PCA 191

6.3.3 Assessment of Hydrocortisone Treated Skin MALDI-MS image 195

6.3.3.1 Evaluating Separation of Sample Groups by PCA 195

6.3.3.2 Assessing the Effects of ISS Normalisation on PCA Results 197

6.3.3.3 Extracting Useful Information form PCA 199

6.4 Conclusions 202

6.5 References 203

7. CONCLUSIONS AND SUGGESTIONS FOR FUTURE WORK 204

8. POSTERS AND PUBLICATIONS 209

TABLE OF FIGURES

Chapter 1

Figure	1.1	The Principle of MRI	7
Figure	1.2	Setup of a Laser Scanning Confocal Microscope	10
Figure	1.3	Diagram of a Simple Mass Spectrometer	18
Figure	1.4	Principle of Secondary Ion Mass Spectrometry	22
Figure	1.5	Diagram of the Principle of MALDI	26
Figure	1.6	Desorption Electrospray Ionisation	28
Figure	1.7	Schematic Representation of Delayed Ion Extraction	30
Figure	1.8	Reflectron TOF Mass Analyser	31
Figure	1.9	Schematic of Applied Biosystems/MDS Sciex Q-Star Pulsar *i*	33
Figure	1.10	Mass Spectrometry Image Acquisition	37
Figure	1.11	Acquiring Ion Images in Mass Microscope Mode	39

Chapter 2

Figure	2.1	Measurements of Laser Spot Dimensions	63
Figure	2.2	Laser Pulse Width Traces	65
Figure	2.3	Laser Beam Profile Images	67
Figure	2.4	Comparing MALDI-MS Imaging Modes	69
Figure	2.5	Assessing Sensitivity as Image Resolution Increases	70

Chapter 3

Figure	3.1	The Chemical Structure of Hydrocortisone	78
Figure	3.2	Transfer Efficiency and Solubility of Hydrocortisone	85
Figure	3.3	Detection of Hydrocortisone on Spot Targets	87
Figure	3.4	Detection of Hydrocortisone on Cellulose Membranes	88
Figure	3.5	Detection of Hydrocortisone on Cellulose Membrane Blots	89
Figure	3.6	Hydrocortisone Lateral Diffusion Images	91

Chapter 4

Figure	4.1	Chemical Structures of AQ4N and its Major Metabolites	101
Figure	4.2	Evaluation of Matrices for Analysis of AQ4N and AQ4	108
Figure	4.3	AQ4N and AQ4 Detection with α-CHCA Matrix	109
Figure	4.4	AQ4N and AQ4 Detection with DHB Matrix	110
Figure	4.5	AQ4N Detection on Tumour Tissue Using α-CHCA	112
Figure	4.6	AQ4 Detection on Tumour Tissue Using α-CHCA	113
Figure	4.7	The Effects of DNA and pH on AQ4 Detection	115
Figure	4.8	The Effects of TFA on AQ4 and α-CHCA Ion Signals	116
Figure	4.9	MALDI-MS Images of Drug Spiked Tissue with 0.1% TFA	118
Figure	4.10	MALDI-MS Images of Drug Spiked Tissue with 2.0% TFA	119
Figure	4.11	Distribution of AQ4N and AQ4 in Treated Tumour Tissue	121
Figure	4.12	Images of the Distribution of ATP in an AQ4N Treated Tumour	123
Figure	4.13	Bicolour Images of the Distribution of AQ4, AQ4N and ATP	124

Chapter 5

Figure	5.1	Determining Ion Species	143
Figure	5.2	Representative *x,y* Scatter Plots for the Assessment of AQ4N Tumour Data	151
Figure	5.3	Average Gradients of AQ4N Tumour Spectra Before and After Normalisation	152
Figure	5.4	Pearson Product-moment Correlation Coefficient Evaluation of AQ4N Tumour Data	154
Figure	5.5	Assessing the Relationship Between Adduct Processes in AQ4N Tumour Data	157
Figure	5.6	Assessing Ion Intensity Patterns for Phosphotidylcholine Adducts in AQ4N Tumour Data	158
Figure	5.7	Representative *x,y* Scatter Plots for the Determination of Linearity of Hydrocortisone Treated Skin Data	161
Figure	5.8	Average Gradients of Hydrocortisone Treated Skin Spectra Before and After Normalisation	162
Figure	5.9	Pearson Product-moment Correlation Coefficient Evaluation of Hydrocortisone Treated Skin Data	164
Figure	5.10	Assessing the Relationship Between Adduct Processes in Hydrocortisone Treated Skin Data	166
Figure	5.11	Assessing Ion Intensity Patterns for Phosphotidylcholine Adducts in Hydrocortisone Treated Skin Data	167

Chapter 6

Figure 6.1 PCA of Viagra and Placebo Tablet Data

Figure 6.2 Principal Components Separating Sample Groups

Figure 6.3 Assessing Separation of Groups by PC Score Range

Figure 6.4 Principal Components Scores Plots for the Brain Image Data

Figure 6.5 Principal Components Loadings Plot for the Brain Image Data

Figure 6.6 Distribution of Ions of Interest in the Rat Brain Sagittal Section

Figure 6.7 The Effects of ISS Normalisation on Sample Grouping

Figure 6.8 The Effects of ISS Normalisation on PCA Results

Figure 6.9 Selecting Ions of Interest by PCA

Figure 6.10 Images of Ions of Interest Selected by PCA

ABBREVIATIONS

°C	degrees centigrade
µg	microgram
µm	micrometre
BLI	bioluminescence imaging
CLA	cluster analysis
cm	centimetre
DA	discriminant analysis
DART	direct analysis in real time
DESI	desorption electrospray ionisation
DHB	2,5-dihydroxybenzoic acid
DIOS	desorption/ionisation on silicon
DNA	deoxyribonucleic acid
FA	factor analysis
g	gram
HABA	2-(4-hydroxyphenylazo) benzoic acid

HPA	3-hydroxypicolinic acid
ISS	ion species specific
KHz	kilohertz
L	litre
LC-MS	liquid chromatography mass spectrometry
LMIG	liquid metal ion gun
MALDI	matrix assisted laser desorption/ionisation
ME-SIMS	matrix enhanced secondary ion mass spectrometry
mg	miligram
mm	millimetre
MRFM	magnetic resonance force microscopy
MS	mass spectrometry
Nd:YAG	neodymium-doped yttrium aluminium garnet
NMRI	nuclear magnetic resonance imaging
PCA	principal components analysis
PET	positron emission tomography
PMCC	Pearson product-moment correlation coefficient

Q-TOF	quadrupole time of flight
RF	radiofrequency
SIC	single ion count
SIMS	secondary ion mass spectrometry
SPECT	single photon emission computed tomography
TFA	trifluoroacetic acid
TIC	total ion count
TOF	time of flight
UV	ultraviolet
α-CHCA	alpha-cyano,4-hydroxycycinnamic acid

CHAPTER 1

Introduction

1.0 Introduction

Living organisms as a whole are the most complex structures in the known universe and their intrinsic mechanisms and interactions have always fascinated man. Over the past few centuries, man's understanding of the complexities of biological systems has increased substantially. One of the most powerful tools used to gain this knowledge has been the generation of images.

The study of living organisms has historically relied on the view and illustration of biological systems. From Vesalius' early studies of human anatomy[1] to molecular structure elucidations at the atomic level, the most practical sense of acquiring and relaying information has been through visualisation and representation as an image. As a result, many techniques have been developed to allow researchers to look at organisms in different ways.

During the 20th century, biological examinations were directed toward the determination of tissue and cellular anatomy. This was promoted through the advent of electron microscopy in the early 1930's.[2] Later with the discovery of the DNA double helix, a new generation of research was born. The mapping of the genome transformed the way that living organisms are considered.

With greater depth in understanding of the underlying complexity of biological systems, researchers have begun to look at living organisms from a very different perspective. Where the traditional methods of biological study determine the gross structure and organisation of tissues and cellular components, the latest innovations in biomedical imaging are directed toward examining the distribution of the molecules within. The ability to see biochemical or biological events as they occur in situ has been pivotal to many areas of scientific research.

1.1 Biochemical Imaging Sciences

Insight into biochemical systems from the anatomic to the subcellular level is now the basis of developmental, pathological, and pharmaceutical research. Both in medicine and research images are often generated to determine biochemical processes, either by tracking the path or by mapping the distribution of certain natural or synthetic chemical entities.

Molecular imaging is a broad title given to a number of techniques that are concerned with the production of images of molecular distribution in tissues and cells. Here the principles and applications of the basic biomedical imaging technologies are examined.

1.2 Imaging Techniques

Images are an effective means of storing and displaying high volumes of information. Molecular images are created through recording the detection of signals from defined points within a sample. The signal responses are stored along with their co-ordinate of spatial origin within the sample. These data can then be processed and represented in the form of a digital image. In an image, the intensity of the signal response for each specific pixel is defined by a change in brightness, or alternatively by a change in colour or hue.

The amount of data collected for each pixel is defined by the number of different signal responses measured in the analysis. This is broadly governed by the type of imaging technique employed. Imaging techniques can also provide three dimensional image data. This is achieved by acquiring signals from a series of sequential two dimensional slices and digitally joining the slices of data together to form a volumetric image set.

The imaging systems available vary in invasiveness. They also differ in resolution, penetration depth, acquisition time, sensitivity and specificity. Clearly, the invasiveness of the imaging technique largely defines its application. Some techniques are relatively harmless and can be carried out on living subjects with little preparation or serious side-effects. These techniques tend to be applied in medicine as diagnostic technologies.

Some techniques require labeling procedures or administration of contrast agents to promote signal responses. Others require procedures which are harmful or cause destruction of the organism under examination. These techniques tend to be reserved primarily for laboratory research purposes.

Whilst many imaging modalities tend to focus on acquisition of one or a few different signal responses, some carry the potential to detect a broad spectrum of signals simultaneously. With the rate at which scientific knowledge is growing, these techniques are becoming increasingly popular in research.

The non-invasive molecular imaging modalities that may be carried out on living cells or tissues include nuclear magnetic resonance imaging, some forms of optical imaging, single photon emission computed tomography and positron emission tomography.

Invasive imaging technologies involving harm or destruction to samples include some forms of optical imaging, autoradiography and most forms of mass spectrometry imaging.

1.2.1 Nuclear Magnetic Resonance Imaging

Nuclear magnetic resonance imaging (NMRI), commonly referred to as magnetic resonance imaging (MRI), is a non-ionising radiation technique. It is widely regarded as one of the most powerful non-invasive imaging technologies available in clinical diagnostics and biomedical research.

MRI has the ability to distinguish between two fundamentally similar, but not identical tissue types. The technique is routinely used by clinicians to evaluate demylinating disorders and for the detection of pathological tissues such as tumours. Additional related approaches include functional MRI and magnetic resonance angiography. These are used for the assessment of neural activity and stenosis respectively. MRI is further applied in medical interventions such as radio and ultrasound therapy to provide navigational guidance for the therapist during the course of treatment.

In MRI, absorption and emission of energy in the radiofrequency range of the electromagnetic spectrum creates detailed tomographic or volumetric images. The technique is based on the principle of spin properties of various atoms when subject to electromagnetic forces.

Images are generated from nuclear magnetic resonance signals and are usually obtained using the spin property of the hydrogen atoms in the tissue. As hydrogen content varies between tissues, adaptation of pulse sequences can produce contrasting signals between various tissues types. As a magnetic field is applied, hydrogen protons become almost equally aligned (B_0) or counter aligned with the magnetic field. B_0 alignment is slightly favoured as the nucleus is at lower energy in this position. As a result there is a net magnetisation pointing in the direction of the B_0 field. B_1 RF pulses are applied to force the protons to spin away from B_0 at an angle of 90° (figure 1.1).

The direction of net magnetization is, over time, altered to align with the B_1 field. It is in this conformation that the radio frequency signal can be detected. As the RF pulse is removed, the protons return to their original B_0 alignment. This is known as relaxation. The energy released as the protons return to the original state acts as a response signal. The signals detected are converted through Fourier transform to produce images.

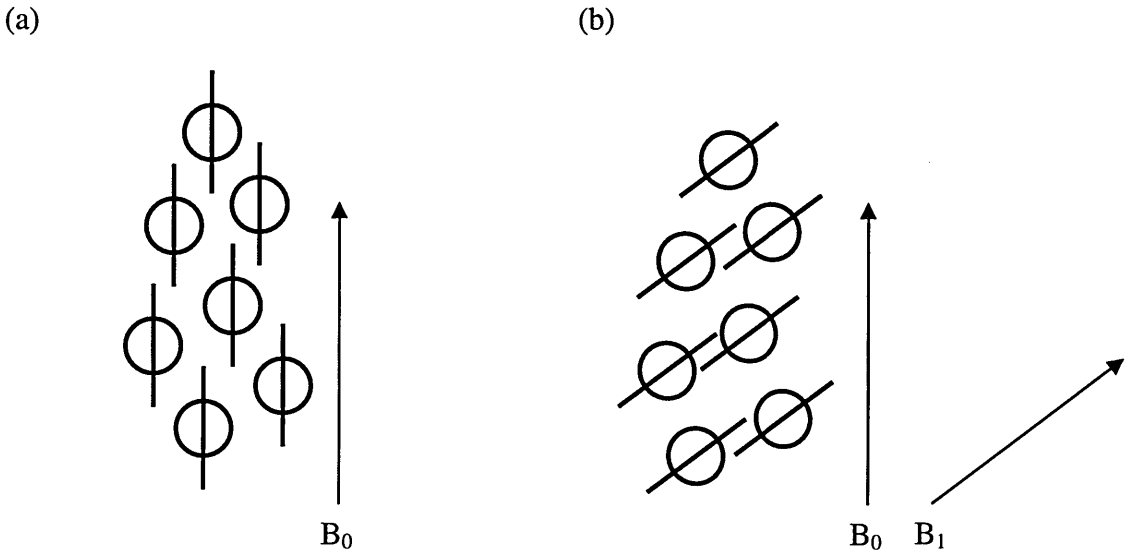

Figure 1.1 The principle of MRI

In a strong magnetic field (B_0) the hydrogen nuclei precess about the direction of the field (a). The radio frequency pulse realigns the magnetic moment to the B_1 direction. During relaxation, once the RF pulse is removed, the hydrogen nuclei return to B_0. The loss in nuclear energy as the protons return to the original state, produces a measurable RF signal that can be used to produce an image.

Resolutions of approximately $1mm^3$ are routine in clinical diagnostics. This is in accordance with the requirements of current medical applications. With the latest adaptation of MRI which incorporates some attributes of atomic force microscopy, image voxel sizes in the region of 1μm are possible. Using this technique, known as magnetic resonance force microscopy (MRFM), images may be produced where a single cell contains approximately 1,000,000 image voxels.[3, 4] The most recent reports of high resolution MRFM boast resolutions of 20nm.[5]

High resolution MRI is used in research as a non-invasive approach for in vivo studies. High spatial resolution and high anatomical contrast combined with the ability to label cells with MR contrast agents allows mapping of microscopic events such as cellular migration. This method has been influential in assessing the pathogenecy of a number of diseases. [6]

1.2.2 Optical Imaging

Optical imaging is the name given to a number of non-ionising imaging techniques. They are based on various physical parameters of light interaction with tissues or molecules. These techniques can be used to determine structural properties as well as chemical and functional changes within tissues. There are a number of optical in vivo and in vitro imaging systems that are currently used in research. Each varies in penetration depth, resolution and application.

Confocal Microscopy

Confocal Microscopy can be used as a stand alone technique or more specifically with fluorescent markers. The latter allows mapping of the relative distribution of specific molecules throughout cells and tissues.

In contrast to wide-field optical microscopy where the whole sample is illuminated simultaneously, confocal microscopy uses a focused beam of light to raster across the sample. Because the technique uses focal point scanning, the depth of analysis can be altered. By performing multiple depth scans of a sample using this technique it is possible to form high resolution 3-dimensional images of microscopic scale biological structures. The basic instrumental setup of a confocal microscope is shown in figure 1.2.

Conventional confocal microscopy can image both fixed and living specimens to a depth of approximately 200 μm, but with new developments of passive pre-dispersion compensation systems, the penetration depth can be extended to 800 μm.[7] In research confocal microscopy is often applied in assessing morphological changes in cell and tissue structures as well as mapping molecular expression through fluorescence microscopy.[8, 9]

In medical applications the use of confocal microscopy is investigated as an endoscopic imaging technology. Using this technique, high resolution cross-sectional images of the gastrointestinal epithelium can be obtained. It is hoped that this approach may provide a means of direct tissue diagnosis, reducing the need for further biopsy screening.[10]

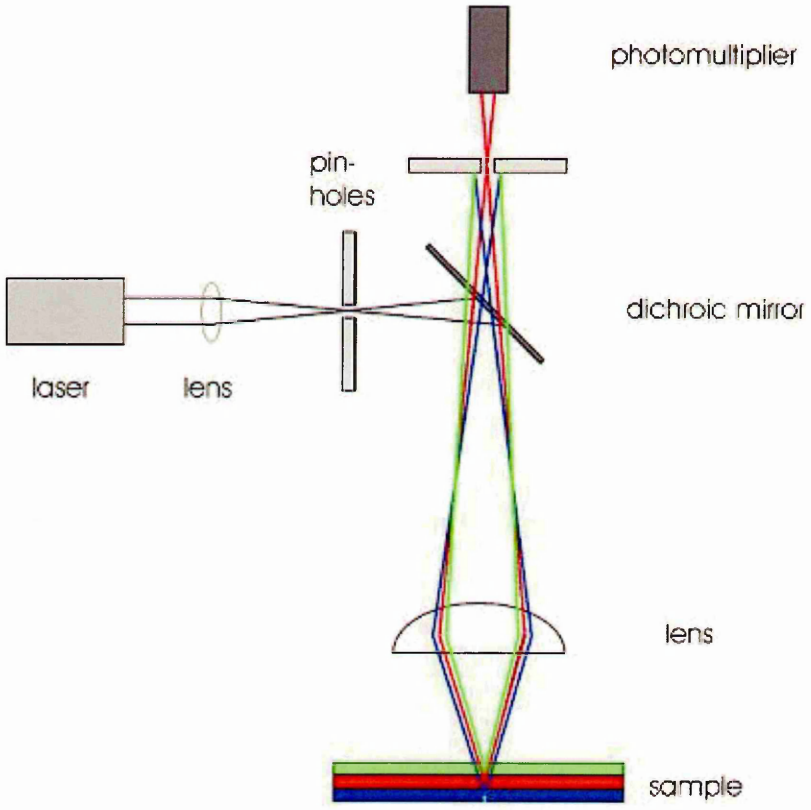

Figure 1.2 Setup of a Laser Scanning Confocal Microscope

The laser beam is focussed into the sample. Electronic lenses and appertures are used to ensure that only fluorescent light from the focal plane is allowed to reach the photomultiplier and be detected. Fluorescence is only detected from small areas of the sample (the confocal point). The sample is scanned to produce a full fluorescence image. Because of the focal point scanning method employed, the penetration depth of analysis can be altered and 3 dimensional images can be produced.[11]

Two-photon Microscopy

Similar to confocal microscopy, two-photon microscopy can also be used to study cells in their natural environment. Two-photon microscopy is another non-invasive optical imaging technique that has the benefit of greater depth penetration than confocal. The increased depth penetration is achieved through reducing light scattering by use of longer wavelengths in the excitation process.[12] Conventionally tissue depth penetration is in the region of 700 μm,[13-16] but this may be increased to 1mm by using a regenerative amplifier.[17] As such this method of analysis is conventionally used to assist in research of in vivo studies on small animal models.

Two-photon microscopy, like confocal imaging, can incorporate fluorescence to allow specifically targeted analysis. Injection of dyes into the blood stream for vascular labeling can allow measurement of blood flow to organs.[14, 18] Labelling of specific components such as proteins or genes can allow mapping of cell migration and gene expression. Cells may also be labeled ex vivo and introduced back into animal models for study.[19]

Fluorescence and Bioluminescence Imaging

As already described, fluorescent and bioluminescent techniques are used as an investigative measure for invivo studies. For the most part they are confined to laboratory research applications. These techniques are widely applied in studying animal models of human disease, in assessing pathological effects of pharmaceuticals on target tissues and for evaluating in vivo pharmacokinetics and drug target binding affinities.

Fluorescence imaging involves the detection of photons emitted when a fluorophore interacts with an incident photon. The wavelengths of the photons emitted when a fluorophore electron returns to the ground state are specific to the given fluorophore entity.

Fluorescent probes can be used to label single or multiple molecular species. Antibodies are targeted to molecular analyte components and then conjugated with fluorescent molecular labels. Multispectral fluorescence imaging can be carried out where several molecular species can be detected in the same image. This is achieved by use of a number of discrete antibody targets each with specific fluorescent label conjugates. The various fluorescent tags are distinguished by a change in colour in the final image through means of the difference in emission wavelength of each given flourophore.

Fluorescence microscopy is often carried out by means of wide-field, two-photon emission or confocal microscopy. With the high image resolution, rapid acquisition timescale and three dimensional abilities of the confocal and two-photon emission microscopy approaches, this technique holds the potential for dynamic live-cell imaging.[20]

Bioluminescence imaging (BLI) enables the visualisation of genetic expression and physiological processes at the molecular level. It is widely used in the study of tumour cell growth and clearance; in assessing the effects of chemotherapeutics on tumours;[21] in tracking immune system cells, in observing bacterial[22, 23] and fungal infections[24]; and in tracking gene expression in living animal models.[25]

Like fluorescence, BLI measures the emission of visible photons at specific wavelengths. In this technique however, no external light source is required. Photons are emitted as a result of energy dependant reactions catalysed by luciferase enzymes on the luciferin substrate. In contrast to fluorescence imaging, there is no background light signal emission from naturally fluorescent entities. This means that BLI can detect light emission at a much lower level. The luciferin substrate is incorporated into cells, organisms and genes through the process of genetic transfection. Consequently BLI is unlikely to find application in human studies.

Both fluorescence and bioluminescence imaging are often employed in small animal studies, using a continuous wave light source (for fluorescence imaging) and a charge-coupled device camera. Localisation of fluorescent or bioluminescent emissions can be obtained to penetration depths of ~7mm (fluorescence) to ~3cm (bioluminescence).[26] As the proximity of contrast agents to the surface affects signal intensity, these applications may only realistically be regarded as a semi quantitative measure.

1.2.3 Single Photon Emission Computed Tomography

Single photon emission computed tomography (SPECT) is used as a diagnostic technique. It is based on the principles of conventional nuclear imaging, where a radionuclide is introduced into the body. A scintillation detector is used to record tomographic images of radionuclide distribution. The radionuclides are often bound to a complex that will act as tracer within the body. These complexes are specifically targeted toward the type of tissue or cells to be assessed.

In terms of application, SPECT is used primarily for measuring blood flow to the brain, heart and other organs. It can provide a more informative diagnosis of ischemia and organ function than can be obtained using MRI. In more detailed research applications SPECT is used to map brain metabolism and function.[27] SPECT has also been assessed for the application of evaluating post-operative organ function.[28]

In laboratory research applications SPECT is often used to assess the viability of new therapeutic agents. The use of therapeutic agents evaluated by this method tends to be those which affect blood flow to organs and/or neuronal function.[29] Alternatively it may be used to map the targeting specificity of a therapeutic agent by nuclide labeling of the drug itself.[30]

1.2.4 Positron Emission Tomography

Positron emission tomography (PET) is a nuclear medicine medical imaging technique that can be used to produce three-dimensional images of various functional processes within the body. It is often used in oncology to map tumours and metastases and make decisions about treatment and prognosis.[31] It is also used as a method to evaluate various neurological diseases.[32] Recently the use of PET has been evaluated for investigating rheumatoid arthritis.[33] In research PET is used as an investigative measure for clinical trials to assess the changes induced by therapeutic interventions such as anti-cancer drugs. It can be used to trace gene expression, angiogenesis and apoptosis.[34]

The method is based on the observance of short-lived radioactive tracer isotopes. As the radio isotope undergoes decay, positrons are emitted. These collide with local electrons to produce a pair of gamma photons. It is these photons that are detected by a photomultiplier to produce a response signal. Instrumentation for PET imaging carries resolutions of approximately 5 mm. Recent advances have increased the resolution to in the region of 1 mm. This is of particular benefit in clinical resaerch where high resolution images are required for applications such as small animal brain imaging. [35]

1.2.5 Whole Body Autoradiography

Whole body autoradiography is very similar to other radionuclide imaging technologies. It differs in the fact that images of the pattern of nuclide decay emissions are produced on an x-ray film or nuclear emulsion as opposed to a digital image. This technique is used in evaluation of natural metabolic pathways and also in the metabolism of therapeutic agents.

For studies of metabolic pathways, radiolabelled transport; enzyme; or receptor inhibitors are often administered to small animal models. These can be used to localise or determine changes in metabolism. In terms of assessing drug metabolism and evaluating drug targeting, therapeutic compounds are radiolabeled and administered to small animal models.[36]

For the process of whole body autoradiography, whole body sections of deceased animals are subjected to analysis. The pattern of radionuclide emissions can be quantitative for the distribution of the radiolabelled components. Whilst this technique can provide quantitative information about the localisation of a drug or metabolic effect, it may not possess sufficient specificity to discriminate between a drug and all of its metabolites.

1.2.6 Mass Spectrometry Imaging

Mass spectrometry imaging is very different from any of the techniques previously described. Not only may it allow simultaneous mapping of a broad spectrum of biological and chemical entities, it can in most cases achieve this without the need for a target labeling procedure. It has the ability to identify molecules over a broad mass spectrum with high sensitivity and molecular specificity.

There are several means of acquiring a mass spectrometric image that are defined by the mode of ionisation from a solid state sample employed. These techniques are still in the development phase for application as imaging technologies and differ in mass range, sensitivity and image resolution.

Conventional mass spectrometry is used in both routine and research applications of biotechnology, drug discovery, environmental health, chemical engineering and clinical diagnostics. It is an invaluable analytical tool which is used to measure the mass of molecular and elemental ions and the intensity of their signal. It is applied in studies of molecular characterization and structural elucidation, and is also used for qualitative and quantitative assessment of sample compositions.

The basic principle of mass spectrometry is defined by the ionisation of elements or molecules and their separation and detection according to charge and molecular or atomic mass.

Mass spectrometers can be divided into three fundamental parts, the ionisation source, the mass analyser, and the ion detector. These are illustrated in figure 1.3.

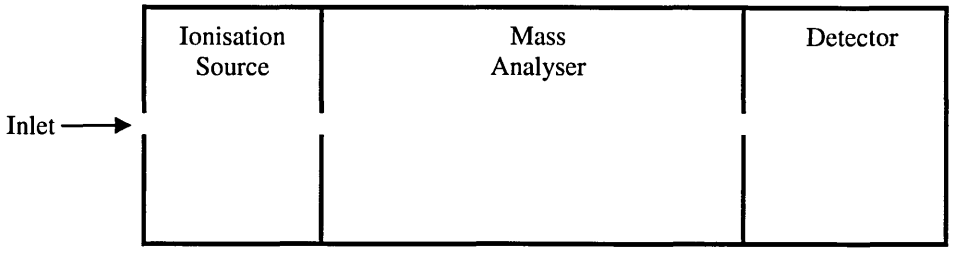

Figure 1.3 Diagram of a Simple Mass Spectrometer

Samples are introduced into the ion source where they undergo the process of ionisation. The ions are then accelerated into the mass analyser where they are separated on the basis of their mass (m) to charge (z) ratio (m/z). The separated ions are detected and the m/z information as well as the signal intensity is recorded.

Advances in desorption ionisation techniques from a sample surface has allowed mass spectrometry to be applied as an imaging technique.[37-39] Mass spectrometry based surface analysis has become an important technique in materials science. It was first introduced in the biological field using secondary ion mass spectrometry and has more recently begun to employ the use of matrix assisted laser desorption/ionisation as well as other newly developed ionisation techniques.

Mass spectrometry imaging will form the focus of this thesis. In the remaining sections of this chapter the fundamental aspects of mass spectrometry imaging techniques are examined and the practical considerations associated with the application of each approach are evaluated.

1.3 Ionisation and Mass Analysis in Mass Spectrometry Imaging

The biological application of mass spectrometry imaging has advanced significantly over the last decade. It is becoming an important tool for studying the distribution of various target compounds in cells and biological tissues.[40, 41]

Secondary ion mass spectrometry (SIMS) and matrix assisted laser desorption/ionisation (MALDI) are the two main ionisation techniques currently employed in mass spectrometric imaging studies. Both allow ionisation and detection of biologically significant entities in solid state biological samples.

The definition between the two techniques relates primarily to application. Where SIMS imaging can be used to determine distributions of elements and small molecules (<1000 Da) at high spatial resolution, MALDI-MS imaging provides a similar assessment of larger molecules (<100 000 Da) under lower spatial resolution (in the order of 50-200 microns).

Other more recently introduced ionisation techniques with the potential to be applied in mass spectrometric imaging include desorption electrospray ionisation (DESI) MS, direct analysis in real time (DART) MS, desorption/ionisation on silicon (DIOS) MS and matrix enhanced (ME) SIMS. DESI and DART techniques allow analysis of tissues under atmospheric pressure. Both methods are being examined in their application for mass spectrometric imaging.

Whilst DESI is primarily investigated as a diagnostic technology for medical application, it has also been investigated as a tool for imaging.[42] DART's current applications tend to lean more toward analysis of pharmaceuticals and explosives. As yet there is little evidence of its application as a mass spectrometric imaging technology. ME-SIMS is an extension of the conventional SIMS approach which utilises MALDI matrices to enhance the mass range of analysis whilst simultaneously retaining the image resolution capabilities of conventional SIMS.

Whilst there is potential for innovative ionisation methods such as DART and DIOS to be applied in the mass spectrometry imaging field, these techniques are currently only in the very early stages of development and are not yet widely regarded as imaging technologies. SIMS, MALDI and (to some extent) DESI are the main ionisation techniques applied in mass spectrometry imaging. The remainder of this chapter looks at the principles of these three techniques with particular emphasis on MALDI.

1.3.1 SIMS Imaging

SIMS is commonly used to provide nanoscale metallurgic evaluation of the optimisation and consistency of the composition of semi-conductors and other alloy metals. Whilst this remains the primary application of the technique, since the 1970's it has been investigated for application in organic analysis.[43]

SIMS imaging has made advances toward biomedical application through the analysis of the fragment ions of biologically important molecules.[44] This has largely been made possible through the advent of liquid metal ion guns (e.g. gold and bismuth cluster ion guns).[45] LMIGs have a higher focusing capacity than either of the other primary ion sources available. They have increased the lateral resolution of SIMS to the submicron level. LMIGs are also less energetic than the other primary ion beams. This makes them more useful in biological analysis. The use of LMIGs enhance the intensity of primary ion species and extend conventional SIMS mass range to in excess of 1000 Daltons.[46]

SIMS has been applied in the imaging analysis of some low mass compounds. Recently it has been shown to define the distribution of cholesterol in tissue.[47] It has also found application in determining the distribution of pharmacological compounds at the cellular level. This has been achieved by localisation of chemical elements of the drug structure (i.e. halogens).[48] SIMS analysis of isotopically labeled compounds has also been found to be effective. This method has been successful in determining the metabolism of a sodium bicarbonate in coral.[49]

SIMS uses a high energy primary ion beam to create secondary ions from a sample surface. The sample is bombarded with an ion beam creating a sputtering effect at the sample surface leading to the emission of sample components. A small proportion of the sample molecules that are ejected from the sample surface become ionised during this process (figure 1.4).

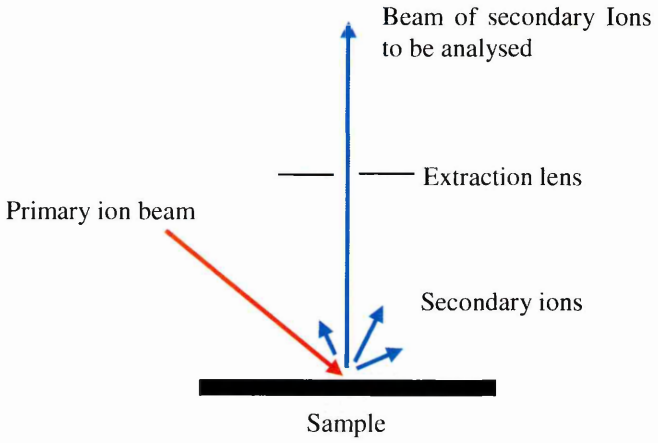

Figure 1.4 Principle of Secondary Ion Mass Spectrometry

The primary ion beam is focused at the sample surface. The high energy impact of the ion beam leads to sputtering and ejection of the surface of the sample. Some of the particles become charged during the process. These charged molecules are extracted into the mass spectrometer for analysis.

There are several classes of primary ion sources that can be used in SIMS instruments. These include duoplasmatrons which create primary ions from gaseous elements (e.g. noble gases or oxygen) or molecules (e.g. SF_5^+ or C_{60}^+); surface ionisation sources which create cesium ions by vapourisation of cesium through a porous tungsten plug; and liquid metal ion guns (LMIG) which generate primary ions from liquid state metals and alloys under the influence of an electric field.

The focusing capacity of ion beams is much greater than that of the laser beams used in MALDI. As a consequence, SIMS can map the distribution of sample components at a much greater image resolution. SIMS does however, have a limited mass range as the high energy involved in ionisation leads to extensive fragmentation. As such, this technique is applied in the study of the distribution of atoms and low mass molecules. Because of the high mass and atomic heterogeneity of many biological components, this technique often requires analytes to be naturally or synthetically labeled with a distinctive atomic entity. This technique has however been successful in allowing the analysis of both elemental and molecular distributions in cells.[50-52]

The use of matrices in SIMS imaging has also been investigated. This matrix enhanced SIMS (ME-SIMS) technique uses an organic acid to increase the conventional SIMS mass window to approximately 2500 Da.[53] This technique has been shown to provide images which maintain the high image resolution of SIMS (<1μm), whilst simultaneously allowing (to some extent) the attribute of MALDI-MS extended mass range.[54]

1.3.2 MALDI-MS Imaging

Matrix assisted laser desorption ionisation mass spectrometry (MALDI-MS) was introduced as a molecular imaging technique in the late 1990's.[40] This 'soft' ionisation technique allows analysis of intact molecules over a much broader mass spectrum than SIMS. Where SIMS imaging tends to rely on determination of fragment ions related to biological entities (such as phospholipids for example),[44, 55] in MALDI-MS these molecules are ionised intact. This can provide a more informative mode of analysis, where the heterogenous distribution of distinctive phospholipids can be defined.[56]

MALDI-MS imaging has been applied to the analysis of a number of different classes of compound. It is most widely used for protein analysis [40, 57-61], but has also been used for the analysis of pharmaceuticals[62, 63], agrochemicals[64] and other low molecular weight compounds such as endogenous metabolites [65, 66].

The principle of MALDI was adapted from the technique of laser desorption. This technique involved the dissociation of thermally labile bonds. MALDI was first introduced as a method of analysing large biomolecules by using an inorganic matrix.[67] It was further developed by Karas and Hillenkamp with the use of organic acid matrices for the analysis of involatile compounds.[38]

In MALDI-MS molecules are ionised by means of pulsed laser desorption from a solid state sample under high vacuum. The ionisation process is reliant upon a matrix (usually small organic molecules) that strongly absorbs energy at the laser wavelength. The energy absorbed by the matrix ultimately drives the matrix crystals and associated molecules into a gaseous phase matrix-analyte plume. There is much less energy imparted to the analytes than there is in the older method of laser desorption, hence it being defined as a soft ionisation technique.

The ionisation reactions that occur in MALDI are not yet fully understood. The most widely accepted mechanism for ionisation is through gas-phase proton transfer between photoionised matrix molecules and analytes in the matrix-analyte plume. The process of this reaction is illustrated in figure 1.5.

The latest advances in increasing MALDI-MS image resolution have been introduced by the combination of laser mass microprobe mass analysis and MALDI. A current limitation associated with this technique is that the lateral resolution of image acquisition exceeds that of the current means of matrix application. [68]

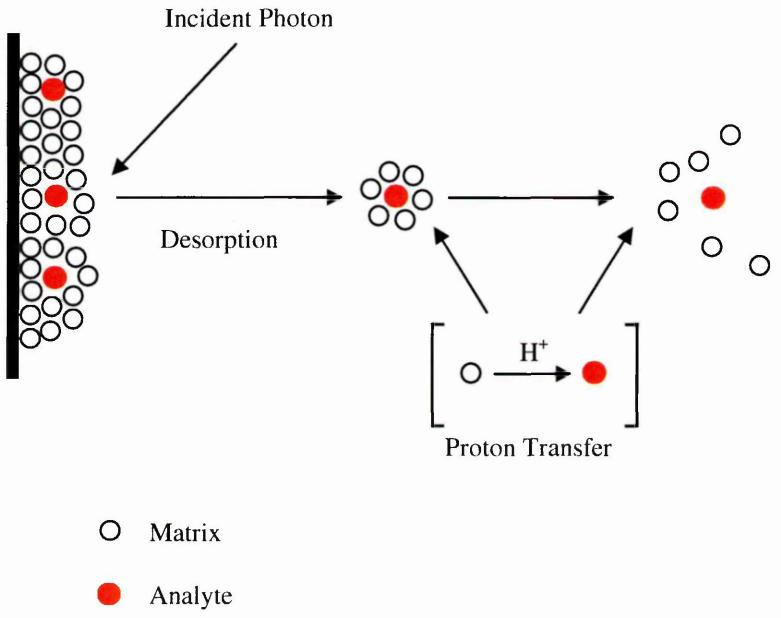

Figure 1.5 Diagram of the principle of MALDI

Laser irradiation leads to desorption of matrix and analyte into an expanding gas phase plume. Gas phase proton transfer occurs between the analyte and photoionised matrix molecules.

1.3.2 DESI Imaging

Desorption electrospray ionisation (DESI) is a relatively new technique that can be used as method of ionisation for mass spectrometric imaging. DESI uses a solvent electrospray directed at a sample surface to desorb ions for introduction into the mass spectrometer (figure 1.6). DESI is very different from SIMS and MALDI as ions are generated under ambient pressure.[69]

This technique remains in its infancy and there is currently only one report of producing images using this technique in the literature, but DESI has benefits over MADLI and SIMS as it allows for rapid analysis with no sample preparation. It has been used to analyse pharmaceutical samples such as tablets, ointments and liquids, and as such it has been shown to allow rapid automated screening of drug tablet constituents.[70]

In the imaging experiment published DESI was used for assessing the distribution of a number of fatty acids in brain tissue, image resolutions were reported to be in the region of 500 microns with unit mass resolution.[71]

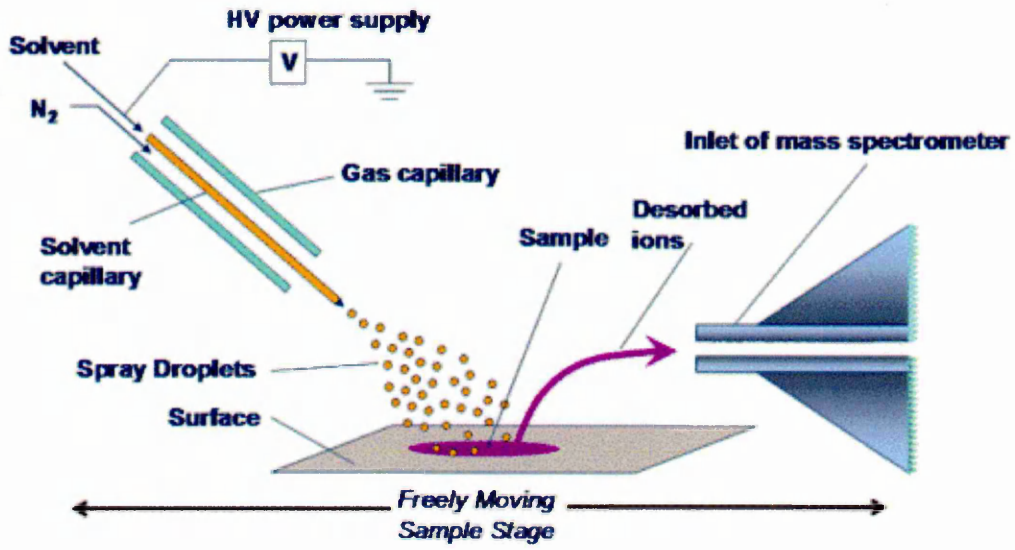

Figure 1.6 Desorption Electrospray Ionisation

A solvent under electrospray is directed at the sample surface and ions are desorbed. The ions are then introduced into the mass spectrometer for analysis.[72]

1.3.5 Mass Analysis in Mass Spectrometry Imaging

In mass spectrometry imaging ions are usually separated using a time of flight (TOF) mass analyser. TOF mass analysers have almost unlimited mass range and are amenable to pulsed modes of ionisation. This makes them ideal for analysis of large biomolecules and analysis of ions generated through the various desorption/ionisation techniques employed in imaging. The TOF mass analyser consists of a field free drift tube, through which ions travel to the detector.

Charged particles are introduced into the field free drift region as a pulse by application of an acceleration potential. At this point the kinetic energy of charged particles is equal between ions of like charge. The difference between the velocities of ions is measured by the time at which they reach the detector. The velocity of each ion is defined by the mass to charge ratio, where smaller ions will travel faster than larger ions with the same charge. The process of TOF separation is given in equation 1.

$$\frac{m}{z} = 2eEs\left(\frac{t}{d}\right)^2$$

Equation 1 The Equation of TOF Separation

The mass to charge ratio of the ion is defined by *m/z*, where *E* is the extraction pulse potential, *s* is the length of the flight tube over which the extraction pulse is applied, *d* is the length of the field free drift region and *t* is the time of flight measured for the ion.

Although TOF separation is a highly sensitive technique, there remains energy dispersion between ions of like *m/z*. This can be more prominent with ionisation sources where ions have been produced in an expanding plume. The kinetic energy spread of like ions can be resolved through introduction of a means of kinetic energy correction. One method of correcting discrepancies in kinetic energy spread is to introduce a short time delay after the ionisation event, before ions are extracted into the mass analyser. Delayed extraction allows less energetic ions to gain more kinetic energy in the source, such that ions of like *m/z* ratio become more focused at the detector plate. This is illustrated in more detail in figure 1.7.

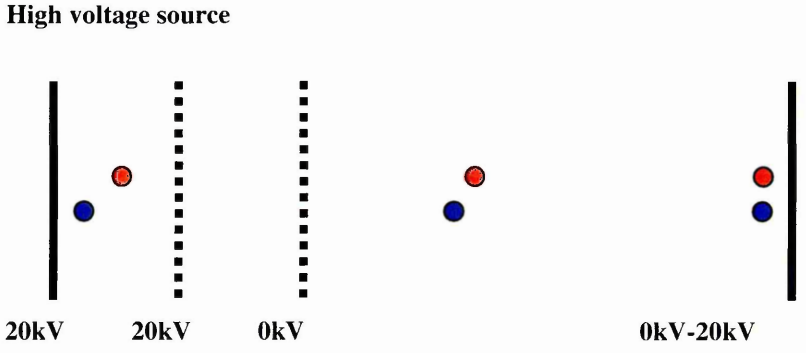

Figure 1.7 Schematic Representation of Delayed Ion Extraction

In delayed pulsed extraction mode ions of a given *m/z* with correct kinetic energy (red) spend a shorter time in the source than those of the same *m/z* with less kinetic energy (blue). The energy dispersion between the like ions is corrected as those spending longer in the source gain more kinetic energy.

Another method of increasing the mass resolution of TOF analysers is to use an electrostatic reflector (figure 1.8). A reflectron, as it is more commonly known, consists of a series of grids and ring electrodes which act as an ion mirror. In contrast to the linear TOF configuration previously described, a reflectron TOF redirects ions back through the flight region of the analyser. Kinetic energy dispersion between like ions is corrected as ions with greater kinetic energy penetrate further into the reflectron region. By retarding ions of greater kinetic energy for a greater length of time than those with less kinetic energy, discrepancies in the time of flight of ions with the same *m/z* ratio are resolved. Similar to the effect of delayed extraction, this provides increased mass resolution, as ions of like *m/z* ratio reach the detector at the same time.

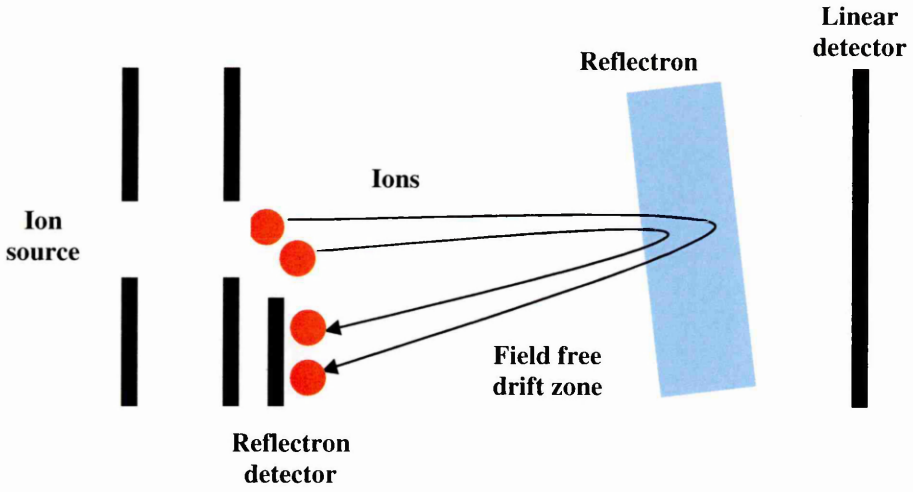

Figure 1.8 Reflectron TOF Mass Analyser

Like ions enter the mass analyser with different kinetic energy. Ions with greater kinetic energy penetrate further into the reflectron region than those of lesser kinetic energy. This allows for correction of the kinetic energy dispersion such that ions of like charge and mass reach the detector at the same time.

TOF mass spectrometers are commonly used in conjunction with quadrupole mass filters, where the quadrupole is positioned as the first mass analyser. In normal MS mode the quadrupole acts an RF only focusing device.

A quadrupole (Q) mass filter consists of four parallel metal rods with elliptical, circular or hyperbolic section. Each pair of opposing rods is given an equal fixed applied direct current voltage, with each of the two pairs of rods having contrasting polarity. An alternating radio frequency (RF) potential is superimposed onto the direct current voltage. Ions pass through the centre of the quadrupole, their trajectories defined by electric fields. By alternating the RF applied, ions of different *m/z* are brought into focus.

In a hybrid Q-TOF instrument, the quadrupole can be used to select ions of specific *m/z* ratio for a second MS analysis. The selected ions are subjected to collision induced dissociation and the resulting product ions assessed by the TOF mass analyser. Product ion scans are useful for chemical characterisation. They can also be used to enhance sensitivity as a product ion can allow differentiation between precursor ions of like or unresolved *m/z* ratio. A schematic diagram of a hybrid quadrupole mass spectrometer is shown in figure 1.9.

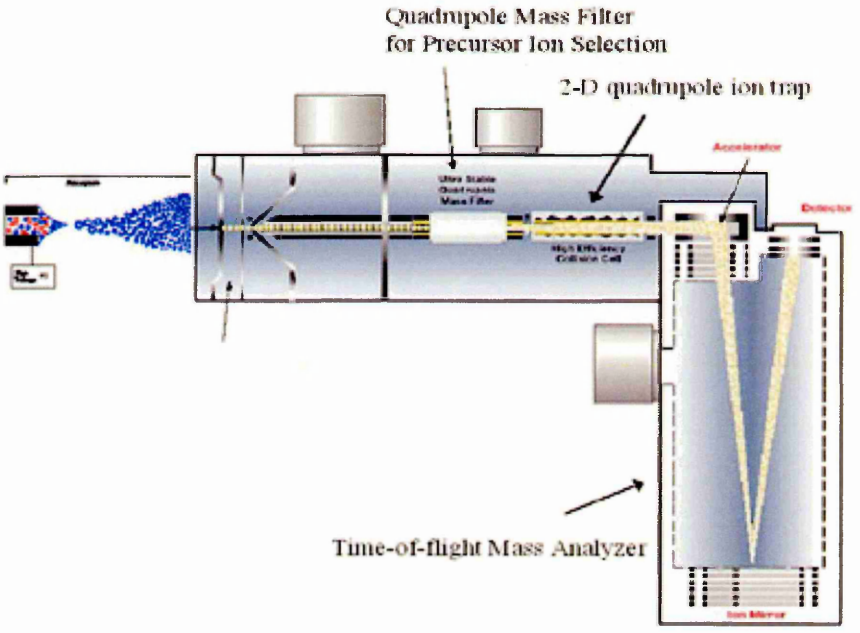

Figure 1.9 Schematic of Applied Biosystems/MDS Sciex Q-Star Pulsar *i*

A schematic diagram of an Applied Biosystems/MDS Sciex Q-Star Pulsar *i* hybrid QTOF LC/MS system with delayed pulse extraction and reflectron.[73]

1.4 Mass Spectrometry Imaging Processes

The process of mass spectrometry imaging can be divided in to various stages; sample preparation; image acquisition; and image processing. Here, the stages are explained in more detail along with methods of statistically evaluating image data.

1.4.1 Sample Preparation in Mass Spectrometry Imaging

Sample preparation is perhaps the most important step in MS image analysis. Poor sample handling can cause serious degradation in the integrity of the sample.

In SIMS imaging, the preparation of samples is dependant of the type of sample used. For tissue analysis, the sample is sectioned using a cryostat. For cell culture analysis, samples are cryogenically preserved and freeze fractured to expose intracellular contents. Samples may then be stored under high vacuum to avoid exposure to moisture that may induce analyte migration. This is particularly important with the high image resolution of SIMS, where very small amounts of moisture may lead to significant degrees of analyte migration within the sample.[74] Gold sputter coating of the sample is often carried out prior to SIMS analysis. This is found to enhance the conductivity of the sample and increase the sensitivity of analysis.[75]

MALDI-MS image samples are usually biological tissue sections. These are produced on a cryostat in the absence of embedding medium to avoid suppression of analyte signals [60]. Samples are often washed in several gradients of ethanol to remove residual salts. This serves to enhance matrix crystalisation.[59, 60]

Tissue sections are coated in an organic acid solution in preparation for MALDI analysis. Application of the matrix is an extremely important stage of the preparation procedure. The matrix has to be applied in a way that allows sufficient interaction between the analytes and matrix solvent, yet avoids any extensive wetting of the sample that might induce analyte spreading. This can be achieved in a number of different ways. Electrospray deposition[76], air-spray deposition or nebulisation[58, 60, 77] and nano-scale matrix spotters have been used.[78] The choice of matrix solvent can be pivotal to the sensitivity of the analysis. The solvent must take into account the solubility of analytes as well as the matrix.[79] As with SIMS imaging, samples are sometimes sputter-coated in gold to enhance sensitivity and reduce the surface charging effect that can lead to distortion of ion images.[80]

Advances in sample preparation will be critical in allowing higher resolution MALDI-MS image analysis. Optimisation of matrix solvents and the use of nanoscale matrix deposition devices has already been demonstrated to increase the sensitivity of analyte detection and reduce the degree of analyte spreading respectively.[60, 78, 81]

ME-SIMS is a new adaptation of the conventional SIMS approach that includes the use of organic matrices in a similar manner to MALDI experiments. This method of analysis yields comparable results to those found with MALDI-MS imaging up to masses of approximately 2500 Da. The advantage of applying SIMS to a sample prepared with a MALDI matrix is that images can be acquired with a much higher spatial resolution (between 60 and 500 nm) than can be obtained in conventional MALDI-MS imaging.

1.4.2 Mass Spectrometry Image Acquisition

The analytical apparatus required to produce mass spectrometric images is similar to that used in the relevant conventional mass spectrometric technique. The instrumentation and software is adapted slightly to allow the sample plate to be moved at set increments beneath the ion or photon beam. As the ion or photon beam is rastered across the sample surface, a mass spectral analysis is performed at a series of pre-determined points. The mass spectrum acquired at each point is recorded along with the relative *x,y* co-ordinate and these data are then used to build an ion image. Figure 1.10 illustrates the process of mass spectrometry image acquisition.

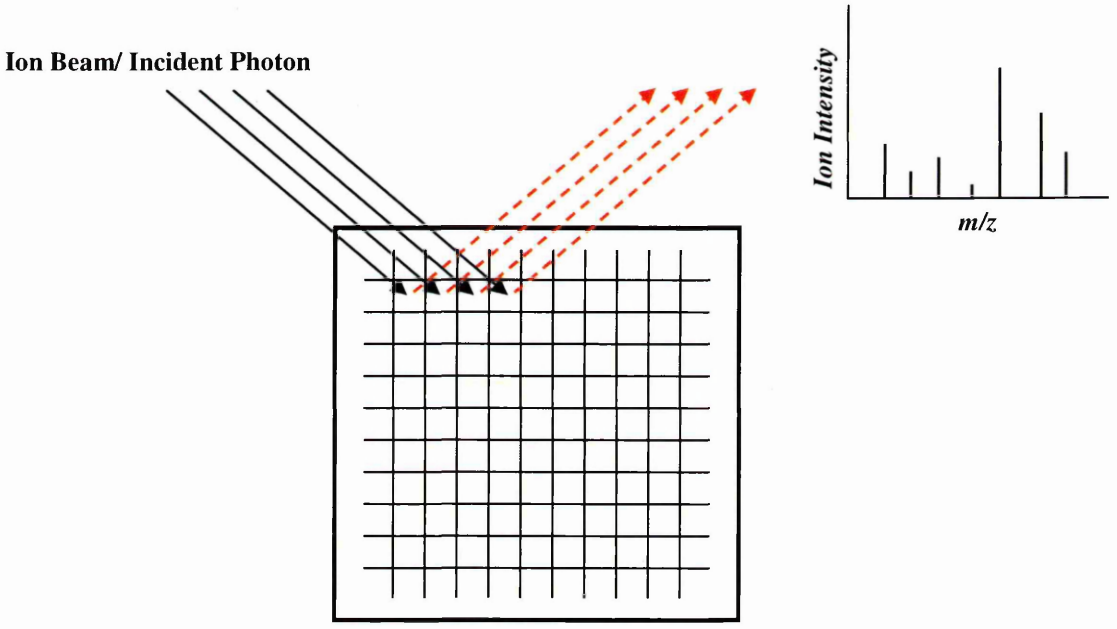

Figure 1.10 Mass Spectrometry Image Acquisition

The sample plate is moved at set increments beneath the stationary ion or photon beam. A mass spectrum is acquired at each point and recoded with its *x,y* co-ordinate.

In this mode of analysis, known as mass microprobe mode, the confines of image resolution are defined by the laser spot diameter, although over-sampling can be carried out.

Recently a new method of acquiring MALDI-MS images has been described, known as the mass microscope.[82] Position-correlated ion detection is used to generate an ion image of approximately 4μm resolution from a single stationary laser ablation spot on the sample surface. By scanning across the sample surface, a number of ion images can be produced (figure 1.11). These can be pieced together to form a high resolution ion image of the sample.

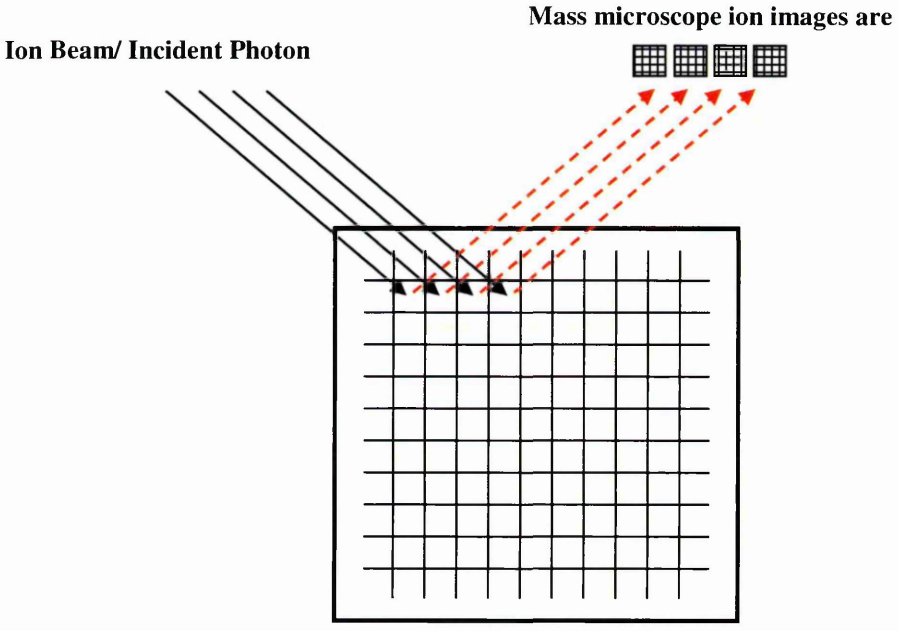

Figure 1.11 Acquiring ion images in mass microscope scanning mode

As the laser passes across the sample surface a mass microsope image is acquired at each point. The ion images are concatenated to produce a high resolution ion image of the sample surface.

1.4.3 Image Processing

The data acquired during MS image analysis are sorted computationally by *m/z* ratio, ion intensity and *x,y* co-ordinate. Imaging software is used to digitally scan through the data to obtain the ion intensities recorded for a defined *m/z* range or *m/z* value. The intensities found for the mass range or value selected are displayed in a two dimensional plot, where ion intensity is shown on a linear scale by a change in brightness or hue for each *x,y* co-ordinate or pixel. The pixel size is determined at the time of analysis, where the plate stepping measurements are defined by the user. Limitation of the level of image resolution is largely defined by the laser or ion beam diameter.

1.4.4 Statistical Evaluation of Mass Spectrometry Image Data

The data acquired in mass spectrometry imaging can be difficult to interpret, and hence a number of statistical approaches have been employed to compress, de-noise and determine patterns in the hyperspectral data. Statistical techniques conventionally applied to enhance the quality of many types of digital image data have been assessed for their application in mass spectrometry imaging. Principal components analysis (PCA), discriminant analysis (DA) and factor analysis (FA) have been used to extract localised variation in ion abundance using the ion intensities recorded in the image mass spectra.[83, 84] Other statistical methods have also been applied to PCA treated data which function to maximize the variance attributed to each of the principal components.[85]

Images are produced using the principal component scores for each individual pixel. As such, the quality of the final image is considerably enhanced and it is possible to classify tissue types by spectral pattern as opposed to a single ion.[83]

1.5 MALDI-MS Imaging Research

MALDI mass spectrometry imaging holds great potential for application in biomedical research. The capacity to simultaneously profile and map the distribution of molecules in situ has led to widespread interest in the technique by academia and industry alike. The unparalleled ability that MALDI-MS holds for detecting a large number of molecules simultaneously from a tissue surface makes it an attractive alternative to many of the conventional molecular imaging methodologies that are currently employed in research.

The initial experiments in MALDI-MS imaging were carried out by the Caprioli group in the late 1990's. Here, the technique was first promoted for its ability to detect protein and peptide signals directly from tissues sections. It was observed that tissue types could be distinguished by the unique signal profiles observed. It was also found that there was a high level of homology in the profiles taken from tissues of genetically similar mouse strains.[86] The direct analysis of tissues by MALDI-MS has since been applied to much greater extent, with successful detection of peptide and protein signals from a broad range of different tissue types.[40, 87-89]

The technique has more recently been extended to the analysis of other molecules such as small metabolites[65, 66] and pharmaceutical compounds.[62, 90, 91] With particular emphasis being placed on the application of MALDI-MS imaging in the study of the pathogenesis and treatment of disease, analysis of smaller molecules is an extremely important development for extending MALDI-MS imaging analysis into the clinical field. Promotion of MALDI-MS image analysis as a method of pre-clinical assessment has been influenced by the successful analysis of whole body sections like those used in whole body autoradiography.[92-95] With these images it is not only possible to pinpoint the distribution of drugs inside the body of the dosed animal, but it is also possible to differentiate between the drug and its metabolites in situ, a major limitation associated with whole body autoradiographic analysis.

With the fundamental aspects of MALDI-MS imaging in place for the analysis of a wide variety of molecules and tissues, research has now become directed toward how best to optimise the imaging approach. This is being done in several areas, primarily in sample preparation, but more recently it has emerged that data normalisation is an important aspect as well.[96]

The need to optimise and regulate the image sample preparation process has been a source of extensive research. Several publications stress the importance of sample preparation on the quality of image results. These relate to sample handling, various sample treatments[60] and perhaps most prominently to matrix application. For the latter, the outcome has been the development of several automated matrix deposition devices.[78, 81]

Currently many of the MALDI-MS imaging reports have been directed toward the analysis of specific molecular targets. In order to utilise all of the information obtained during MALDI-MS image analysis, several research groups have begun to look deeper into methods of data interpretation. A number of methods have been proposed as ways of statistically sorting through the vast amounts of data. These include principal components analysis and multivariate cluster analysis.[83]

Some of these areas of MALDI-MS imaging research that are directed toward optimizing the method are investigated in this thesis. More in depth discussions of the current research associated with each area is presented as the introduction to each experimental chapter.

1.6 Aims of Work

The work carried out in this thesis is based on the imaging of small molecules by MALDI-MS. Experiments are focused toward assessing the fundamental aspects of MALDI-MS imaging in this area of applications. The application of a high repetition laser is evaluated for use in MALDI-MS imaging experiments. The various methods of data normalisation conventionally used in MALDI-MS imaging are compared and a new method is investigated. Optimisations of sample preparation procedures for both direct and indirect imaging of biological tissues are assessed and the use of principal components analysis is evaluated for application as a latent variable determinant from the hyperspectral datasets.

1.7 References

1. VALLEJO-MANZUR, F., PERKINS, Y., VARON, J. and BASKETT, P., 2003/1. Andreas Vesalius, the concept of an artificial airway. *Resuscitation,* **56**(1), pp. 3-7.

2. RUSKA, H., VON BERRIES, B. and RUSKA, E., 1940. Die bedeutung der übermikroskopie für die virusforschung. *Arch ges Virusforsch,* **1**, pp. 155-169.

3. CHAO, S., DOUGHERTY, W.M. and GARBINI, J.L., 2004. Nanometer-scale magnetic resonance imaging. *Review of Scientific Instruments,* **75**(5), pp. 1175-1181.

4. TSUJI, S., MASUMIZU, T. and YOSHINARI, Y., 2004. Magnetic resonance imaging of isolated single liposome by magnetic resonance force microscopy. *Journal of Magnetic Resonance,* **167**(2), pp. 211-220.

5. STIPE, B.C., MAMIN, H.J., YANNONI, C.S., STOWE, T.D., KENNY, T.W. and RUGAR, D., 2004. Electron spin relaxation near a micron-size ferromagnet. *Physical Review Letters,* **87**, pp. 277602-277614.

6. BAUMJOHANN, D., HESS, A., BUDINSKY, L., BRUNE, K., SCHULER, G. and LUTZ, M.B., 2006. *In vivo* magnetic resonance imaging of dendritic cell migration into the draining lymph nodes of mice. *European journal of immunology,* **36**(9), pp. 2544-2555.

7. MCCONNELL, G., 2006. Improving the penetration depth in multiphoton excitation laser scanning microscopy. *Journal of Biomedical Optics,* **11**(5), pp. 54020-54026.

8. HOMANN, U., MECKEL, T., HEWING, J., HÜTT, M. and HURST, A., 2007. Distinct fluorescent pattern of KAT1::GFP in the plasma membrane of Vicia faba guard cells. *European Journal of Cell Biology,* **86**(8), pp. 489-500.

9. Bene, L. *et al.* Colorectal carcinoma rearranges cell surface protein topology and density in CD4+ T cells, 2007. *Biochemical and Biophysical Research Communications* **361**, 202-207.

10. EVANS, J.A. and NISHIOKA, N.S., 2005. Endoscopic confocal microscopy. *Current Opinions in Gasteroenterology,* **21**(5), pp. 578-584.

11. JANSHOFF, A., Confocal laser scanning microscopy. Last updated 2006. Available: http://www.uni-mainz.de/FB/Chemie/AK-Janshoff/137_DEU_HTML.php. Last accessed September 9th 2007.

12. DENK, W., STRICKLER, J.H. and WEBB,W., 1990. Two-photon laser scanning fluorescence microscopy. *Science,* **248**, pp. 73-76.

13. SVOBODA, K., KLEINFELD, D. and TANK, D.W., 1997. In vivo dendritic calcium dynamics in neuronal pyramidal neurons. *Nature,* **385**, pp. 161-165.

14. KLEINFELD, D., MITRA, P.P., HELMCHEN, F. and DENK, W., 1998. Fluctuations and stimulus-induced changes in blood flow observed in individual capillaries in layers 2 through 4 of rat neocrotex. *Proceedings of the National Academy of Sciences of the United States of America,* **95**, pp. 15741-15746.

15. SVOBODA, K., HELMCHEN, F., DENK, W. and TANK, D.W., 1999. Spread of dendritic excitation in layer 2/3 pyramidal neurons in rat barrel cortex. *Nature Neuroscience,* **2**, pp. 65-73.

16. KIRCHHOFF, N.A., KERR, F. and HELMCHEN, F., 2004. Sulforhodamine 101 as a specific marker of astroglia in the neocortex in vivo. *Nature Methods,* **1**, pp. 31-37.

17. MIZRAHI, A., CROWLEY, J., SHTOYERMAN, E. and KATZ, L., 2004. High-resolution in vivo imaging of hippocampal dendrites and spines. *Journal of Neuroscience,* **24**, pp. 3147-3151.

18. MOLITORIS, B.A. and SANDOVAL, R.M., 2005. Intravital multiphoton microscopy of dynamic renal processes. *American Journal of Physiology Renal Physiology,* **288**, pp. 1084-1089.

19. BOUSSO, P. and ROBEY, E.A., 2004. Dynamic behaviour of T cells and thymocytes in lymphoid organs as revealed by two-photon microscopy. *Immunity,* **21**, pp. 349-355.

20. HUA, W., SHEFF, D., TOONUE, D. and MELLMAN, I., 2006. Vectorial insertion of apical and basolateral membrane proteins in polarized epithelial cells revealed by quantitative 3D live cell imaging. *Journal of Cell Biology,* **172**(7), pp. 1035-1044.

21. SHAH, K., TANG, Y., BREAKEFIELD, X.O. and WEISSLEDER, R., 2003. Real-time imaging of TRAIL-induced apoptosis of glioma tumors in vivo. *Oncogene,* **22**, pp. 6865-6872.

22. CONTAG, C., CONTAG, P., MULLINS, J., SPILMAN, S., STEVENSON, D. and BENARON, D., 1995. Photonic detection of bacterial pathogens in living hosts. *Molecular Microbiology,* **18**(593), pp. 603.

23. ROCHETTA, H.L., BOYLAN, C.J., FOLEY, J.W., IVERSEN, P.W., LETOURNEAU, D.L. and MCMILLIAN, C.L., 2001. Validation of a noninvasive, real-time imaging technology using bioluminescent Escherichia coli in the neutropenic mouse thigh model of infection. *Antomicrobial Agents and Chemotherapy,* **48**, pp. 129-137.

24. DOYLE, T.C., NAWOTKA, K.A., KAWAHARA, C.B., FRANCIS, K.P. and CONTAG, P.R., 2006. Visualizing fungal infections in living mice using bioluminescent pathogenic *Candida albicans* strains transformed with the firefly luciferase gene. *Microbial Pathogenesis,* **40**, pp. 82-90.

25. SHAH, K., JACOBS, A., BREAKEFIELD, X.O. and WEISSLEDER, R., 2004. Molecular imaging of gene therapy for cancer, Gene Therapy, *Gene Therapy,* **11**(1175), pp. 1187.

26. WEISSLEDER, R. and NTZIACHRISTOS, V., 2003. Shedding light onto live molecular targets. *Nature,* **9**, pp. 123-128.

27. CHO, M.J., LYOO, I.K., LEE, D.W., KWON, J.S., LEE, J.S., LEE, D.S., JUNG, J.K. and LEE, M.C., 2002. Brain single photon emission computed tomography findings in depressive pseudodementia patients. *Journal of Affective Disorders,* **69**(1-3), pp. 159-166.

28. MAO, Y.L., ZHANG, T., SANG, X.T., LI, F., BA, J.T., LU, X., YANG, Z.Y., ZHONG, S.X. and HUANG, J.F., 2007. Three-dimensional assessment of the remnant hepatic function following surgery using single photon emission computed tomography in an animal model. *Zhonghua Wai Ke Za Zhi,* **45**(9), pp. 609-612.

29. HWANG, L.C., CHANG, C.J., LIU, H.H., KAO, H.C., LEE, S.Y., JAN, M.L. and CHEN, C.C., 2007. Imaging the availability of serotonin transporter in rat brain with 123I-ADAM and small-animal SPECT. *Nuclear Medicine Communications,* **28**(8), pp. 615-621.

30. YANG, D.Y., OUYANG, C.H., LU, F.G., LIU, X.W. and HUANG, L.Q., 2007. Targeting specificity and pharmacokinetics of asialoorosomucoid, a specific ligand for asialglycoprotein receptor on hepatocyte. *Journal of Digestive Diseases,* **8**(2), pp. 89-95.

31. CHIN, K., FINGER, P., KURLI, M., TENA, L. and REDDY, S., 2007. Second cancers discovered by 18FDG PET/CT imaging for choroidal melanoma. *Optometry - Journal of the American Optometric Association,* **78**(8), pp. 396-401.

32. MOISSET, X. and BOUHASSIRA, D., 2007. Brain imaging of neuropathic pain. *NeuroImage,* **37**(Supplement 1), pp. S80-S88.

33. MCQUEEN, F. and ØSTERGAARD, M., 2007. Established rheumatoid arthritis – new imaging modalities. *Best Practice & Research Clinical Rheumatology,* **21**(5), pp. 841-856.

34. READER, A. and ZWEIT, J., 2001. Developments in whole-body molecular imaging of live subjects. *Trends in Pharmacological Sciences,* **22**(12), pp. 604-607.

35. DELGUERRA, A. and BELCARI, N., 2007. State-of-the-art of PET scanners for small animal and breast cancer imaging. *Nuclear Instruments and Methods in Physics Research Section A: Accelerators, Spectrometers, Detectors and Associated Equipment,* **580**(2), pp. 910-914.

36. JIANG, L.J., TAKEUCHI, R., LEWSLEY, A., SONDERFAN, A., BABA, T. and OR, Y.S., 2007. Tissue distribution of [14C]-EDP-420 in the rat by quantitative whole-body autoradiography. *International Journal of Antimicrobial Agents,* **29**, pp. S605.

37. POSTHUMUS, M.A., KISTEMAKER, P.G., MEUZELAAR, L.C. and TEN, M.C., 1978. Laser desorption-mass spectrometry of polar non-volatile bio-organic molecules. *Analytical Chemistry,* **50**(7), pp. 985-991.

38. KARAS, M. and HILLENKAMP, F., 1988. Laser desorption ionisation of proteins with molecular masses exceeding 10,000 daltons. *American Chemistry,* **60**, pp. 2299-2301..

39. PACHUTA, S.J. and COOKS, R.G., 1987. Mechanisms in molecular SIMS. *Chemistry Reviews,* **87**(3), pp. 647-669.

40. CAPRIOLI, R.M., FARMER, T.B. and GILE, J., 1997. Molecular imaging of biological samples: localisation of peptides and proteins using MALDI-TOF MS. *Analytical Biochemistry,* **69**, pp. 4751-4760

41. PACHOLSKI, M.L. and WINOGRAD, N., 1999. Imaging with mass spectrometry. *Chemical reviews,* **99**(10), pp. 2977-3006.

42. WISEMAN, J.M., IFA, D.R., SONG, Q. and COOKS, R.G., 2006. Tissue imaging at atmospheric pressure using desorption electrospray ionization (DESI) mass spectrometry. *Angewandte Chemie,* **118**(43), pp. 7346-7350.

43. GALLE, P., 1970. Sur une nouvelle méthode d'analyse cellulaire utilisant le phénomène d'émission ionique secondaire. *Ann. Phys. Biol,* **42**, pp. 83-94.

44. NYGREN, H., BÖRNER, K., HAGENHOFF, B., MALMBERG, P. and MÅNSSON, J., 2005. Localization of cholesterol, phosphocholine and galactosylceramide in rat cerebellar cortex with imaging TOF-SIMS equipped with a bismuth cluster ion source. *Biochimica et Biophysica Acta (BBA) - Molecular and Cell Biology of Lipids,* **1737**(2-3), pp. 102-110.

45. TOUBOUL, D., HALGAND, F., BRUNELLE, A., KERSTING, R., TALLAREK, E., HAGENHOFF, B. and LAPREVOTE, O., 2004. Tissue molecular ion imaging by gold cluster ion bombardment. *Analytical Chemistry,* **76**, pp. 1551-1559.

46. TOUBOUL, D., KOLLMER, F., NIEHUIS, E., BRUNELLE, A. and LAPRÉVOTE, O., 2005. Improvement of biological time-of-flight secondary ion mass spectrometry imaging with a bismuth cluster ion source. *Journal of the American Society for Mass Spectrometry,* **16**(10), pp. 1608-1618.

47. NYGREN, H., JOHANSSON, B.R. and MALMBERG, P., 2004. Bioimaging TOF-SIMS of tissues by gold ion bombardment of a silver-coated thin tissue section. *Microscopy Research and Technique,* **65**(6), pp. 282-286.

48. FRAGU, P. and KAHN, E., 1997. Secondary ion mass spectrometry (SIMS) microscopy: A new tool for pharmacological studies in humans. *Microscopy Research and Technique,* **36**(4), pp. 296-300.

49. CLODE, P.L., STERN, R.A. and MARSHALL, A.T., 2007. Subcellular imaging of isotopically labelled carbon compounds in a biological sample by ion microprobe (NanoSIMS). *Microscopy Research and Technique,* **70**(3), pp. 220-229.

50. FARTMANN, M., DAMBACH, S., KRIEGESKOTTE, C., WIESMANN, H.P., WITTIG, A., SAUERWEIN, W., LIPINSKY, D. and ARLINGHAUS, H.F., 2002. Characterization of cell cultures with ToF-SIMS and laser-SNMS. *Surface and Interface Analysis,* **34**, pp. 63-66.

51. COLLIVER, T.L., BRUMMEL, C.L., PACHOLSKI, M.L., SWANEK, F.D., EWING, A.G. and WINOGRAD, N., 1997. Atomic and molecular imaging at the single-cell level with TOF-SIMS. *Analytical Chemistry,* **69**(13), pp. 2225-2231.

52. MAS, S., TOUBOUL, D., BRUNELLE, A., ARAGONCILLO, P., EGIDO, J., LAPREVOTE, O. and VIVANCO, F., 2007. Lipid cartography of atherosclerotic plaque by cluster-TOF-SIMS imaging. *Analyst,* **132**, pp. 24-26.

53. ALTELAAR, A.F.M., VANMINNEN, J., JIMENEZ, C.R., HEEREN, R.M.A. and PIERSMA, S.R., 2005. Direct Molecular Imaging of Lymnaea stagnalis Nervous Tissue at Subcellular Spatial Resolution by Mass Spectrometry. *Analytical Chemistry,* **77**(3), pp. 735-741.

54. MCDONNELL, L.A., PIERSMA, S.R., ALTELAAR, A.F.M., MIZE, T.H., LUXEMBOURG, S.L., VERHAERT, P.D.E.M., VAN MINNEN, J. and HEEREN, R.M.A., 2005. Subcellular imaging mass spectrometry of brain tissue. *Journal of Mass Spectrometry,* **40**(2), pp. 160-168.

55. MALMBERG, P., BÖRNER, K., CHEN, Y., FRIBERG, P., HAGENHOFF, B., MÅNSSON, J. and NYGREN, H., 2007. Localization of lipids in the aortic wall with imaging TOF-SIMS. *Biochimica et Biophysica Acta - Molecular and Cell Biology of Lipids,* **1771**(2), pp. 185-195.

56. SHIMMA, S., SUGIURA, Y., HAYASAKA, T., HOSHIKAWA, Y., NODA, T. and SETOU, M., 2007. MALDI-based imaging mass spectrometry revealed abnormal distribution of phospholipids in colon cancer liver metastasis. *Journal of Chromatography B,* **855**(1), pp. 98-103.

57. STOECKLI, M., CHAURAND, P. and CAPRIOLI, R.M., 2001. Direct profiling of proteins in biological tissue sections by MALDI mass spectrometry. *Nature Medicine,* **7**, pp. 493-496.

58. CHAURAND, P., SCHWARTZ, S.A. and CAPRIOLI, R.M., 2002. Imaging mass spectrometry: A new tool to investigate the spatial organisation of peptides and proteins in mammalian tissue sections. *Current Opinion in Chemical Biology,* **6**, pp. 676-681.

59. CHAURAND, P., FOUCHECOURT, S., DAGUE, B.B., XU, B.J., REYZER, M.L., ORGEBIN-CRIST, M.C. and CAPRIOLI, R.M., 2003. Profiling and imaging proteins in the mouse epididymis by imaging mass spectrometry. *Proteomics,* **3**, pp. 2221-2239.

60. SCHWARTZ, S.A., REYZER, M.L. and CAPRIOLI, R.M., 2003. Direct tissue analysis using matrix-assisted laser desorption/ionisation mass spectrometry: Practical aspects of sample preparation. *Journal of Mass Spectrometry,* **38**, pp. 699-708.

61. REYZER, M.L. and CAPRIOLI, R.M., 2007. MALDI-MS-based imaging of small molecules and proteins in tissues. *Current Opinion in Chemical Biology,* **11**(1), pp. 29-35.

62. REYZER, M.L., HSIEH, Y., NG, K., KORFMACHER, W.A. and CAPRIOLI, R.M., 2003. Direct Analysis of Drug Candidates in Tissue by Matrix-Assisted Laser Desorption/Ionisation Mass Spetrometry. *Journal of Mass Spectrometry,* **38**, pp. 1081-1092.

63. BUNCH, J., CLENCH, M.R. and RICHARDS, D.S., 2004. Determination of pharmaceutical compounds in skin by imaging matrix assisted laser desorption/ionisation mass spectrometry. *Rapid Communications in Mass Spectrometry,* **18**, pp. 3051-3060.

64. MULLEN, A.K., CLENCH, M.R., CROSLAND, S. and SHARPLES, K.R., 2005. Determination of agrochemical compounds in soya plants by imaging matrix-assisted laser desorption/ionisation mass spectrometry. *Rapid Communications in Mass Spectrometry,* **19**(18), pp. 2507-2516.

65. ROBINSON, S., WARBURTON, K., SEYMOUR, M., CLENCH, M.R. and THOMAS-OATES, J., 2007. Localization of water-soluble carbohydrates in wheat stems using imaging matrix-assisted laser desorption ionization mass spectrometry. *Rapid Communications in Mass Spectrometry,* **21**(7), pp. 1271-1276.

66. BURRELL, M.M., EARNSHAW, C.J. and CLENCH, M.R., 2007. Imaging matrix assisted laser desorption ionization mass spectrometry: a technique to map plant metabolites within tissues at high spatial resolution. *Journal of Experimental Botany,* **58**, pp. 757-763.

67. TANAKA, K., WAKI, H., IDO, Y., AKITA, S., YOSHIDA, Y. and YOSHIDA, T., 1988. Protein and polymer analyses up to *m/z* 100,000 by laser ionization time-of-flight mass spectrometry. *Rapid Communications in Mass Spectrometry,* **2**, pp. 151-153.

68. BOUSCHEN, W. and SPENGLER, B., 2007. Artifacts of MALDI sample preparation investigated by high-resolution scanning microprobe matrix-assisted laser desorption/ionization (SMALDI) imaging mass spectrometry. *International Journal of Mass Spectrometry,* **266**(1-3), pp. 129-137.

69. TAKATS, Z., WISEMAN, J.M., GOLOGAN, B. and COOKS, R.G., 2004. Mass Spectrometry Sampling Under Ambient Conditions with Desorption Electrospray Ionization. *Science,* **306**, pp. 471.

70. CHEN, H., TALATY, N.N., TAKATS, Z. and COOKS, R.G., 2005. Desorption Electrospray Ionization Mass Spectrometry for High-Throughput Analysis of Pharmaceutical Samples in the Ambient Environment. *Analytical Chemistry,* **77**(21), pp. 6915-6927.

71. WISEMAN, J.M., IFA, D.R., SONG, Q. and COOKS, R.G., 2006. Tissue imaging at atmospheric pressure using desorption electrospray ionization (DESI) mass spectrometry. *Angewandte Chemie,* **118**(43), pp. 7346-7350.

72. Desorption electrospray ionisation (DESI), Last updated 2006. Available: http://www.prosolia.com/DESI.html. Last accessed September 9th 2007.

73. Instrument pictures and schematics. Last Updated 2006. Available: http://www.chem.purdue.edu/mcluckey/instrumentation.htm. Last accessed August 10th 2007.

74. BÖRNER, K., MALMBERG, P., MÅNSSON, J. and NYGREN, H., 2007. Molecular imaging of lipids in cells and tissues. *International Journal of Mass Spectrometry,* **260**(2-3), pp. 128-136.

75. LEVI-SETTI, R., GAVRILOV, K.L. and NEILLY, M.E., 2006. Cations in mammalian cells and chromosomes: Sample preparation protocols affect elemental abundances by SIMS. *Applied Surface Science,* **252**(19), pp. 6765-6769.

76. KRUSE, R. and SWEEDLER, J.V., 2003. Spatial profiling invertebrate ganglia using MALDI MS. *American Society for mass spectrometry,* **14**, pp. 752-759.

77. CHAURAND, P. and CAPRIOLI, R.M., 2002. Direct profiling and imaging of peptides and proteins from mammalian cells and tissue sections by mass spectrometry. *Electrophoresis,* **23**, pp. 3125-3135.

78. HANS-RUDOLF AERNI, R.M., CORNETT, D.S. and CAPRIOLI, R.M., 2006. Automated acoustic matrix deposition for MALDI sample preparation. *Analytical Chemistry,* **78**(3), pp. 827-834.

79. COHEN, L.H. and GUSEY, A.I., 2002. Small molecule analysis by MALDI mass spectrometry. *Analytical and Bioanalytical Chemistry,* **373**, pp. 571-586.

80. ALTELAAR, A.F.M., TABAN, I.M., MCDONNELL, L.A., VERHAERT, P.D.E.M., DE LANGE, R.P.J., ADAN, R.A.H., MOOI, W.J., HEEREN, R.M.A. and PIERSMA, S.R., 2007. High-resolution MALDI imaging mass spectrometry allows localization of peptide distributions at cellular length scales in pituitary tissue sections. *International Journal of Mass Spectrometry,* **260**(2-3), pp. 203-211.

81. SHIMMA, S., FURUTA, M., ICHIMURA, K., YOSHIDA, Y. and SETOU, M., 2006. Direct MS/MS analysis in mammalian tissue sections using MALDI-QIT-TOFMS and chemical inkjet technology. *Surface and Interface Analysis,* **38**(12-13), pp. 1712-1714.

82. LUXEMBURG, S.L., MIZE, T.H., MCDONNELL, L.A. and HEEREN, R.M.A., 2004. High-Spatial Resolution Mass Spectrometric Imaging of Peptide and Protein Distributions on a Surface. *Analytical Chemistry,* **76**, pp. 5339-5344.

83. MCCOMBIE, G., STAAB, D., STOECKLI, M. and KNOCHENMUSS, R., 2005. Spatial and spectral correlations in MALDI mass spectrometry images by clustering and multivariate analysis. *Analytical Chemistry,* **19**, pp. 6118-6124.

84. MILILLO, T.M., GARDELLA, J., and JOSEPH A., 2006. Spatial statistics and interpolation methods for TOF SIMS imaging. *Applied Surface Science,* **252**(19), pp. 6883-6890.

85. KLERK, L.A., BROERSEN, A., FLETCHER, I.W., VAN LIERE, R. and HEEREN, R.M.A., 2007. Extended data analysis strategies for high resolution imaging MS: New methods to deal with extremely large image hyperspectral datasets. *International Journal of Mass Spectrometry,* **260**(2-3), pp. 222-236.

86. CHAURAND, P., STOECKLI, M. and CAPRIOLI, R.M., 1999. Direct profiling of proteins in biological tissue sections by MALDI mass spectrometry. *Analytical Chemistry,* **71**, pp. 5263-5270.

87. ZHENG, Y., XU, Y., YE, B., LEI, J., WEINSTEIN, M.H., O'LEARY, M.P., RICHIE, J.P., MOK, S.C. and LIU, B.C., 2003. Prostate carcinoma tissue proteomics for biomarker discovery. *Cancer,* **98**(12), pp. 2576-2582.

88. TODD, P.J., SCHAAFF, T.G., CHAURAND, P. and CAPRIOLI, R.M., 2001. Organic ion imaging of biological tissue with secondary ion mass spectrometry and matrix-assisted laser desorption/ionization. *Journal of Mass Spectrometry,* **36**(4), pp. 355-369.

89. STOECKLI, M., CHAURAND, P., HALLAHAN, D.E. and CAPRIOLI, R.M., 2001. Imaging mass spectrometry: A new technology for the analysis of protein expression in mammalian tissues. *Nature Medicine,* **7**, pp. 493-496.

90. TROENDLE, F., REDDICK, C. and YOST, R., 1999. Detection of pharmaceutical compounds in tissue by matrix-assisted laser desorption/ionization and laser desorption/chemical ionization tandem mass spectrometry with a quadrupole ion trap. *Journal of the American Society for Mass Spectrometry,* **10**(12), pp. 1315-1321.

91. HSIEH, Y., CASALE, R., FUKUDA, E., CHEN, J., KNEMEYER, I., WINGATE, J., MORRISON, R. and KORFMACHER, W., 2006. Matrix-assisted laser desorption/ionization imaging mass spectrometry for direct measurement of clozapine in rat brain tissue. *Rapid Communications in Mass Spectrometry,* **20**(6), pp. 965-972

92. KHATIB-SHAHIDI, S., ANDERSSON, M., HERMAN, J.L., GILLESPIE, T.A. and CAPRIOLI, R.M., 2006. Direct molecular analysis of whole-body animal tissue sections by imaging MALDI mass spectrometry. *Analytical Chemistry,* **78**(18), pp. 6448-6456.

93. HSIEH, Y., CHEN, J. and KORFMACHER, W., 2007. Mapping pharmaceuticals in tissues using MALDI imaging mass spectrometry. *Journal of Pharmacological and Toxicological Methods,* **55**(2), pp. 193-200.

94. REYZER, M.L. and CAPRIOLI, R.M., 2007. MALDI-MS-based imaging of small molecules and proteins in tissues. *Current Opinion in Chemical Biology,* **11**(1), pp. 29-35.

95. STOECKLI, M., STAAB, D. and SCHWEITZER, A., 2007. Compound and metabolite distribution measured by MALDI mass spectrometric imaging in whole-body tissue sections. *International Journal of Mass Spectrometry,* **260**(2-3), pp. 195-202.

96. NORRIS, J.L., CORNETT, D.S., MOBLEY, J.A., ANDERSSON, M., SEELEY, E.H., CHAURAND, P. and CAPRIOLI, R.M., Processing MALDI mass spectra to improve mass spectral direct tissue analysis. *International Journal of Mass Spectrometry,* **260**(2), pp. 212-221.

CHAPTER 2

Evaluation of a High Repetition Rate Nd:YAG Laser

2 Evaluation of a High Repetition Nd:YAG Laser

2.1 Introduction

The fundamental principle of the MALDI process is based on the irradiation of matrix crystals and associated analytes through application of a laser beam. A laser is a mechanical device that is used to produce coherent radiation.

The term 'laser' is an acronym for **L**ight **A**mplification by **S**timulated **E**mission of **R**adiation. A laser works via excitation of gain medium atoms and their release of photons at specific wavelengths as they return to their ground state.

The wavelength of the laser is governed by the gain medium used in the laser system. The gain medium may be a liquid, gas, solid or semiconductor material. There are many gain media that have been employed in laser operation, all of which function to stimulate emission of photons leading to the amplification of light.

By using mirrors, photons are forced to make many passes through the gain medium contained within the optical cavity. As they do so, they stimulate other excited atoms to emit photons of the same frequency and direction. As the photons make multiple passes through the gain medium, the power of light is amplified before being allowed to pass through a partially transparent region in one of the mirrors to form the laser beam. The wavelength of light emitted from the laser is governed by the gain medium used in the laser system.

The majority of MALDI-MS analyses are conducted using organic acid matrices. These matrices absorb light in the UV range of the visible light spectrum. UV laser desorption of organic acid matrices was introduced by Karas and Hillenkamp in the late 1980's as a useful means of allowing the analysis of large biomolecules by mass spectrometry.[1-3] The UV lasers conventionally used in MALDI-MS are nitrogen (λ=337nm) and frequency tripled or quadrupled Nd:YAG (λ=355nm or 266nm) UV lasers.

The majority of MALDI-MS instruments have been designed for use with nitrogen lasers. This has primarily been due to the reduced cost and increased availability of nitrogen lasers in comparison to Nd:YAG lasers. Nitrogen lasers can have repetition rates up to approximately 50Hz and have a lifetime of approximately 2×10^7 to 6×10^7 shots.[4] In this chapter a frequency tripled (λ=355nm) Nd:YAG laser is assessed for MALDI-MS imaging. The benefits of Nd:YAG lasers lie with the high repetition rate and the extended laser lifetime. These lasers can readily achieve repetition rates up to 1KHz, with a lifetime of several 10^9 shots.[4]

Recently with MALDI applications extending into LC-MALDI and MALDI-MS image analysis, high throughput and extended laser lifetimes are important factors to be considered. Image acquisition with N_2 lasers typically runs at approximately 100 shots per pixel. This would mean that for an image run of 100x100 pixels, 1 million shots would be used.

Taking in to consideration the extended lifetime and laser repetition rate, Nd:YAG lasers are an attractive alternative to nitrogen lasers for MALDI-MS imaging experiments. The laser pulse frequency has been found (in conventional MALDI-MS analysis) to increase sample throughput whilst providing spectra of equal quality to lower repetition rate lasers, but with the benefits of greater reproducibility and shorter acquisition times.[5]

Nd:YAG typically emit in the infrared region of the visible light spectrum at a wavelength of 1064nm, but with frequency doubling, tripling and quadrupling, wavelengths of 532nm, 355nm and 266nm can be produced. The wavelength of frequency doubled and tripled Nd:YAG lasers fall within the UV region of the visible light spectrum. These laser configurations can therefore be applied in MALDI-MS analysis.

The effects of laser properties on the desorption process in MALDI have been studied by various research groups. In the studies conducted, the main focus of interest tends to be the laser wavelength, the laser pulse width, the laser fluence (or radiant exposure) and the profile of the laser beam.

The laser wavelength is an important factor in MALDI analysis, with the MALDI process being fundamentally reliant upon this property for absorption of energy by the matrix crystals. Small changes in laser wavelength are seen to have effects on sample ionisation with certain matrices. For example, it has been noticed that matrices such as sinapinic acid and 3-hydroxypicolinic acid provide a much lower response with an Nd:YAG laser than is observed when using a nitrogen laser.[4]

Laser pulse width and laser fluence are features which have also been subject to investigation in relation to MALDI analysis. In UV-MALDI-MS, laser pulse widths of 0.5-10 nanoseconds are typically employed. These short laser pulse widths are thought to avoid the destructive thermal excitation of analyte molecules that are observed with longer pulse widths and which can lead to fragmentation.[6]

The laser fluence is defined as the laser energy per unit area incident on the sample surface. This parameter is of extreme relevance in MALDI-MS as it plays an important role in the yield of desorbed ions and molecules.[7] Like the laser pulse width, the laser fluence has also been linked to the level of fragmentation that can occur during the desorption/ionisation process.[8]

The typical profile of an Nd:YAG laser beam is Gaussian in shape. Recent research has shown that a Gaussian laser profile may influence the MALDI process quite significantly. This is found to be particularly important with respect to imaging, where laser irradiation is static at each acquisition point. This is thought to be due to a lack of homogeneity of laser fluence over the laser irradiation area leading to the occurrence of hotspots within the laser irradiation area. Efforts have been made to create a flat top beam profile to address this issue. In these experiments it has been found that the use of a flat top beam profile can increase the reproducibility of MS ion signals.[9] Other studies have looked at the effects of modulating the beam profile, such that the laser profile is slightly altered for each laser pulse. This form of dynamically altering the laser profile is similar to the changes in nitrogen laser profile that have been observed from shot to shot.[4]

In this chapter an Nd:YAG laser is assessed for MALDI-MS imaging. Measurements of the laser properties have been conducted and a number of imaging experiments have been carried out.

2.2 Materials and Methods

2.2.1 Materials

All MALDI-MS experiments were carried out using a Teem (PNV 001525 SC2) high repetition rate Nd:YAG laser (Teem Photonics, Massachusetts, USA) on an Applied Biosystems/MDS Sciex QStar Pulsar *i* (Ontario, Canada) fitted with an orthoganol MALDI ion source. All chemical reagents were obtained from Sigma-Aldrich (Poole, UK).

2.2.2 Methods

Several methods were used to assess the application of the Teem Nd:YAG laser for MALDI-MS imaging experiments.

Examinations of the laser beam profile, pulse width and peak energy were carried out in collaboration with Dr. Keith Oaks of Elforlight Ltd. (Daventry, UK)

2.2.2.1 *Measuring Laser Spot Size*

The laser spot size is an important feature of the laser in imaging experiments as its dimensions may govern the maximum resolution of images that may be obtained. The laser spot size was measured by burning lines through the matrix coating on a stainless steel MALDI target in the x and y dimensions. A stainless steel MALDI target was spray coated with α-CHCA matrix (25 mg/mL in ethanol, 0.1% TFA). With the laser power set to 5.0μJ the matrix coating was ablated from the target surface in a vertical line. On a separate area of the target the same was carried out in the horizontal direction. Measurements of the width (vertical ablation mark) and height (horizontal ablation mark) were taken on an optical microscope (Olympus CH-2 at 100X magnification).

2.2.2.2 *Laser Energy*

The laser energy was assessed by measuring average power on a Molectron PM10 head and EPM1000 display unit. Measurements were taken whilst the laser was set to a repetition rate of 1kHz, which is the standard pulse frequency used in imaging experiments. A number of measurements were made from 25% to 100% energy, although only briefly beyond 50% (5.0μJ) due to concerns about damage to the fibre optic.

2.2.2.3 *Pulse Width*

The pulse shape was monitored on a Telefunken photodiode with a 100ps rise time, and a 300MHz Tektronix 'scope. Measurements were taken at 25% and 40% laser power.

2.2.2.4 *Beam Profile*

The beam profile from the multimode fibre was recorded using a Spiricon LB3 beam profiler system based on a Pulnix TM6 camera. The raw beam profile from the fibre optic was viewed at a distance of approximately 50mm from the end of the fibre optic at a laser energy level of 5%. A crude attempt was made to focus the beam using a magnifying lens combination with a focal length approximately 40mm, this was carried out using a laser energy of 25%.

2.2.2.5 *Assessing the Effect of Laser Profile on MALDI Imaging*

The literature suggests that hotspots and the static nature of Nd:YAG laser beam profiles may account for the reduced ion signals often observed in imaging experiments. Recently a new laser which modulates the hotspot regions within the laser spot has been introduced.[9] Based on these facts and the results obtained from the measurement of the Teem laser beam profile, several experiments have been carried out to assess the effects of moving the position and/or modulating the laser profile at each pixel during image acquisition.

In normal (static) imaging mode the laser beam is fired at a single point on the sample surface for the pre-determined length of time. The laser is then stopped whilst the sample plate is realigned for MALDI-MS acquisition at the next image pixel.

In dynamic pixel imaging mode the laser beam is fired at the sample surface in the same way, stopping to allow realignment of the plate to the position of the next image pixel. However, whilst data is being acquired for each image pixel, the sample plate is manoeuvred in a figure of eight pattern within the confines of the pixel dimension.

Stationary versus dynamic mode imaging has been assessed by looking at the ion intensities observed in each mode. Text was printed in Arial font size 6 onto normal copy paper using a Hewlet Packard HP2420 printer fitted with a compatible black ink printer cartridge. The sample was coated in approximately 5 mL of α-CHCA (25 mg/mL in ethanol, 0.1% TFA) by airspray deposition. MALDI-MS images of the text were acquired in static and dynamic pixel imaging modes. The sensitivity of the imaging process was assessed by acquiring images at various resolutions (200, 100 and 50 μm). Further experiments were carried out in stationary mode in which the fibre optic was manoeuvred manually to disrupt and vary the speckle pattern of the laser beam profile.

2.3 Results

The laser model under evaluation is a Teem PNV 001525 SC2 (Teem Photonics, France) on loan from Applied Biosystems/MDS Sciex for evaluation purposes. This laser has been fitted to a QStar Pulsar *i* mass spectrometer. It is introduced into the MALDI ion source by means of a fibre optic feed and is controlled by o-MALDI server 5.0 imaging software. According to the manufacturers performance specifications this laser has an energy range of between 15 and 30μJ, a repetition rate scale from 0.01 to 1KHz and a pulse width of 0.5ns. The laser beam profile is described as elliptical with a typical ellipticity ratio of 2:1.

2.3.1 Measuring Laser Spot Size

The laser spot size measurements appear to be approximately 88±13μm in the horizontal dimension (figure 2.1a) and 150±25μm in the vertical dimension (figure 2.1b). Based on these results is would appear that the manufacturers approximation of a beam profile elipticity ratio of 2:1 is correct.

(a)

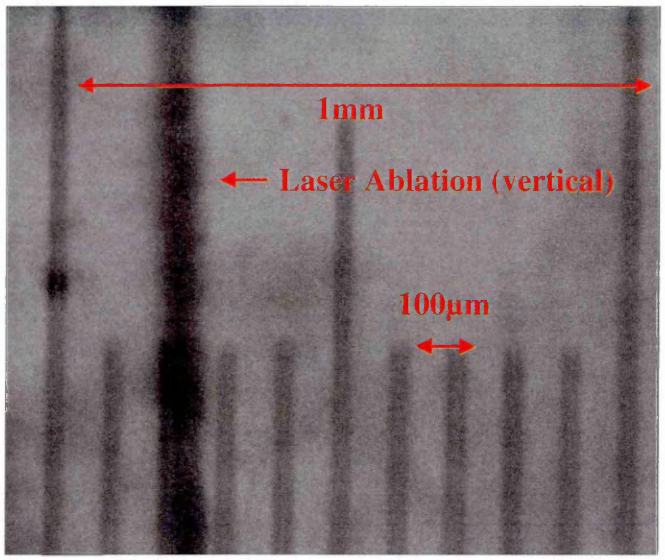

(b)

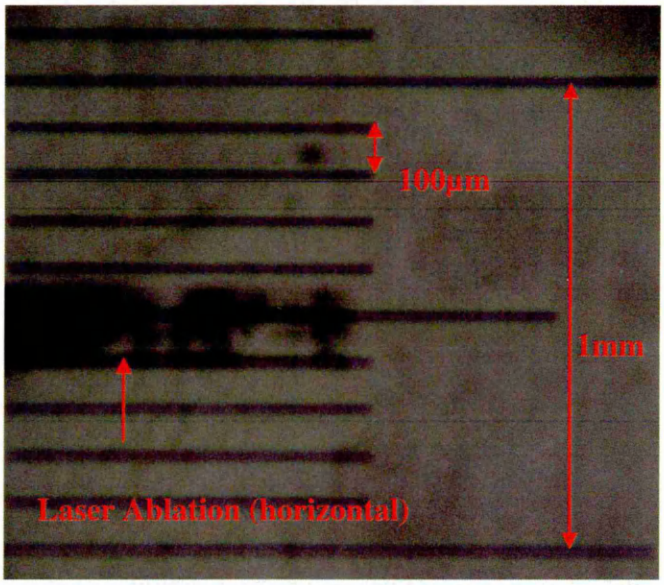

Figure 2.1 Measurements of Laser Spot Dimensions

Optical images (100X magnification) of linear matrix ablation paths are shown to illustrate the laser spot dimensions. The laser spot width (a) and height (b) dimensions were measured using a light microscope by looking at the ablation of matrix from a MALDI target surface. The width of the laser spot appears to be between 75 and 100µm and the laser spot height appears to be between 150 and 200µm.

2.3.2 Measuring Laser Energy

The laser energy was measured to ensure that it correlated with the calibration values given in the instrument control software, i.e. 2.5μJ at 25% energy etc. Measurements were made from 25% to 100% energy, although only briefly beyond 50% (5 μJ) due to concerns about damage to the fibre. On initial switch on, some variance in laser power was observed, with the variation being up to about 50% of the laser power defined by the software calibration. This appeared to settle down after a few minutes operation.

2.3.3 Measuring Pulse Width

The laser pulse widths appeared to be around 800ps FWHM, but this is probably limited by the Tektronix 'scope response time. These results are shown in figure 2.2. The laser manufacturer's quoted pulse width is <500ps. Based on the results obtained and the limitations of the Textronix 'scope response time, 500ps would seem reasonable pulse width.

(a)

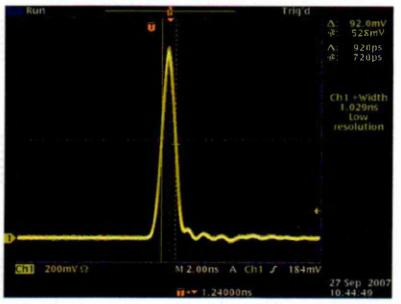

(b)

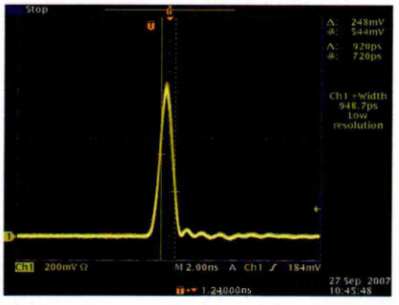

(c)

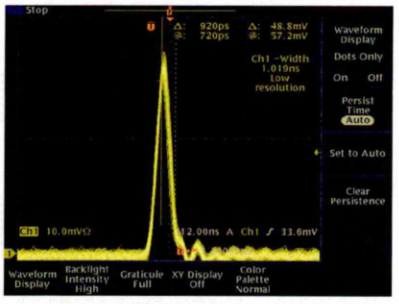

Figure 2.2 Laser Pulse Width Traces

Traces are shown at 25% (a) and 40% (b) laser energy levels. The stability of the pulse width is indicated by observable changes of energy levels over time. At lower energy levels of 5% (c) a slightly higher level of instability was observed. This can be seen in the above illustration as an increase in the thickness of the line indicating laser energy.

2.3.4 Measuring Beam Profile

The profile observed from the raw beam from the fibre optic indicated a speckling effect (figure 2.3a). The speckling effect was still observed after crudely focusing the beam using a magnifying lens combination (figure 2.3b). The speckle is thought to be caused by interference as the beam passes through the fibre optic as a result of the high coherence of the laser. It was found that the speckle pattern could be varied by manually moving the fibre optic cable around.

(a)

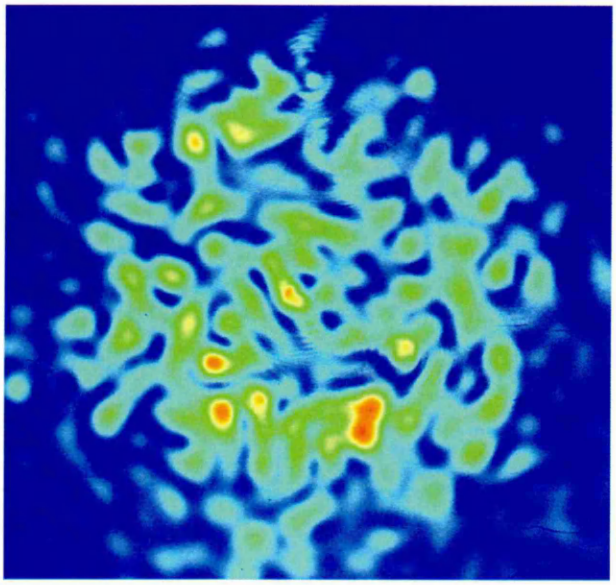

(b)

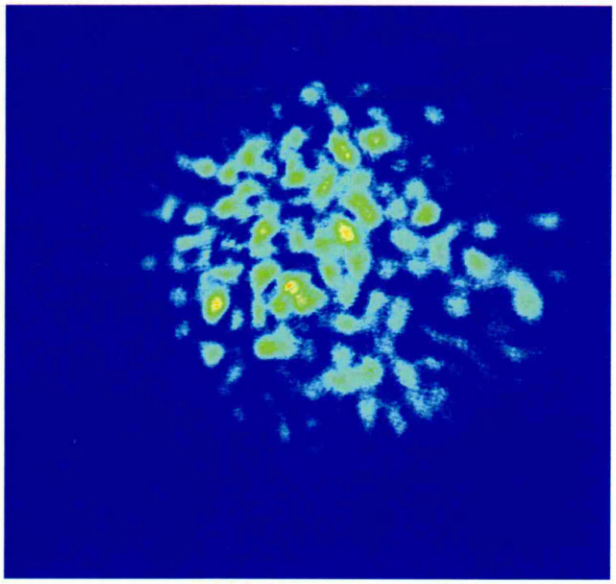

Figure 2.3 Laser Beam Profile Images

Speckle was observed both from the raw laser beam at 5% laser energy and after focusing the laser beam at 25% laser energy. Laser speckle with Nd:YAG lasers is a by-product of use of multi-mode fibre optic feed delivery systems.

2.3.5 Assessing the Effects of Laser Profile on MALDI Imaging

Static and dynamic pixel imaging modes were evaluated by measuring the ion signal of rhodamine 6G at *m/z* 443.5. These are compared to the results obtained by imaging in static imaging mode whilst manoeuvring the fibre optic cable in figure 2.4.

In dynamic pixel imaging mode, high ion yields were observed. The ion yield obtained in static imaging mode was significantly reduced by comparison. However, the image acquired in static imaging mode where the fibre optic cable was manoeuvred to vary the speckle pattern of the laser profile produced ion yields comparable to those obtained in dynamic imaging mode. This would indicate that varying the speckle pattern of the laser has a similar effect in enhancing sensitivity as using the dynamic pixel imaging mode when acquiring MALDI-MS images.

Figure 2.5 shows the images obtained using the dynamic pixel imaging mode at 200, 100 and 50μm resolutions. It can be seen from the images that as the resolution increases, the ion yield is reduced. This is thought to be a result of the laser movement being increasingly confined as the pixel dimensions get smaller. In these experiments, where at a pixel size of 50μm, the ion signal from the ink becomes too low to be able to distinguish the letters in the image. A 50μm resolution image was acquired in which the laser speckle pattern was varied by moving the fibre optic cable whilst the instrument acquired in static imaging mode (figure 2.5d). In this image the letters could clearly be distinguished. This shows that at higher resolutions, varying speckle pattern whilst acquiring in static imaging mode produces higher ion yield than is observed in dynamic pixel imaging mode.

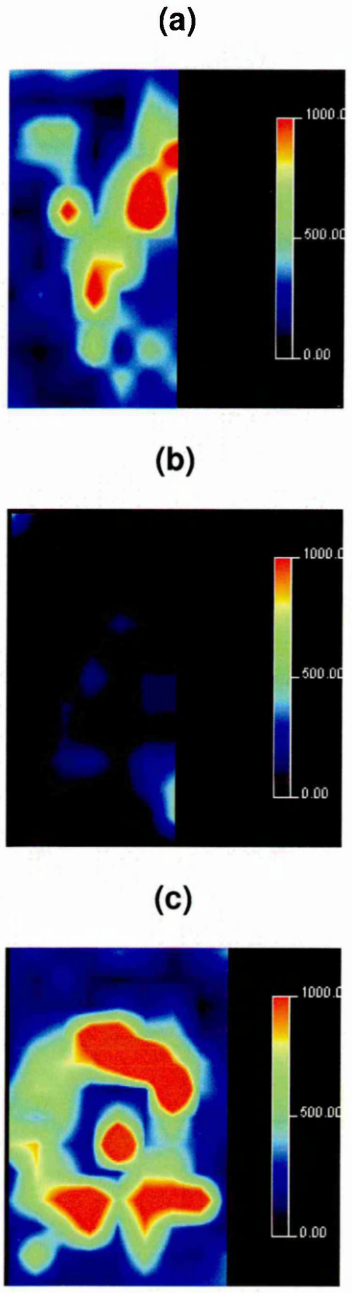

Figure 2.4 Comparing MALDI-MS Imaging modes

Ion images produced at a resolution of 200μm for the protonated molecule of rhodamine 6G (*m/z* 443.5) compare dynamic pixel imaging mode (a) with static ion imaging mode (b) and varying the laser speckle pattern by manouvring the fibre optic(c). Static ion imaging mode produces a much lower ion yield than is observed with either of the other two modes of acquisition.

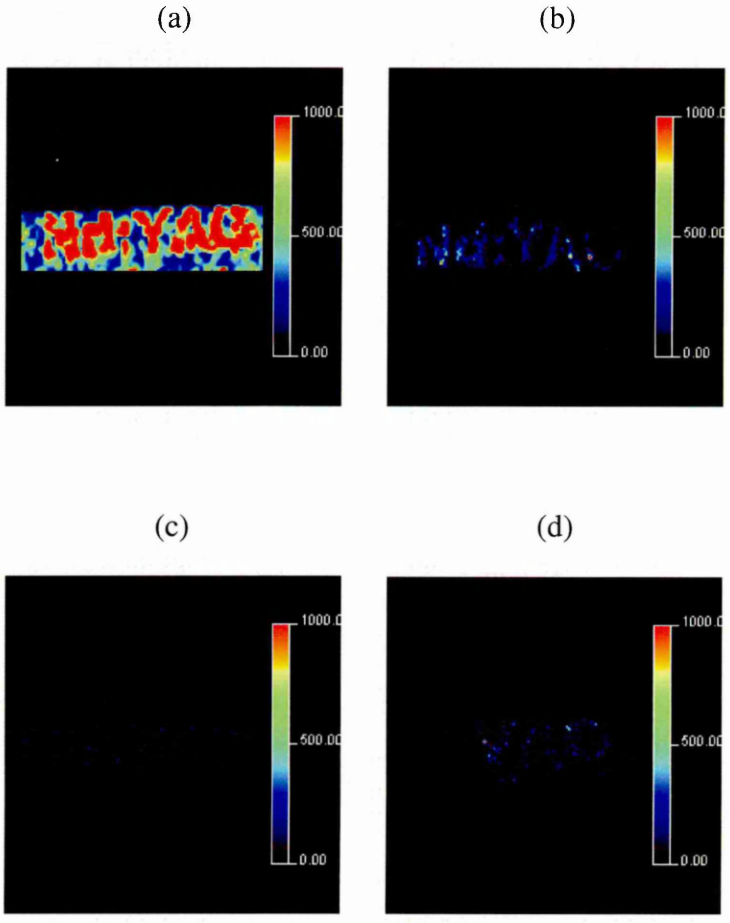

Figure 2.5 Assessing Sensitivity as Image Resolution is Increased

Images acquired in dynamic pixel imaging mode at resolutions of 200µm (a), 100µm (b) and 50µm (c) are shown. It can be seen that as the image resolution increases the ion yield is reduced. In a 50µm resolution image acquired in static imaging mode higher ion signals were observed than in dynamic pixel imaging mode when the speckle pattern was varied by moving the fibre optic cable (d).

2.4 Conclusions

The laser energy and laser pulse width measurements taken for the Teem Nd:YAG laser are in agreement with the manufacturer's specifications. Assessment of the beam profile provided some interesting results. In contrast to the reported Gaussian beam profiles of Nd:YAG lasers[4], it appears that by using a fibre optic feed to introduce the laser into the ion source, the Gaussian beam profile is altered to produce a speckled effect.

The assessment of the high repetition rate Nd:YAG laser for MALDI-MS imaging showed that dynamic pixel imaging mode produces a higher ion yield than is observed in static imaging mode. A similar enhancement of ion signals was observed when the speckle pattern was varied by manoeuvring the fibre optic cable during image acquisition. In this latter mode of image acquisition, higher ion signals are produced at 50μm resolution than were obtained in dynamic pixel imaging mode. This is thought to be due to the fact that the movement of the laser is reduced as the pixel size becomes smaller.

2.4 References

1. HILLENKAMP, F., KARAS, M., HOLTKAMP, D. and KLUSENER, P., 1986. Energy deposition in ultraviolet laser desorption mass spectrometry of biomolecules. *International Journal of Mass Spectrometry and Ion Processes,* **69**(3), pp. 265-276.

2. KARAS, M., BACHMANN, D., BAHR, U. and HILLENKAMP, F., 1987. Matrix-assisted ultraviolet laser desorption of non-volatile compounds. *International Journal of Mass Spectrometry and Ion Processes,* **78**, pp. 53-68.

3. KARAS, M., BAHR, U. and HILLENKAMP, F., 1989. UV laser matrix desorption/ionization mass spectrometry of proteins in the 100 000 dalton range. *International Journal of Mass Spectrometry and Ion Processes,* **92**, pp. 231-242.

4. HOLLE, A., HAASE, A., KAYSER, M. and HOHNDORF, J., 2006. Optimising UV laser profiles for improved MALDI perfomance. *Rapid Communications in Mass Spectrometry,* **41**, pp. 705-716.

5. HATSIS, P., BROMBACHER, S., CORR, J., KOVARIK, P. and VOLMER, D.A., 2003. Quantitative analysis of small pharmaceutical drugs using a high repetition rate laser matrix-assisted laser/desorption ionization source. *Rapid Communications in Mass Spectrometry,* **17**(20), pp. 2303-2309.

6. VERTES, A., GIJBELS, R. and LEVINE, R.D., 1990. Homogeneous bottleneck model of matrix-assisted ultraviolet laser desorption of large molecules. *Rapid Communications in Mass Spectrometry,* **4**(6), pp. 228-233.

7. DREISEWERD, K., SCHEURENBERG, M., KARAS, M. and HILLENKAMP, F., 1995. Influence of the laser intensity and spot size on the desorption of molecules and ions in matrix assisted laser desorption/ionisation mass spectrometry. *International Journal of Mass Spectrometry and Ion Processes,* **141**(2), pp. 127-148.

8. SPENGLER, B., KIRSCH, D. and KAUFMANN, R., 1992. Fundamental aspects of post-source decay in matrix-assisted laser desorption mass spectrometry: I. Residual gas effects. *Journal of Physical Chemistry,* **96**, pp. 9678-9684.

9. SHERROD, S., CASTELLANA, E., MCLEAN, J. and RUSSELL, D., 2007. Spatially dynamic laser patterning using advanced optics for imaging matrix assisted laser desorption/ionization (MALDI) mass spectrometry. *International Journal of Mass Spectrometry,* **262**(3), pp. 256-262.

CHAPTER 3

Indirect Tissue Imaging

3 Indirect Tissue Imaging

3.1 Introduction

Conventionally, MS imaging of biological tissues relates to the analysis of compounds directly from the surface of a tissue. Therefore, MALDI-MS imaging samples are generally composed of thin tissue sections coated with an organic acid matrix. This method of sample preparation has been shown to be successful in the analysis of a broad range of analytes from a number of different tissues.[1-3] It appears however that there are some exceptions. In this chapter some of the problems which may be encountered with direct tissue analysis are introduced and studies carried out to overcome these issues by using an indirect imaging approach are shown.

When analysing low abundance compounds from within a complex mixture it may be beneficial to selectively extract the compound of interest. It has been shown that selective extraction reduces the complexity of the mass spectrum generated and can also function to enrich the sample, increasing the limit of detection for the analyte(s) in question.[4, 5] Taking these factors in to account, it is not surprising that whilst attempting to ionise molecules from an untreated sample surface, as is carried out in many MALDI-MS imaging experiments looking at the distribution of xenobiotic compounds, the same problems are encountered.

As with conventional MALDI analysis, tissues used in imaging experiments become less amenable to direct analysis when the matrix crystalisation process is hindered by salts within the tissue. This effect may be observed to a greater or lesser extent in different tissue types. It has been found that in some cases this problem can be resolved by introducing a series of tissue washing steps prior to matrix application.[6] The salt content of tissues is reduced by washing the sample in increasing concentrations of ethanol. This procedure has been shown to be beneficial for the detection of analytes such as proteins and is examined in the analysis of lipids in later chapters. However, in the detection of analytes presenting high ethanol solubility this method may be detrimental to sample integrity as ethanol washing may induce migration and in extreme cases, complete loss of the analyte.

In this chapter, MALDI-MS imaging is investigated for the detection of a xenobiotic compound in porcine skin tissue. The skin is the largest organ of the body, serving as a barrier to xenobiotic absorption in order to protect the tissues and organs beneath its surface from exposure. Despite this, the skin remains an important vehicle for the administration of a number of drugs, both in the treatment of the skin itself as well as for drugs intended for systemic circulation, where it is required that the first pass effect is avoided. Current methodologies for the determination of dermal absorption include skin extraction measurements, horizontal sectioning and corneum tape stripping, quantitative skin autoradiography and spectroscopic methods.[7-10] Problems commonly associated with these techniques include the requirement for radiolabelled compound, poor sensitivity and the loss of spatial information.

In comparison to existing methods for the analysis of dermal absorption of compounds, MALDI-MS imaging is clearly an attractive alternative. The direct analysis of such samples however, has proven difficult. Skin is an exemplary case in which matrix crystalisation on the tissue surface is found to be problematic. Even after extensive washing in several gradients of ethanol, matrix crystalisation on the tissue surface is poor and ion signals from the sample surface are weak. An indirect tissue imaging approach has been shown to be beneficial in analysing the distribution of xenobiotic compounds in skin cross-sections by MALDI-MS imaging.[11]

In the work described here, a tissue blotting approach incorporating an extraction solvent was used to provide a molecular imprint of the skin tissue on to a cellulose membrane support. The benefits of this approach are two-fold. By producing a molecular imprint of the tissue, not only are any problems associated with matrix crystalisation avoided, but the analytes are in effect selectively extracted from the tissue, thus reducing the complexity of the sample prior to image analysis.

It has been found through preliminary experiments however, that this approach is not directly transferable to the analysis of all compounds. In the approach described by Bunch and co-workers, an imprint of the tissue was made onto a cellulose membrane that had been pre-coated in matrix. It may be assumed that when using this method that the transfer of compounds from the skin to the membrane and the subsequent analyte-matrix co-crystalisation relies upon moisture within the tissue. It is therefore unlikely that compounds which present low water solubility will be transferred to the membrane or indeed co-crystalised with the matrix on the membrane surface. Theoretically, if the transfer of compounds from the tissue surface to a membrane is reliant upon solubility, introduction of a solvent to assist transfer should increase transfer efficiency accordingly. This approach was first described by Mullen *et al.* for the indirect imaging of agrochemicals in soya plants.[12]

In testing this hypothesis for the analysis of compounds in skin, the choice of analyte was extremely important. The compound must exist as a topically applied skin therapeutic, designed to be absorbed through the skin, and it must also be relatively water insoluble. For this experiment hydrocortisone has been found to be a suitable model compound (figure 3.1). Initial experiments show that this compound is not transferred to a cellulose membrane in the absence of a solvent to assist the blotting process.

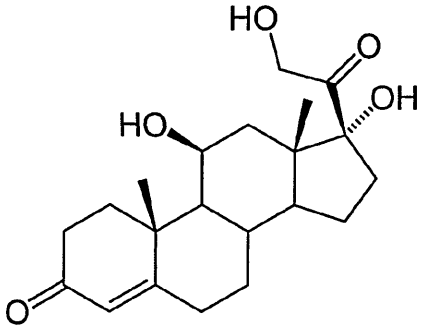

Figure 3.1 The Chemical Structure of Hydrocortisone

The chemical structure of hydrocortisone [11,17,21-trihydroxy-,(11beta)-pregn-4-ene-3,20-dione] is shown.

The corticosteroid hydrocortisone is used as an anti-inflammatory measure in the treatment of eczema and dermatitis. Upon topical application, hydrocortisone diffuses through the skin by both transfollicular and transepidermal routes.[13] This compound also presents low water solubility (0.28 mg/mL), ensuring that the transfer of the analyte from the skin to a membrane surface is unlikely to be affected by residual water in the tissue itself. Furthermore, hydrocortisone presents high ethanol solubility, meaning that the analysis of this compound directly from the skin surface cannot be carried out. In preliminary experiments the vigorous ethanol washing steps required to achieve even the weakest ion signals from the skin surface were found to remove all traces of hydrocortisone from the skin tissue.

A number of experiments have been carried out to assess the solvent assisted blotting approach using the analysis of hydrocortisone from skin tissue as a model system. Arguments against the use of indirect imaging approaches relate primarily to a lack of abundance of the analyte as well as the loss of the original spatial orientation of analytes during the blotting process. The following experiments therefore aim to provide a method of optimizing the transfer of analyte to the membrane as well as to investigate the derogatory effects that introduction of a sample wetting step may have on the spatial integrity of the original sample.

3.2 Materials and Methods

3.2.1 Materials

A generic hydrocortisone cream (0.1% w/w, active ingredient) was used in all skin treatment experiments. Porcine ear skin, obtained from a local abattoir was used as a model of human skin for the investigation.[14] All other reagents were obtained from Sigma-Aldrich (Poole, Dorset, UK).

3.2.2 Methods

3.2.2.1 Assessment of Transfer Efficiency

Porcine skin tissue was treated with 2 mL of a commercial hydrocortisone cream (0.1% w/w active ingredient) over a 2 cm^2 area. The sample was then incubated at 37°C for 1 hour. After the incubation period, the excess hydrocortisone formulation was washed away. Cellulose membranes (2 cm^2) were either applied in the absence of solvent, or as saturated in the various solvents (methanol, ethanol or isopropanol). Where solvents were applied to membranes prior to blotting, the excess solvent was first blotted on to a clean piece of cellulose membrane and membranes were then left to air dry for 60 seconds prior to blotting.

Membranes were manually applied to the treated areas of the skin tissue surface under a pressure of approximately 1 kg/cm^2 for a period of 60 seconds. Hydrocortisone was extracted from the membranes in 1 mL of mobile phase (acetonitrile:water, 70:30) in preparation for subsequent quantitative HPLC analysis. The extraction efficiency of the mobile phase in removing hydrocortisone from the membrane was determined as >99%.

High performance liquid chromatography (HPLC) was used to validate the transfer efficiency of hydrocortisone from the skin to the membrane. Reversed phase HPLC has been used in these experiments as hydrocortisone is a relatively non-polar compound. The HPLC analysis was carried out using a Spherisorb ODS 15 µm column (25cm x 4.6 mm) at a flow rate of 1 mL/minute using a mobile phase composed of acetonitrile:water (70:30). Detection of hydrocortisone was carried out by UV at a wavelength of 242 nm. All experiments were carried out in triplicate.

3.2.2.2 Matrix Optimisation

All analysis of hydrocortisone samples was carried out in positive ion mode. Several matrices were evaluated for the detection of hydrocortisone by spotting a 50:50 mixture of matrix (25 mg/mL in ethanol, 0.1% TFA):hydrocortisone (1 mg/mL in ethanol).

Matrices found suitable for detection of hydrocortisone were also tested for their ability to allow analysis of hydrocortisone from a cellulose membrane. Here, cellulose membranes were spiked with 1 µL volumes of hydrocortisone (1 mg/mL) and spray coated in matrix (25 mg/mL in ethanol, 0.1% TFA).

Further experiments to ensure that matrices were suitable for the detection of hydrocortisone in the presence of other compounds that may be transferred from the skin during the blotting process were also carried out. In these experiments, ethanol assisted cellulose membrane blots of skin treated with hydrocortisone formulation (0.1% w/w) were spray coated in matrix (25 mg/mL in ethanol, 0.1% TFA). For each of the experiments described, an experimental blank was also prepared in the same way in the absence of hydrocortisone.

3.2.2.3 Assessment of Lateral Diffusion

In optimising the extent of lateral diffusion of analytes during the blotting process experiments were carried out to assess the effects of the extent of solvent saturation of the membrane as well as the period of time over which membrane extraction (blotting) took place. This was achieved by treating porcine skin tissue with commercial hydrocortisone cream (0.1% w/w active ingredient) over a defined region using an in-house device which confined the treatment region to a circular area, 6 mm in diameter. The treated tissue was incubated for 1 hour at 37°C. The excess formulation was then washed away from the surface using a 5 second water rinse. Ethanol saturated cellulose membranes were then left to air dry for 30, 60 and 90 seconds prior to blotting.

Each degree of membrane saturation was assessed in conjunction with 30, 60 and 90 second membrane extraction periods. The resulting membrane blots were coated by air-spray from a distance of 10 cm with approximately 5 mL of matrix solution (25 mg/mL α-CHCA in acetone, 0.1% TFA). Acetone was used as a matrix delivery solvent in these experiments to ensure minimal lateral analyte diffusion was induced during the matrix application process. Images were acquired at 200 μm resolution, with a laser dwell time of approximately 2 seconds at each position. Measurements of hydrocortisone distribution in each sample were made using the metric scale of the imaging software.

3.3 Results

3.3.1 Assessment of Transfer Efficiency

Figure 3.2 shows how the HPLC results of the solvent assisted transfer efficiency tests relate to the solubility of hydrocortisone in each of the solvents assessed. As can be seen from this graph, the extraction efficiencies observed follow the predicted trend, correlating with the solubility of hydrocortisone in each of the solvents.

The highest transfer efficiency obtained was through use of an ethanol soaked membrane to assist the blotting process. Using ethanol as the blotting solvent provided more than 80-fold increase in transfer efficiency when compared to relying on residual moisture within the tissue. These results indicate that the solvent assisted blotting approach can be used to increase transfer efficiency and limits of detection considerably.

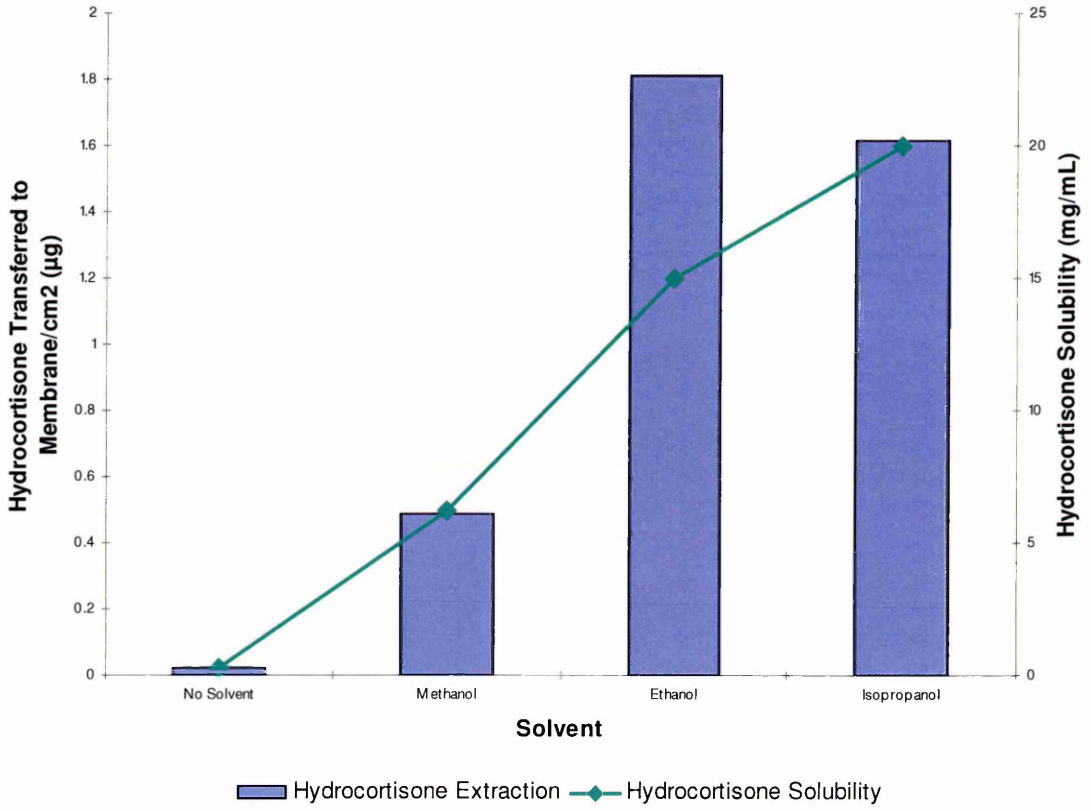

Figure 3.2 Transfer Efficiency and Solubility of Hydrocortisone

Hydrocortisone transfer efficiency increases in accordance with compound solubility in each of the transfer solvents. Ethanol was found to give the highest level of transfer of hydrocortisone to the membrane. It is thought that the level of hydrocortisone transferred to the membrane using isopropanol was reduced due to the viscosity of the solvent.

3.3.2 Matrix Optimisation

The most suitable matrix found for use in imaging of hydrocortisone from membranes was α-CHCA. Examples of detection of hydrocortisone using this matrix on spot targets, from spiked cellulose membranes and from hydrocortisone treated skin tissue blots are shown in figures 3.3 to 3.5. This matrix not only provided the best ion signals of hydrocortisone in each of the examples shown, but is also found to be an ideal matrix for image analysis due to the small matrix crystal size and homogeneity of crystal formation on the membrane surface.[9]

In figure 3.3 we can see in the blank α-CHCA spectrum that matrix peaks exist at *m/z* 363.09 and 363.33. The hydrocortisone molecular ion $[M+H]^+$ has a mass of 363.22, meaning that a mass resolution of more than 3500 is required to resolve the peaks. The mass resolution of the QStar Pulsar *i* instrument is in the region of 10,000 and is therefore adequate to resolve these ions and to allow subsequent image analysis. Further examination also revealed that there is no signal interference from either the cellulose membrane (figure 3.4) or the membrane blot (figure 3.5), as hydrocortisone was readily detected in all samples.

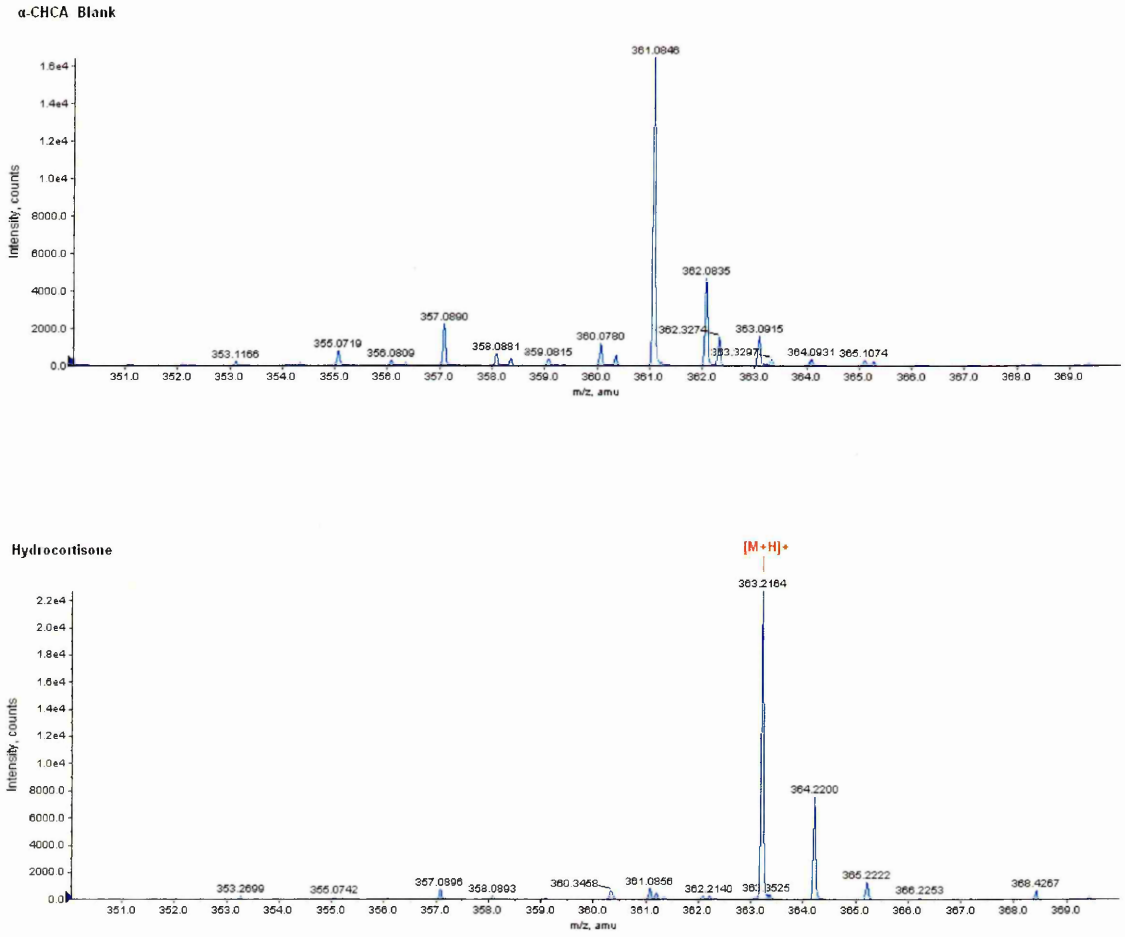

Figure 3.3 Detection of Hydrocortisone on Spot Targets

MALDI-MS spectrum obtained from a spot target sample of 1:1 hydrocortisone (1mg/mL): α-CHCA (25 mg/mL) compared against a MALDI-MS spectrum of an α-CHCA blank.

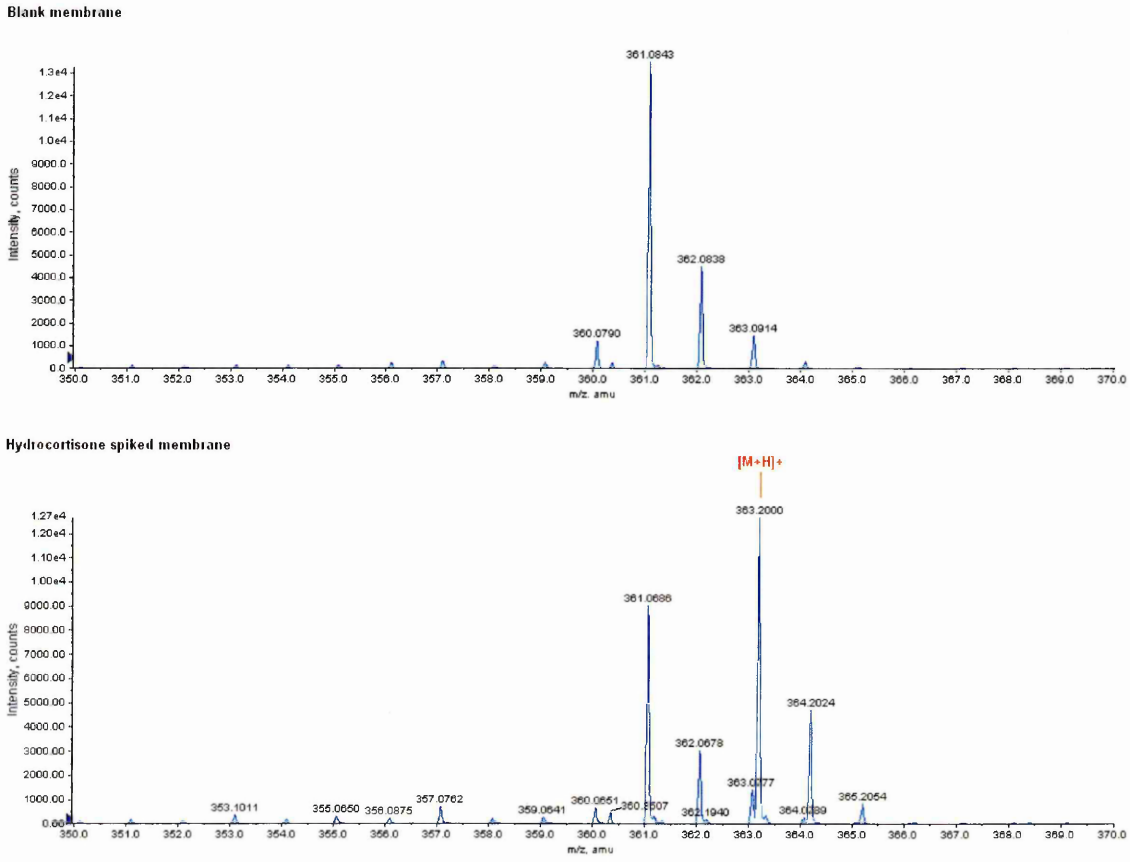

Figure 3.4 Detection of Hydrocortisone on Cellulose Membranes

MALDI-MS spectrum of a cellulose membrane spiked with 1µL hydrocortisone (1mg/mL) and spray coated with α-CHCA (25 mg/mL) compared against a MALDI-MS spectrum of a cellulose membrane coated in the same way with α-CHCA as a blank.

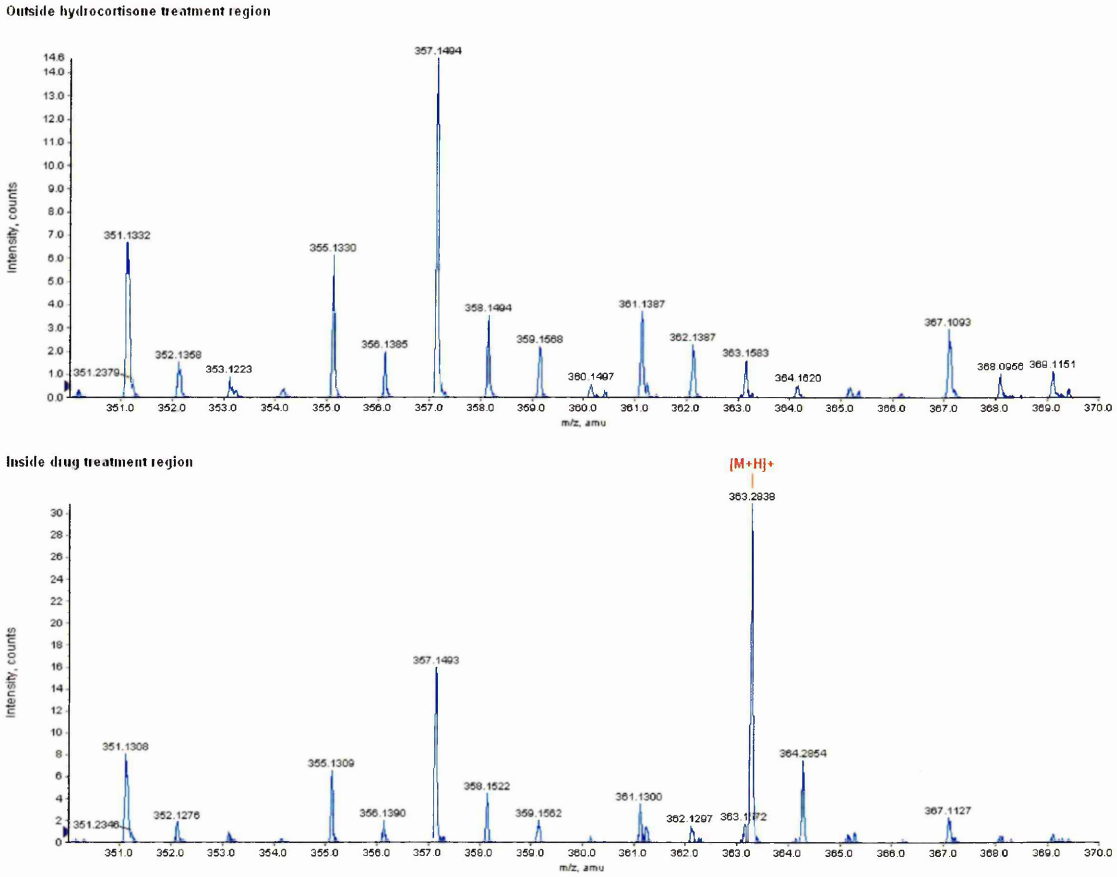

Figure 3.5 Detection of Hydrocortisone on Cellulose Membrane Blots

MALDI-MS spectra taken from an ethanol assisted cellulose membrane blot of skin tissue treated with hydrocortisone formulation (1% w/w) and spray coated in α-CHCA (25mg/mL). Spectra from inside and outside the drug treatment area are shown. The protonated molecule of hydrocortisone is observed at m/z 363.29.

3.3.3 Assessment of Lateral Diffusion

Figure 3.6 shows the data obtained from experiments conducted to assess the lateral diffusion of analyte during the blotting process. It was found that the major factors associated with extended lateral diffusion were the amount of solvent present on the membrane during the blotting process and the length of time over which blotting took place.

With shorter drying times of 30 seconds, high ion signals for hydrocortisone are obtained. This is combined, however, with an extensive degree of analyte spreading.

As the drying time is increased, hydrocortisone ion signals are reduced, but a general reduction in the extent of lateral analyte diffusion is observed. Samples prepared with 60 and 90 second drying times show a positive trend in the amount of hydrocortisone transferred to the membrane as the transfer time is increased. Whilst samples prepared after allowing the membrane to dry for 90 seconds present the least amount of analyte spreading, these samples show less uptake of the analyte than is observed with samples prepared after 60 seconds membrane drying time. Based on these results, it would appear that a membrane drying time of 60 seconds combined with a transfer time of 90 seconds provides the optimum conditions to ensure a good level of sensitivity whilst ensuring analyte spreading is kept to within an acceptable limit.

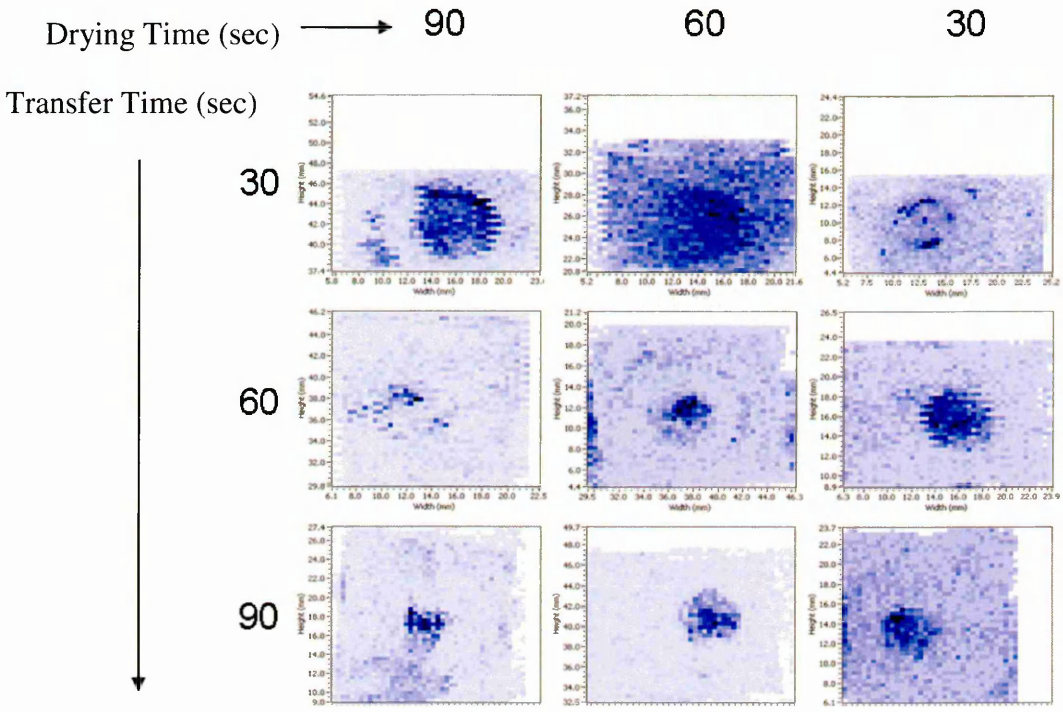

Figure 3.6 Hydrocortisone Lateral Diffusion Images

The images shown are representative of the degree of analyte diffusion using various drying (i.e. wetness of the cellulose membrane) and blotting times in mapping the distribution of hydrocortisone from porcine skin treated over a 6mm diameter region with a 0.1% hydrocortisone formulation. The ion intensity range was adapted individually to each image to best represent the degree of lateral diffusion. As such, comparison between apparent abundance of analyte should be disregarded.

3.4 Conclusion

The solvent assisted blotting approach is useful in allowing MALDI-MS imaging of compounds from tissues not amenable to direct analysis. It has been shown that attention to analyte properties is extremely important in optimising an indirect imaging approach. In this experiment, compound solubility was found to be an important factor. In using an appropriate solvent to assist blotting, a high level of sensitivity for the compound was obtained.

Clearly, incorporation of a wetting step during the sample preparation process does lead to some analyte spreading. It has been shown however that with proper optimisation, lateral migration can be limited to approximately 10%. Whilst this may limit applications, it is thought that for the purpose of some investigations this degree of spreading may not be significant.

3.5 References

1. STOECKLI, M., CHAURAND, P. and CAPRIOLI, R.M., 2001. Direct profiling of proteins in biological tissue sections by MALDI mass spectrometry. *Nature Medicine,* **7**, pp. 493-496.

2. STOECKLI, M., STAAB, D. and SCHWEITZER, A., 2007. Compound and metabolite distribution measured by MALDI mass spectrometric imaging in whole body sections. *International Journal of Mass Spectrometry,* (260), pp. 195-202.

3. ROBINSON, S., WARBURTON, K., SEYMOUR, M., CLENCH, M.R. and THOMAS-OATES, J., 2007. Localization of water-soluble carbohydrates in wheat stems using imaging matrix-assisted laser desorption ionization mass spectrometry. *Rapid Communications in Mass Spectrometry,* **21**(7), pp. 1271-1276.

4. GAO, M., LI, N., ZHANG, J., YANG, P. and ZHANG, X., 2006. The study of three extraction methods for pre-separation and enrichment: Application to the complex proteome separation in rat liver. *Separation and Purification Technology,* **52**(1), pp. 170-176.

5. PAN, C., XU, S., ZOU, H., GUO, Z., ZHANG, Y. and GUO, B., 2005. Carbon nanotubes as adsorbent of solid-phase extraction and matrix for laser desorption/ionization mass spectrometry. *Journal of the American Society for Mass Spectrometry,* **16**(2), pp. 263-270.

6. SCHWARTZ, S.A., REYZER, M.L. and CAPRIOLI, R.M., 2003. Direct tissue analysis using matrix-assisted laser desorption/ionisation mass spectrometry: Practical aspects of sample preparation. *Journal of Mass Spectrometry,* **38**, pp. 699-708.

7. TOUITOU, E., MEIDAN, V.M. and HORWITZ, E., 1998. Methods for quantitative determination of drug localized in the skin. *Journal of Controlled Release,* **56**(1-3), pp. 7-21.

8. ROUGIER, A., LOTTE, C. and MAIBACH, H.I., 1987. In vivo percutaneous penetration of some organic compounds related to anatomic site in humans: Predictive assessment by the stripping method. *Journal of pharmaceutical sciences,* **76**(6), pp. 451-454.

9. FABIN, B. and TOUITOU, E., 1991. Localization of lipophilic molecules penetrating rat skin in vivo. by quantitative autoradiography. *International journal of Pharmacology,* **74**, pp. 59-65.

10. SENNHENN, B., GIESE, K., PLAMANN, K., HARENDT, N. and KÖLMEL, K., 1993. In vivo evaluation of the penetration of topically applied drugs into human skin by spectroscopic methods. *Skin Pharmacology,* **6**(2), pp. 152-160.

11. BUNCH, J., CLENCH, M.R. and RICHARDS, D.S., 2004. Determination of pharmaceutical compounds in skin by imaging matrix assisted laser desorption/ionisation mass spectrometry. *Rapid Communications in Mass Spectrometry,* **18**, pp. 3051-3060.

12. MULLEN, A.K., CLENCH, M.R., CROSLAND, S. and SHARPLES, K.R., 2005. Determination of agrochemical compounds in soya plants by imaging matrix-assisted laser desorption/ionisation mass spectrometry. *Rapid Communications in Mass Spectrometry,* **19**(18), pp. 2507-2516.

13. HUEBER, F., WEPIERRE, J. and SCHAEFER, H., 1992. Role of transepidermal and transfollicular routes in percutaneous absorption of hydrocortisone and testosterone: in vivo study in the hairless rat. *Skin Pharmacology,* **5**(2), pp. 99-107.

14. SIMON, G.A. and MAIBACH, H.I., 2000. The pig as an experimental animal model of percutaneous permeation in man: Qualitative and quantitative observations - An overview. *Skin Pharmacology and Applied Skin Physiology,* **13**, pp. 229-234.

CHAPTER 4

MALDI-MS Imaging for Pre-clinical Applications

4 MALDI-MS Imaging for Pre-clinical Applications

4.1 Introduction

Observing the activity and metabolism of drugs inside the body is an important step in drug development. The potential of MALDI-MS imaging for studying drug distributions is of great interest to the pharmaceutical industry. Researchers hope that this technique may complement existing technologies by allowing simultaneous mapping of and distinction between structurally related drug metabolites; a limitation of existing drug imaging approaches.

Conventionally, drug distribution studies have been reliant upon autoradiographic and immunofluoresence imaging. Whilst these methods enable tracking of the drug compound they are not necessarily able to trace the drug metabolites. Mass spectrometry based techniques have become the industry standard for looking at drug distributions. LC-MS analysis may be used to provide some resolution to the specificity issue[1-3], however crude sampling methods (involving extraction of target compounds from tissue homogenates) do not allow determination of heterogeneous distribution within a tissue. It is with this objective in mind that MALDI-MS imaging is being evaluated for its potential to bridge the gap between autoradiographic imaging and LC-MS analysis.[4, 5]

With the latest prodrug technologies, it is required that imaging techniques are capable of distinguishing between compounds where structures are defined by as little as one atom. Moreover, with therapeutic strategies being directed toward reduced dosing in patients, the analysis must have sufficient sensitivity to detect these compounds at low abundance. For MALDI-MS imaging to successfully achieve this goal, measures must be taken to ensure that compound specificity is maintained and that drug signals are not impaired.

Unlike LC-MS analysis, where extraction of analytes from tissues and chromatographic separation reduces the complexity of samples prior to ionisation, desorption and ionisation in MALDI-MS image analysis is carried out directly from the tissue surface. In our own studies it has been found that fragmentation during the ionisation process can interfere with compound specificity. Structures of the fragment ions of a drug may mimic the molecular ions of drug metabolites, leading to production of 'false' images. This is difficult to resolve, even with MS-MS imaging capabilities.

Furthermore, due to the high level of sample complexity, ion suppression in MALDI-MS imaging is common. Ion suppression may lead to an apparent reduced abundance or complete loss in detection of the compound(s) of interest, either in confined regions of the image or throughout the entirety of the image run. Similarly, with ionisation in MALDI-MS being reliant upon the presence of a matrix, variability in matrix coverage can be seen to add to this effect. Again, either one or both of these factors may lead to the production of 'false' images.

In the following experiments potential methods to overcome these problems using experimental controls and by optimising sample preparation methods are demonstrated. In this study MALDI-MS imaging is investigated for its ability to image the distribution of a prodrug and its active metabolite. The compound chosen for this analysis is a novel anticancer drug which is currently in the early stages of phase II clinical trials.

A large proportion of human cancers present as solid tumours.[6] Effective treatment of solid tumours is limited by the presence of hypoxic regions within tumour tissue. Hypoxia is a rare physiological occurrence associated with cases of severe oxygen depletion such as stroke, arthritis and cardiac arrhythmias. In tumours, hypoxia occurs through combination of the high oxygen demand of dividing cells and irregularities in tissue vasculature. Perfusion deficits as well as the metabolic changes that occur in hypoxia render hypoxic cells resistant to conventional cancer therapies. If left untreated these cells have the potential become reoxygenated, leading to increased likelihood of tumour regrowth.[7]

Much research has been directed toward harnessing the reductive conditions that persist during a hypoxic episode in order to facilitate treatment of solid tumours. Bioreductive drugs available include N-oxides such as tirapazamine, aziridinylnitroimidazoles RSU 1069/RBU 6145 and quinones such as indoloquinone EO9AQ4N.[8]

AQ4N (1,4-bis-{[2-(dimethylamino-*N*-oxide)ethyl]amino}5,8-dihydroxyanthracene-9,10-dione) is a member of the N-oxide functionality group of bioreductive anticancer agents.[9, 10] This novel compound, devised to circumvent the therapeutic resistance induced by hypoxia, has been shown to significantly enhance radiation therapy as well as improving the anti-tumour effects of drugs such as cyclophosphamide and cisplatin.[11,12]

The activation of AQ4N is shown to be largely confined to within tumours. Studies have found that only a low proportion of AQ4N administered to the body is systematically metabolised to the active metabolite AQ4 (<2% of the AQ4N for all doses administered). This low systemic release of the cytotoxic metabolite reduces side effects and allows dosing in patients up to 200 mg/Kg.

Under reduced oxygen conditions and facilitated by bioreductive enzymes, AQ4N undergoes metabolic N-oxide reduction to produce the cytotoxic compound AQ4 (figure 4.1). AQ4 is a DNA affinic which inhibits Topoisomerase II activity, an enzyme which is critical to cellular DNA processing. AQ4 inhibition of this enzyme functions to sychronise cell growth, sensitising cells to fractionated radiotherapy and some forms of chemotherapy. Whilst there are a number of bioreductive drugs available with similar pathophysiological effects, AQ4N has the exclusive capacity to retain activity upon tissue reoxygenation.[6, 13]

AQ4N is an ideal candidate for assessing the potential of MALDI-MS imaging in pre-clinical assessment. As well as being a highly selective compound, the prodrug also presents a high level of structural homology with the active metabolite. The overall aim of this experiment is to validate that the site of bioreductive activation of AQ4N correlates with regions of hypoxia within tumours. This is to be carried out by mapping the distributions of AQ4N and AQ4 in human tumour xenographs, excised from mice previously treated with AQ4N. The following experiments describe the steps taken towards optimising sample preparation for the detection of AQ4N and AQ4 in treated tumour samples.

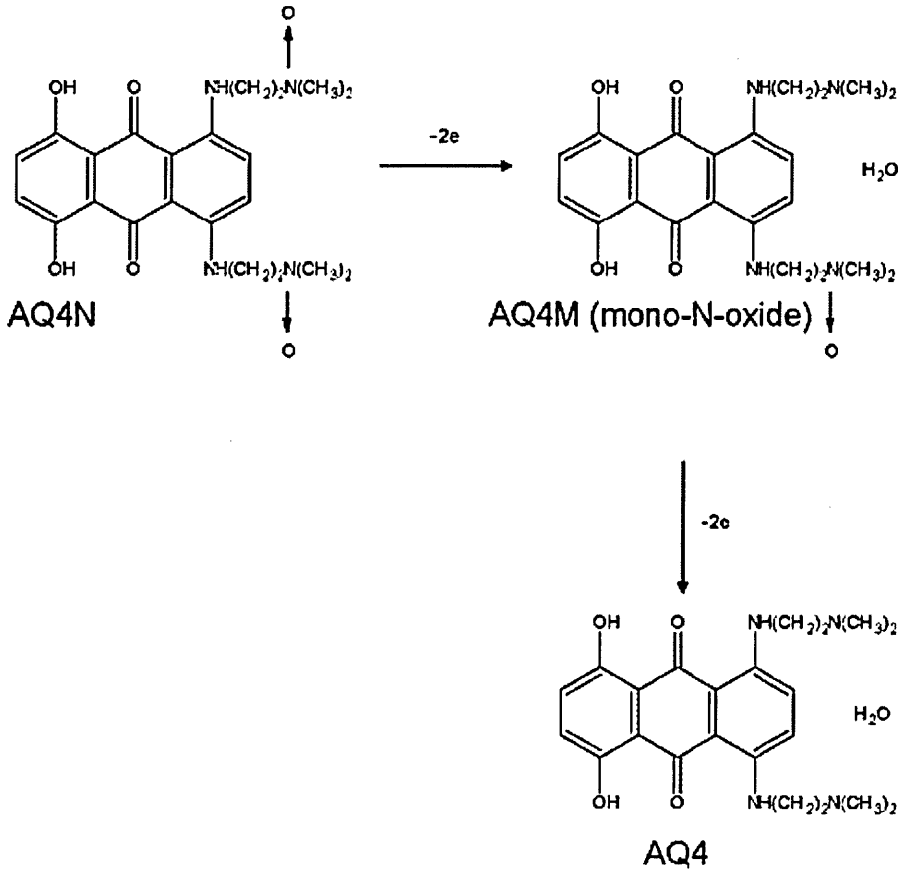

Figure 4.1 Chemical structures of AQ4N and its major metabolites.

Bioreduction of the prodrug AQ4N produces the intermediate metabolite AQ4M. AQ4M is further reduced to form the active compound AQ4. These reactions occur in the highly reductive environment that exists in hypoxia.

4.2 Materials and Methods

In determining the distribution of AQ4N and AQ4 in tumour tissue, it is required that these compounds can be detected simultaneously. Optimisation of matrices and other experimental parameters have been carried out to ensure a high level of sensitivity and selectivity is achieved throughout the analysis.

4.2.1 Materials

AQ4N and AQ4 standards were synthesised as previously described.[14] These compounds and the H460 human tumour xenographts were obtained from the Institute of Cancer Therapeutics, University of Bradford, Bradford, UK. Treated H460 human tumour xenographts were taken from tumour bearing mice after 24 hours treatment with AQ4N (100mg/Kg, intraperitonally (i.p.)). Tumours were flash frozen immediately upon excision and stored at -80°C. All animal experiments were carried out under a project licence approved by the UK Home Office, London, UK. Untreated H460 human tumour xenographts were obtained and stored under the same conditions.

All tumour cryosections were produced using a Leica cryostat (Leica Microsystems, Wetzlar, Germany). Sections were produced at 12 μM thickness in the absence of embedding medium at an operating temperature of -20°C. The sections were placed directly onto disposable aluminium sheets in preparation for MALDI matrix application. All tissue sections used in MALDI-MS image analysis were prepared and run on the same day to avoid sample degradation. All other reagents were obtained from Sigma-Aldrich (Poole, UK).

4.2.2 Methods

4.2.2.1 Matrix Optimisation

A range of matrices were tested as potential candidates for MALDI-MS image analysis of AQ4N and AQ4. All matrices were made up to a final concentration of 25 mg/mL in ethanol, 0.1% trifluoroacetic acid (TFA). AQ4N and AQ4 standards (1 mg/mL) were mixed 50:50 with each of the matrices and spotted onto a stainless steel MALDI target in 1 μL volumes. MALDI-MS spot samples were run manually at a 30% laser power (3.2 μJ).

4.2.2.2 *Detection of Compounds from Tumour Tissue*

Experiments have been carried out to ensure detection of compounds directly from the tissue surface. Both α-CHCA and DHB matrices were tested for suitability for the detection of AQ4N and AQ4 in tumours. Untreated tumour sections were spotted with 1μL volumes of AQ4N and AQ4 at 1.0, 0.1 and 0.01mg/mL concentrations. Samples were then coated with approximately 5mL of matrix (25mg/mL in ethanol, 0.1% TFA) by air-spray deposition and MALDI-MS analysis was carried out manually on the drug spike regions using a laser repetition rate of 1KHz and a laser power of 30% (3.2μJ).

4.2.2.3 *Assessing the Effects of DNA Binding on AQ4 Ionisation*

The DNA binding properties of AQ4 may significantly reduce ionisation of this compound from the tissue surface. An experiment was carried out to assess how ionisation of AQ4 was affected in the presence of DNA and how alteration of experimental pH may function to dissociate AQ4 and enhance ion signals. All samples were prepared in triplicate using stock solutions of AQ4 (1mg/mL) and DNA (5μg/mL). α-CHCA matrix solutions (25mg/mL in ethanol) were used at varying TFA concentrations (0-2.0%) to investigate the effect of pH on AQ4/DNA dissociation. Table 1 illustrates the composition of the samples in more detail.

4.2.2.4 *Imaging of AQ4N and AQ4 in Tumours*

Test image samples were prepared to evaluate the benefits of altering matrix TFA concentration on detection of AQ4N and AQ4 from tumour tissue. Untreated H460 human tumour xenograph tissue sections were spiked with 1μL volumes of AQ4N (1mg/mL) and AQ4 (1mg/mL) and spray coated in matrix with the various TFA concentrations (0.1%, 1.0% and 2.0%).

Imaging of treated H460 human tumour xenograph tissue sections was carried out to determine the distribution of both AQ4N and AQ4 through out the tumour tissue. These experiments were carried out in the presence of experimental controls to ensure selectivity between AQ4N and AQ4.

All images were run at 200μm resolution with a laser power of 30% using a beta test version of the Applied Biosystems/MDS Sciex 'Dynamic Pixel' imaging mode. In this mode, rather than performing stationary laser irradiation at each image voxel position, the sample is moved beneath the laser within the confinements of the user-defined voxel dimensions. This aims to address sensitivity issues associated with the use of an Nd:YAG laser with a Gaussian beam profile.[15]

Standard Solutions	AQ4 (1mg/mL)	DNA (5μg/mL)	α-CHCA (25mg/mL)	H_2O
AQ4+ α-CHCA	1μL	-	5μL	4μL
AQ4+ DNA+α-CHCA	1μL	4μL	5μL	-
AQ4+ DNA+α-CHCA (0.1% TFA)	1μL	4μL	5μL (0.1% TFA)	-
AQ4+ DNA+α-CHCA (1.0% TFA)	1μL	4μL	5μL (1.0% TFA)	-
AQ4+ DNA+α-CHCA (2.0% TFA)	1μL	4μL	5μL (2.0% TFA)	-

Table 1 Sample Composition for DNA/AQ4 Binding Experiments

The table illustrates the composition of samples prepared for MALDI-MS analysis in the determination of the effects of pH on DNA/AQ4 binding.

4.3 Results

4.3.1 Matrix Optimisation

A total of five matrices were evaluated as potential candidates for MALDI-MS image analysis of AQ4N and AQ4. The results of this experiment are shown in figure 4.2, where detection of each of the drug compounds is illustrated as a percentage of the base peak of each spectrum.

AQ4N was detected as both the protonated molecule $[M+H]^+$ at *m/z* 445 and as the sodium adduct $[M+Na]^+$ at *m/z* 467 using all matrices, with the exception of hydroxypicolinic acid (HPA). Similarly, AQ4 was detected as the protonated molecule $[M+H]^+$ at *m/z* 413 using all matrices with the exception of sinapic acid (SA).

As it is required for imaging that both compounds are detected simultaneously, both sinapinic acid and hydroxypicolinic acid are unsuitable matrices for this analysis. Whilst 2-(4-hydroxyphenylazo) benzoic acid (HABA) is shown to provide a reasonable level of sensitivity in the detection of the sodium adduct of AQ4N, this matrix was disregarded due to the poor ion signals observed for AQ4.

Based on these results, dihydrobenzoic acid (DHB) and α-cyano,4-hydroxy cinammic acid (CHCA) were selected for subsequent testing for the detection of AQ4N and AQ4 in tumour sections. Both compounds were readily detected using these matrices. Spectra obtained using α-CHCA and DHB matrices for each of the compounds are shown in figures 4.3 and 4.4 alongside matrix blanks.

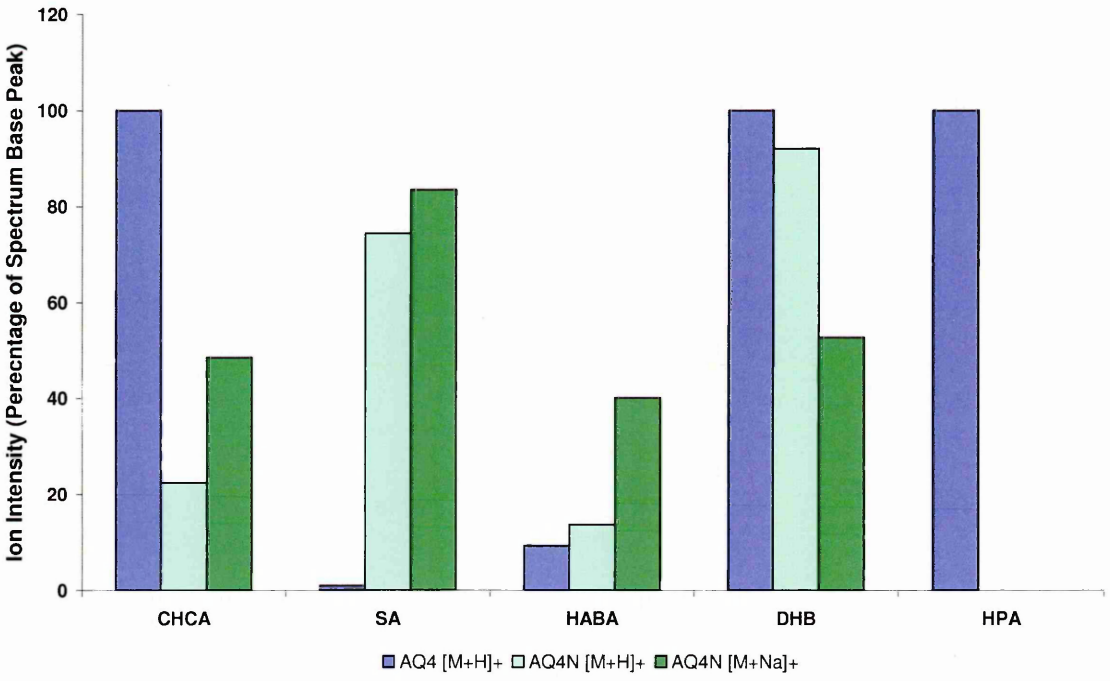

Figure 4.2 Evaluation of Matrices for Analysis of AQ4N and AQ4

Ion intensities of analytes are presented as the percentage of the base peak within each spectrum to allow comparison between spectra of varying ion intensity scale. From these results α-CHCA and DHB are found to be the most suitable matrices as these allow detection of both AQ4N and AQ4.

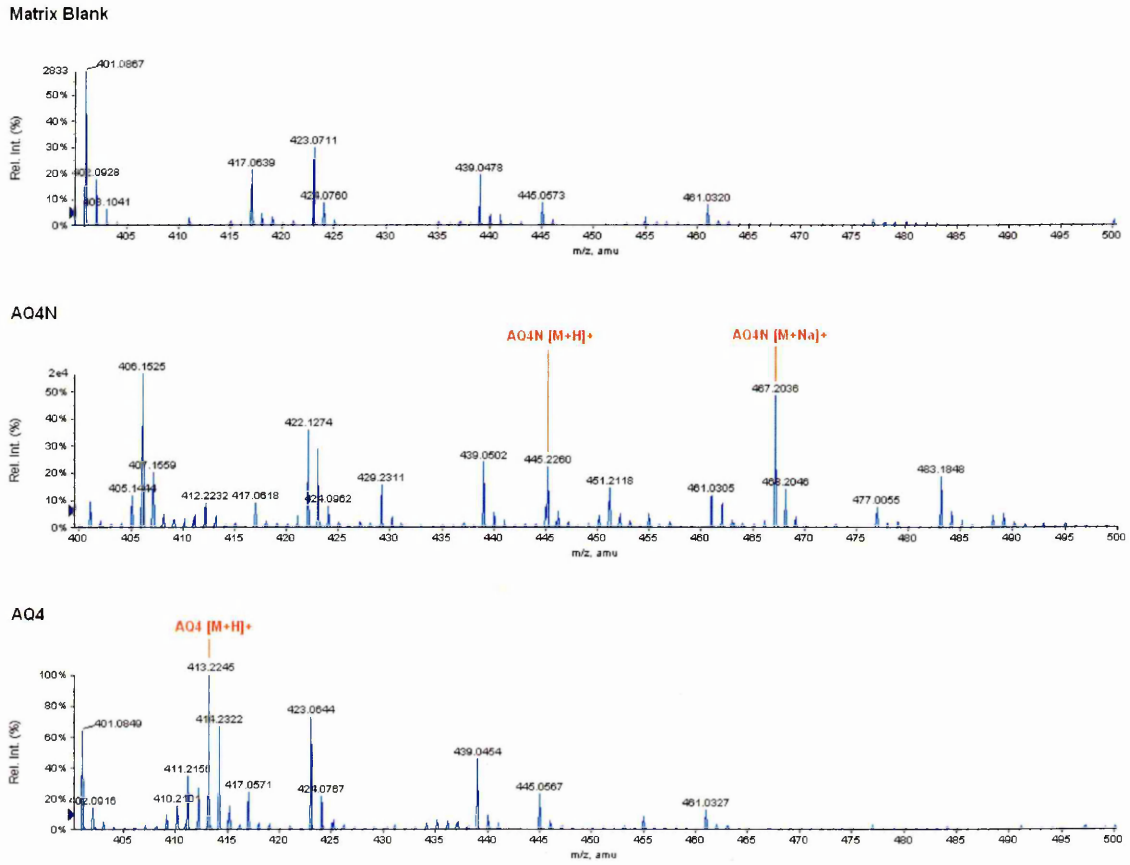

Figure 4.3 AQ4N and AQ4 Detection with α-CHCA Matrix

The protonated molecule $[M+H]^+$ of AQ4 and the protonated molecule and sodium adduct of AQ4N are detected using α-CHCA matrix. Whilst α-CHCA matrix presents peaks with masses closely matching those of AQ4 $[M+H]^+$ and AQ4N $[M+H]^+$, the instrument has sufficient mass resolution to define analyte peaks from the matrix.

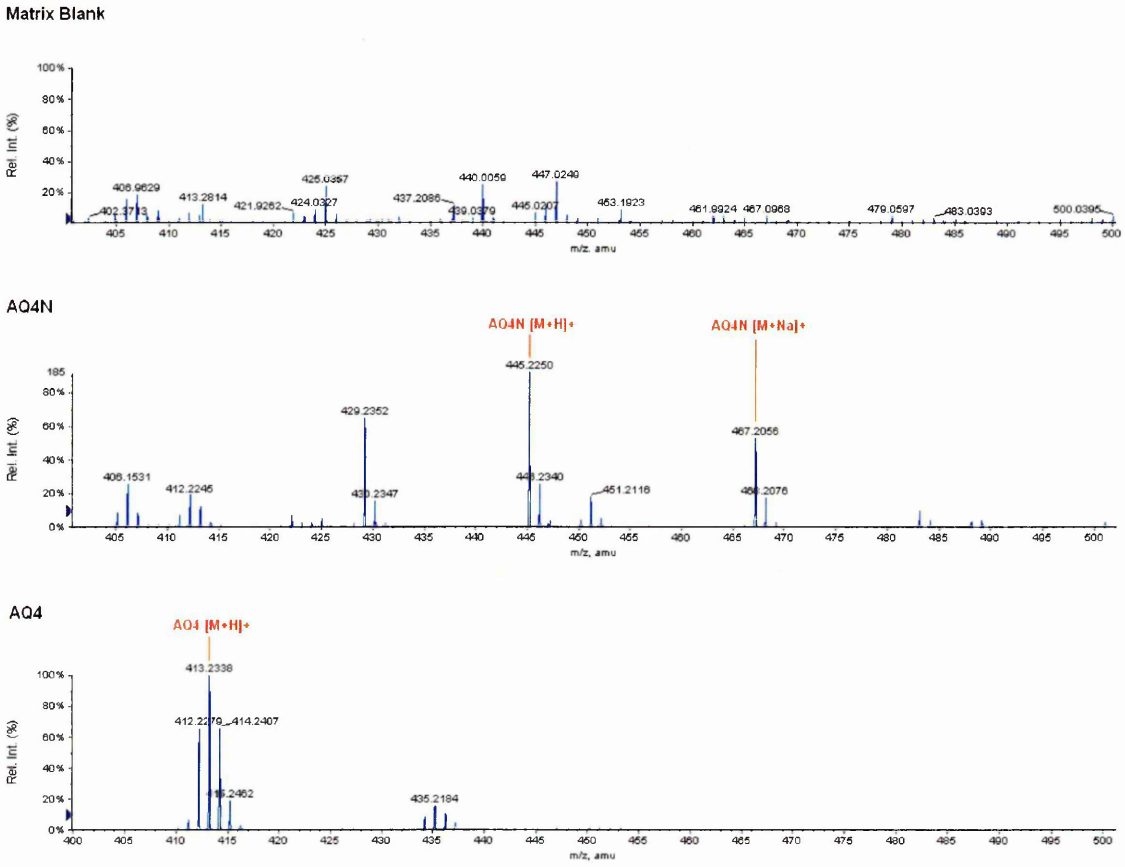

Figure 4.4 AQ4N and AQ4 Detection with DHB Matrix

The protonated molecule $[M+H]^+$ of AQ4 and the protonated molecule and sodium adduct of AQ4N are detected using DHB matrix. Whilst DHB matrix produces ions with mass to charge ratios closely matching those of AQ4 $[M+H]^+$ and AQ4N $[M+H]^+$, the mass resolution required to resolve these peaks (e.g *m/z* 413.2338 from *m/z* 412.2279) is less than 400. Operationally, the Q-Star typically achieves 10,000 mass resolution (FWHM definition), therefore it is sufficient to define analyte peaks from the matrix.

4.3.2 Detection of Compounds Directly from Tumour Tissue

In assessing DHB and α-CHCA for direct tissue analysis of AQ4N and AQ4, it was found that DHB was not a suitable matrix. Intensities of DHB matrix peaks were low and neither analyte could be detected from the tissue surface.

Success in detection of both AQ4N and AQ4 from the drug spiked tissue regions was achieved using α-CHCA, although ion signals were quite weak. Spectra taken from each of the drug spike regions are shown in figures 4.5 and 4.6 alongside spectra taken from blank areas of the tumour tissue.

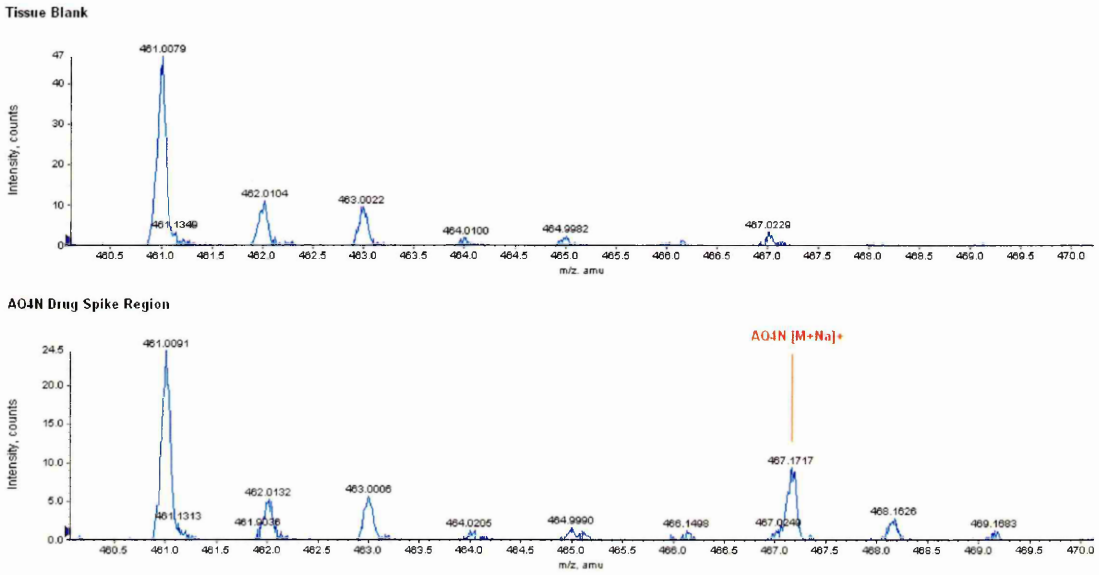

Figure 4.5 AQ4N Detection on Tumour Tissue Using α-CHCA

AQ4N $[M+Na]^+$ was detected from an AQ4N drug spike region of tumour tissue at m/z 467.17. High ion signals were obtained for AQ4N $[M+Na]^+$ but AQ4N $[M+H]^+$ could not be detected.

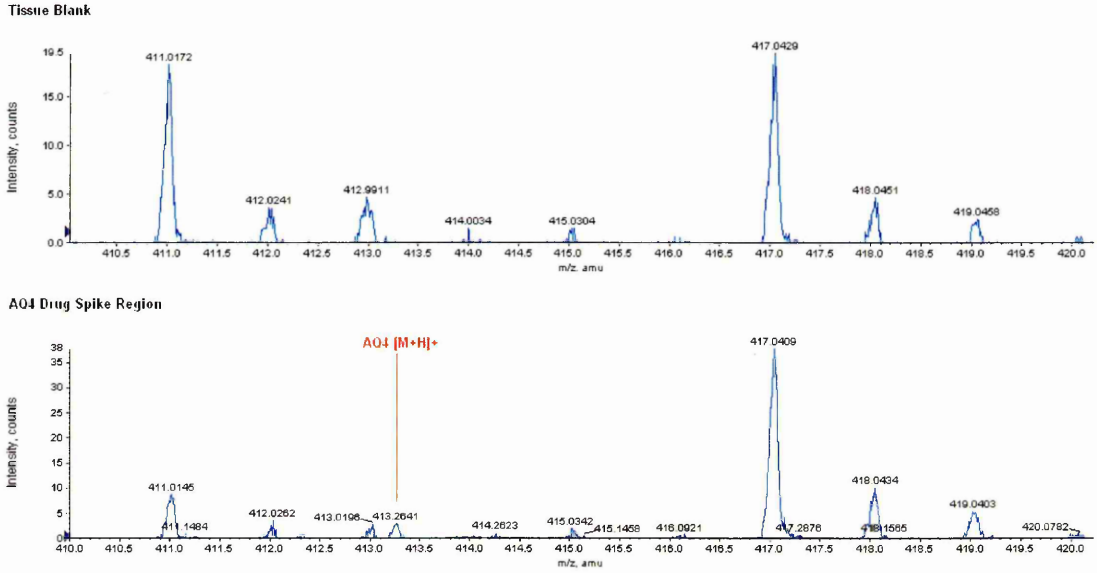

Figure 4.6 AQ4 Detection on Tumour Tissue Using α-CHCA

AQ4 $[M+H]^+$ was detected from an AQ4 drug spike region of tumour tissue at m/z 413.26. Whilst the ion peak was well distinguished from neighbouring ion peaks, the signal response for the AQ4 $[M+H]^+$ ion was weak.

4.3.3 Assessing the Effects of DNA Binding on AQ4 Ionisation

As a result of initial failed experiments in the detection of AQ4 directly from tumour tissue at concentrations <0.1 mg/mL, the effects of DNA binding properties on detection of AQ4 were investigated. Assessment of the effects of pH in allowing dissociation of AQ4 from DNA were also carried out.

The results of the DNA binding and evaluation of experimental pH on AQ4 ion signals are illustrated in figure 4.7. Here, average ion intensities of the AQ4 $[M+H]^+$ normalised against α-CHCA $[M+H]^+$ indicate that although AQ4 ion signals are impaired in the presence of DNA, this effect may be reversed by increasing the amount of TFA added to the matrix.

In the absence of DNA AQ4 is readily detected as the protonated molecule at *m/z* 413, yet when DNA is present AQ4 ion signals are drastically reduced. Figure 4.8 shows the average ion intensities for both AQ4 [M+H]+ and α-CHCA $[M+H]^+$. From these data it can be seen that although an increase in matrix TFA concentration elevates matrix ion signals, the change in AQ4 ion intensity is unrelated. This would indicate that the DNA-affinic properties of AQ4 were responsible for the poor sensitivity observed in the initial direct tissue experiments.

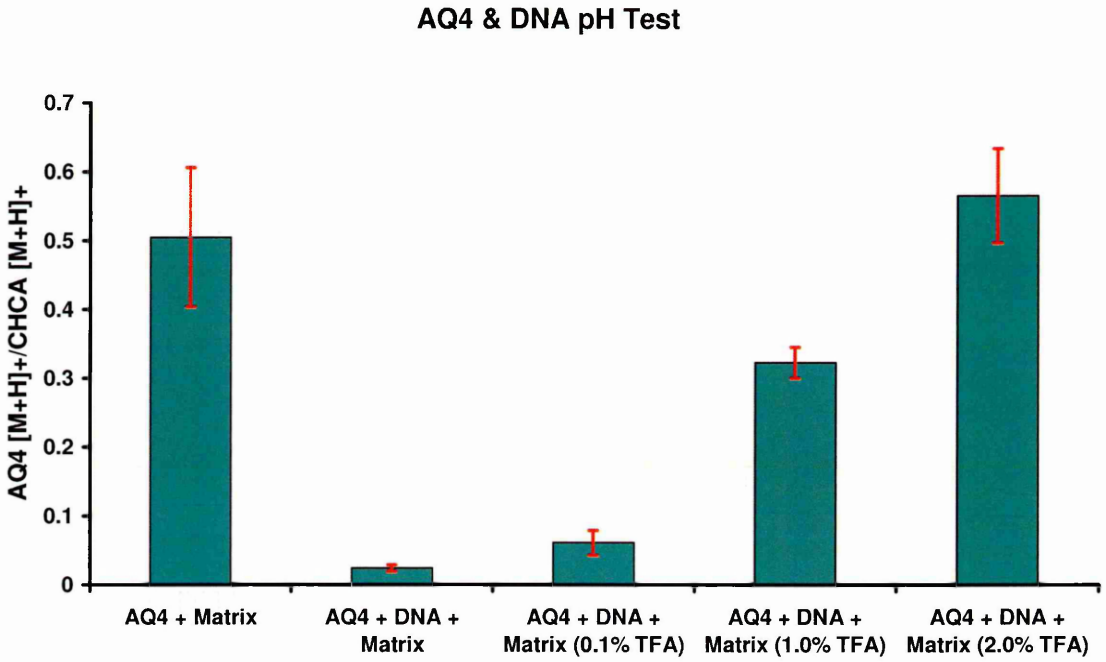

Figure 4.7 The effects of DNA and pH on AQ4 Detection

The AQ4 peak areas of the protonated molecule of AQ4 (*m/z* 413) normalised against the protonated molecule of α-CHCA (*m/z* 190) are shown in the presence and absence of DNA at various TFA concentrations (0-2.0%). The presence of DNA is shown to significantly reduce AQ4 ion signals, but the addition of TFA to the matrix appears to dissociate the AQ4 from the DNA allowing the compound to be detected. This is seen here as an elevation of AQ4 ion signals normalised against the matrix increase in accordance with matrix TFA concentration.

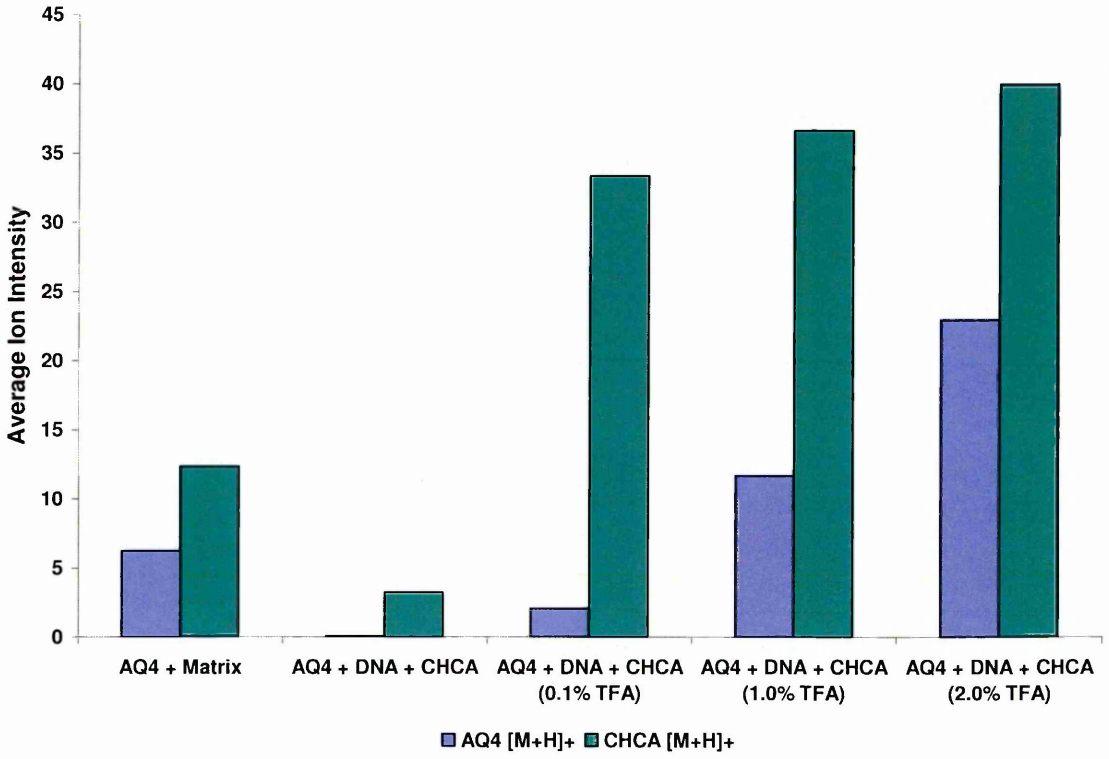

Figure 4.8 The Effects of TFA on AQ4 and α-CHCA Ion Signals

The graph shown illustrates the changes in signal responses for the protonated molecule of AQ4 (*m/z* 413) and the protonated molecule of α-CHCA (*m/z* 190) in the absence of DNA and TFA. Small changes in α-CHCA ion signal as the matrix TFA concentration increases may indicate that the TFA enhances ionisation of this compound. Much larger changes in AQ4 ion signals are observed as the matrix TFA concentration increases. This would indicate that increase in AQ4 ion signals is not dependant upon the matrix, but is dependant up pH.

4.3.4 MALDI-MS Imaging of AQ4N and AQ4 in Tumours

Further investigation into the effects of varying matrix TFA concentration on analyte detection has been carried out by MALDI-MS imaging. Comparison of 0.1, and 2.0% matrix TFA concentrations on image quality has been assessed using drug spiked untreated tumour samples (figures 4.9 and 4.10 respectively).

In experiments where a matrix TFA concentration of 0.1% TFA was used AQ4N $[M+Na]^+$ was detected with high sensitivity from the tumour surface. In these experiments, however, AQ4 could not be detected at all.

In experiments where a matrix concentration of 2% TFA was used AQ4 $[M+H]^+$ was detected with high sensitivity, yet the AQ4N $[M+Na]^+$ signal was noticeably reduced.

It is apparent from these results that whilst a matrix TFA concentration of 2% is found to increase sensitivity for the detection of AQ4, with this level of TFA present AQ4N signals seem to be suppressed. In order to assess the effects of matrix pH on DNA/AQ4 binding (presented in section 4.3.3 of this chapter) further imaging experiments have been carried out using a matrix TFA concentration of 1%. In the AQ4/DNA binding experiments it was found that whilst a matrix TFA concentration of 2% provided the highest ion signals for AQ4, a matrix concentration of 1% also provided a significant increase in sensitivity for AQ4. In order to assess the effects of high TFA concentration on the detection of AQ4N, a 1% TFA concentration is thought to be a reasonable compromise in allowing simultaneous detection of both compounds.

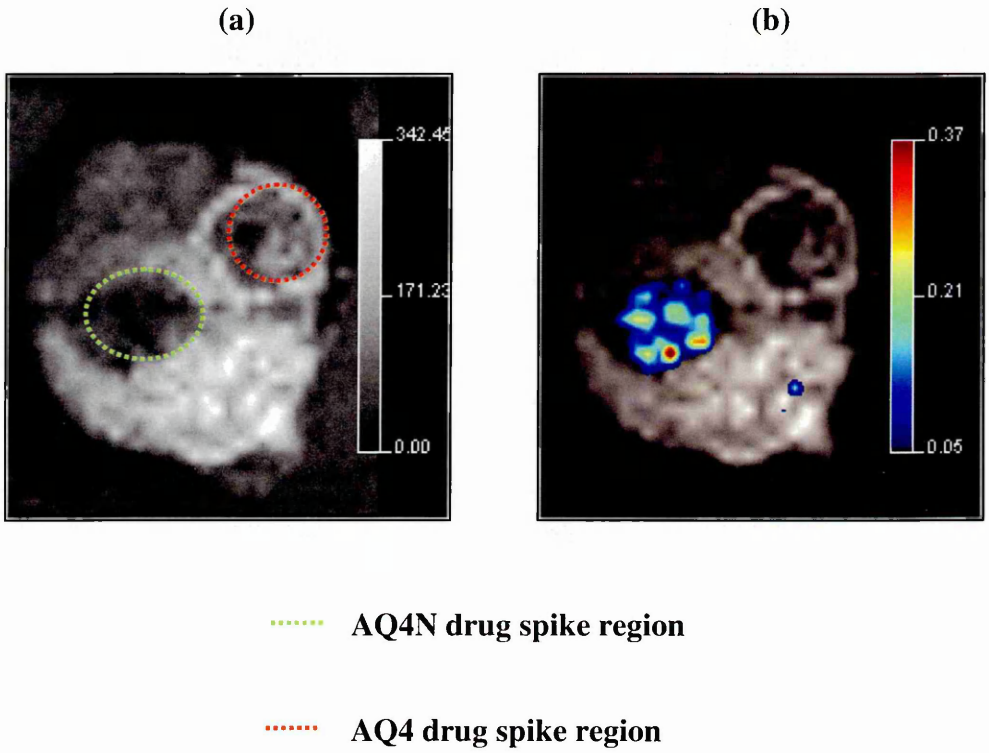

Figure 4.9 MALDI-MS images of Drug Spiked Tissue 0.1% TFA

An image of the potassium adduct of the phosphatidylcholine head groups at *m/z* 222 is shown in black and white (a). This ion is suppressed in the regions of the tissue that have been spiked with the drug compounds (AQ4 and AQ4N), this clearly illustrates the drug spike regions. The distribution of AQ4N $[M+Na]^+$, shown here as a colour overlay (b) is confined to the AQ4N drug spike region. AQ4 was not detected in this analysis. The AQ4N ion image was normalised against the respective ion species of the matrix

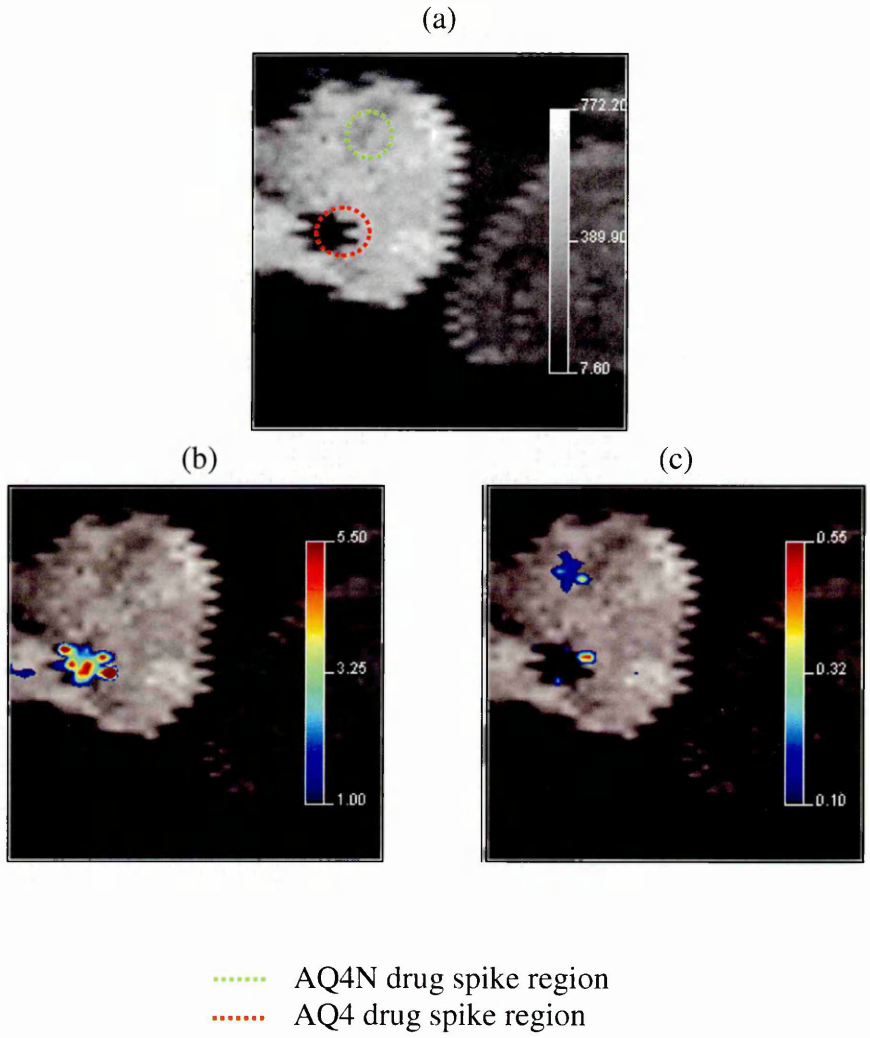

Figure 4.10 MALDI-MS images of Drug Spiked Tissue with 2% TFA

An image of the potassium adduct of the phosphatidylcholine head groups at *m/z* 222 is shown in black and white (a). This ion is suppressed in the regions of the tissue that have been spiked with AQ4. In contrast to images obtained using 0.1% TFA the *m/z* 222 ion is not suppressed in the AQ4N drug spike region. The distribution of AQ4N $[M+Na]^+$ at *m/z* 467, shown here as a colour overlay, is confined to the AQ4N drug spike region (b). This image shows a marked decrease in sensitivity for AQ4N when using matrix with 2% TFA compared to using matrix with 1% TFA. The distribution of AQ4 $[M+H]^+$ at *m/z* 413, also shown as a colour overlay is confined to the AQ4 drug spike region (b) and presents a high level of sensitivity using this matrix TFA concentration. Both AQ4N and AQ4 ion images were normalised against the respective ion species of the matrix.

Figure 4.11 shows the ion images obtained for AQ4 and AQ4N from an AQ4N treated tumour tissue section alongside an image of the distribution of the phosphatidylcholine head group at *m/z* 184. The images include controls for each of the drug compounds to ensure that specificity between drug and metabolite has been maintained. In these images it appears that whilst both AQ4N and AQ4 are detected throughout the tissue, the distributions for each compound are significantly different.

The bicolour image shown in section 4.3.5 (figure 4.13) illustrates the difference in distribution of the compounds within the tissue. Here it can be seen that these compounds co-exist in very few locations throughout the tissue. Interpretation of this image, based on the known activation mechanism of AQ4N, would infer that AQ4N may exist in the oxygenated regions of the tissue and that AQ4 may exist in the hypoxic regions of the tissue. This theory is further evaluated in the next section of results.

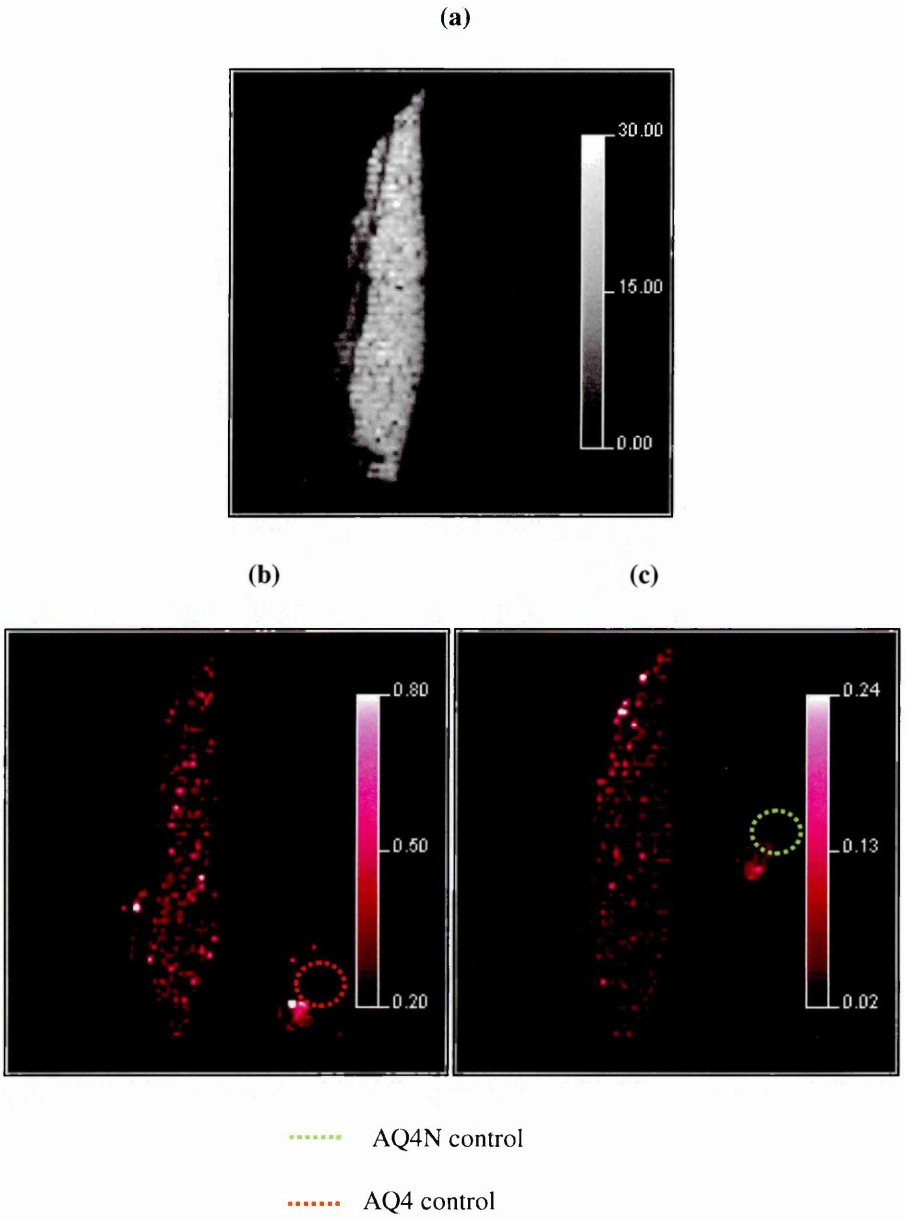

Figure 4.11 Distribution of AQ4N and AQ4 in Treated Tumour Tissue

An image of the distribution of the phosphatidylcholine head group $[M+H]^+$ (*m/z* 184) is shown to illustrate the position of the tumour section within the image (a). Ion images of AQ4 $[M+H]^+$ at *m/z* 413 (b) and AQ4N $[M+Na]^+$ at *m/z* 467 (c) are also displayed. All images have been normalised against the respective ion species of the matrix. A high level of specificity is observed for the detection of each compound, with the controls for AQ4 and AQ4N being clearly defined. There is a marked difference in the distribution of AQ4 in comparison to the distribution of AQ4N.

4.3.5 Using Endogenous Markers to Define Hypoxic Tissue Regions

The endogenous compound ATP has been used as a marker for hypoxia in this experiment. In the images obtained, ATP was readily detected as the fragment ion at *m/z* 409 (corresponding to the loss of H_3PO_4). In the images shown in figure 4.12 it can be seen that the distribution of ATP is highly correlated with the distribution of AQ4N shown in figure 4.11. As ATP depletion is one of the first effects observed in hypoxia, this may imply that AQ4N is largely confined to oxygenated regions of the tissue.

In contrast, AQ4 distribution is found to oppose ATP distribution (i.e. AQ4 is found at elevated levels where ATP is found at reduced levels within the tissue). This may imply that AQ4 is largely confined to hypoxic regions of the tissue. Figure 4.13 shows bicolour images of AQ4 and AQ4N as well as AQ4 and ATP. These images illustrate the contrast between AQ4 and AQ4N distribution as well as the contrast between AQ4 and ATP distribution.

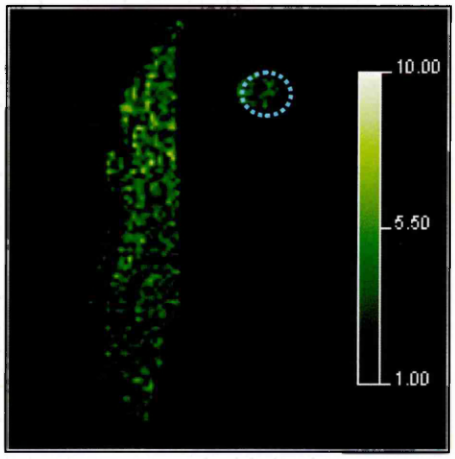

ATP control

Figure 4.12 Image of the distribution of ATP in an AQ4N Treated Tumour

The image displayed is taken from a negative ion image acquisition of the AQ4N treated tumour sample. The distribution of ATP fragment ion at *m/z* 409 reflects the distribution of AQ4N [M+Na]+ shown in figure 4.11 A high level of specificity is observed for the detection of ATP, with the control for this compound being clearly defined.

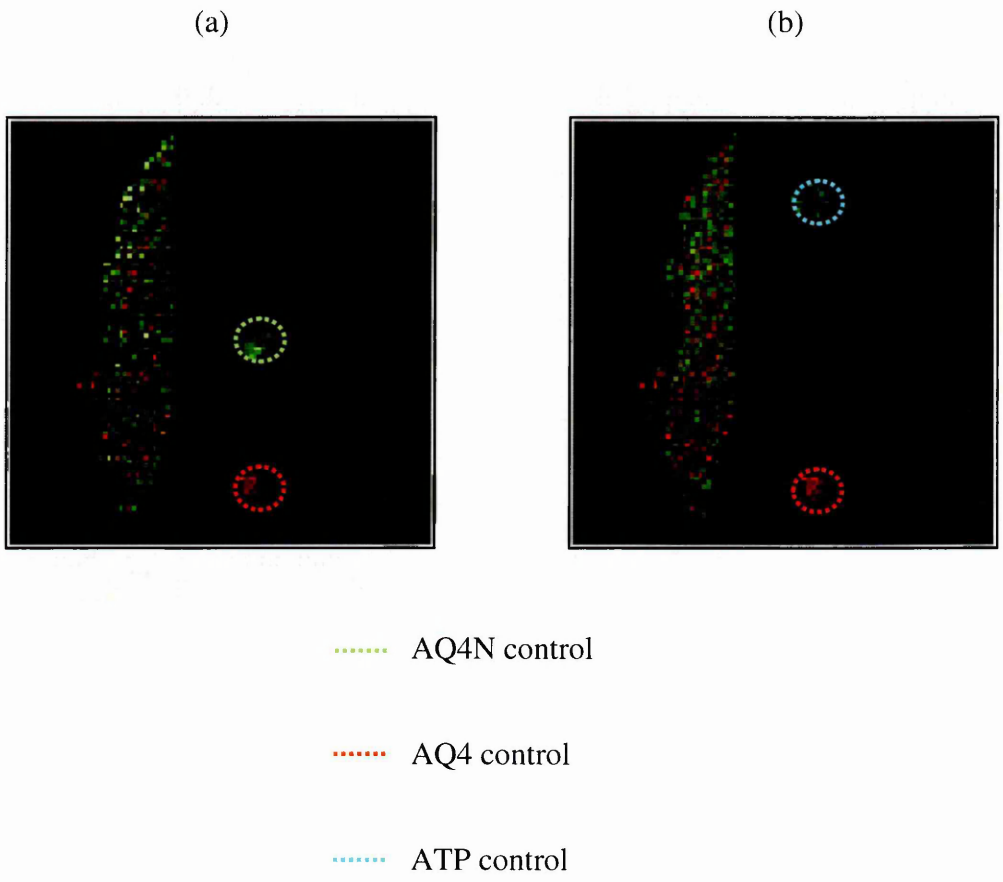

Figure 4.13 Bicolour images of the distribution of AQ4, AQ4N and ATP

The bicolour image of AQ4 (red) and AQ4N (green) shows the contrast between AQ4 and AQ4N distribution (a). The bicolour image of AQ4 (red) and ATP (blue) shows similar contrast in distribution (b). It can also be seen from these images that AQ4N (shown in image a) and ATP (shown in image b) present very similar distributions.

4.4 Conclusion

MALDI-MS imaging has been successfully applied to the analysis of the prodrug AQ4N and its active metabolite AQ4 in AQ4N treated H460 human tumour xenographs. It has been found that AQ4N and AQ4 distributions complement the theoretical assumptions made on the distribution of these two compounds based on the understanding of hypoxia induced activation of AQ4N.

Regions of hypoxia have been defined in these analyses by the reduced abundance of ATP in oxygen depleted regions. It appears from the results obtained that AQ4N distribution correlates with the detection of typical levels of ATP expected in normal oxygenated tissue. Contrasting images of AQ4 distribution suggest that elevated levels of AQ4 are largely confined to hypoxic regions (i.e. those where ATP abundance is reduced). This evidence further validates the highly selective nature of this drug.

The DNA binding properties of AQ4 have been shown to contribute to reduced sensitivity, and in some cases complete loss, in the detection of AQ4 both in the presence of DNA and directly from the tumour tissue surface.

These experiments illustrate the importance of sample preparation in the application of MALDI-MS imaging for pre-clinical analysis and also indicate a necessity for collection of preliminary evidence of sample constituents. It is clear from this analysis that by underestimating the importance of optimisation of sample preparation procedures, false conclusions may be made. In the absence of preliminary experiments (LC-MS of tissue homogenates, for example) to crudely determine the expected presence of analytes in a sample, it is possible that the existence of AQ4 in these treated tumour sections may have been overlooked.

4.5 References

1. HSIEH, Y., MERKLE, K., WANG, G., BRISSON, J. and KORFMACHER, W.A., 2003. High-performance liquid Chromatography-atmospheric pressure photoionization/tandem mass spectrometric analysis for small molecules in plasma. *Analytical Chemistry,* **75**(13), pp. 3122-3127.

2. HSIEH, Y., WANG, G., WANG, Y., CHACKALAMANNIL, S. and KORFMACHER, W.A., 2003. Direct plasma analysis of drug compounds using monolithic column liquid chromatography and tandem mass spectrometry. *Analytical Chemistry,* **75**(8), pp. 1812-1818.

3. KORFMACHER, W., 2005. Foundation review: Principles and applications of LC-MS in new drug discovery. *Drug Discovery Today,* **10**(20), pp. 1357-1367.

4. HSIEH, Y., CHEN, J. and KORFMACHER, W., 2007. Mapping pharmaceuticals in tissues using MALDI imaging mass spectrometry. *Journal of Pharmacological and Toxicological Methods,* **55**(2), pp. 193-200.

5. REYZER, M.L., HSIEH, Y., NG, K., KORFMACHER, W.A. and CAPRIOLI, R.M., 2003. Direct analysis of drug candidates in tissue by matrix-assisted laser desorption/ionisation mass spetrometry. *Journal of Mass Spectrometry,* **38**, pp. 1081-1092.

6. LOADMAN, P.M., SWAINE, D.J., BIBBY, M.C. and WELHAM, K.J. PATTERSON, L.H., 2000. A preclinical pharmacokinetic study of the bioreductive drug AQ4N. *Drug metabolism and disposition: the biological fate of chemicals.,* **29**(4), pp. 422-426.

7. KNISELY, J.P. and ROCKWELL, S., 2002. Importance of hypoxia in the biology and treatment of brain tumours. *Neuroimaging Clinics of North America,* **12**(4), pp. 525-536.

8. WORKMAN, P. and STRATFORD, I.J., 1993. The experimental development of bioreductive drugs and their role in cancer therapy. *Cancer Metastasis Reviews,* **12**(2), pp. 73-82.

9. PATTERSON, L.H., 1993. Rationale for the use of aliphatic N-oxides as prodrug DNA binding agents. *Cancer Metastasis Reviews,* **12**, pp. 119-134.

10. PATTERSON, L.H., CRAVEN, M.R., FISHER, G.R. and TEESDALESPITTLE, P., 1994. Aliphatic amine N-oxides of DNA-binding agents as bioreductive drugs. *Oncology Research,* **6**, pp. 533-538.

11. FRIERY, O.P., GALLAGHER, R., MURRAY, M.M., HUGHES, C.M., GALLIGAN, E.S., MCINTYRE, I.A., PATTERSON, L.H., HIRST, D.G. and MCKEOWN, S.R., 2000. *Enhancement of the anti-tumour effect of cyclophosphamide by the bioreductive drugs AQ4N and tirapazamine. British Journal of Cancer,* **82**(8), pp. 1469-1473.

12. GALLAGHER, R., HUGHES, C.M., MURRAY, M.M., FRIERY, O.P., PATTERSON, L.H., HIRST, D.G. and MCKEOWN, S.R., 2001. The chemopotentiation of cisplatin by the novel bioreductive drug AQ4N. *British Journal of Cancer,* **85**, pp. 625-629.

13. FORTUNE, J.M. and OSHEROFF, N., 2000. Topoisomerase II as a target for anticancer drugs: when enzymes stop being nice. *Progress in Nucleic Acid Research and Molecular Biology,* **64**, pp. 221-253.

14. PATTERSON, L.H., 1989. Anthraquinone anticancer compounds with (disubstituted amino-N-oxide) alkylamino substituent. UK Pat. GB 2, pp. 237–283.

15. HOLLE, A., HAASE, A., KAYSER, M. and HÖHNDORF, J., 2006. Optimizing UV laser focus profiles for improved MALDI performance, *Journal of Mass Spectrometry,* **6**, pp. 705-716.

CHAPTER 5

Pre-processing of MALDI-MS Image Data

5 Pre-processing of MALDI-MS Image Data

5.1 Introduction

The information gathered in MALDI-MS imaging is highly complex by nature. There are many variables besides those intended for analysis that may cause difficulties in interpreting experimental results. These variables can to some extent be separated in to two different categories; sample induced variability and analytically induced variability.

5.1.1 Analytically Induced Variability

Analytically induced variability relates primarily to the MALDI-MS process itself, where the complex nature of samples being analysed gives rise to spectrum-spectrum changes in levels of ion suppression. Ion suppression is thought to occur as a result of the differences in proton affinity between molecules, with a limited availability of protons providing a competitive environment for the ionisation process.

Whilst the pattern of suppression may be relatively constant in replicate samples or where analytes possess high proton affinity, in sampling chemically diverse material such as biological tissue (or where analytes present a particularly low proton affinity), suppression patterns may alter significantly from one spectrum to another. This may cause problems in assigning true relativity to analyte abundance, and in extreme cases can cause difficulties in interpretation of data.

Problems relating to ion suppression can be reduced to some extent by optimising the sample preparation process. Optimisation can provide an increase in the sensitivity of analysis for a particular compound or group of compounds and may aid in reducing the prevalence of false negatives in extreme cases of analyte suppression. Optimisation does not, however, alleviate the issue of ion signal variance attributed to ion suppression.

With suppression effects occurring as a result of the competitive nature of the ionisation process, it is unlikely that this effect can be avoided. Moreover, with the subject of suppression being of such high complexity, it is difficult to contemplate its correction via post-acquisition data pre-processing.

5.1.2 Sample Induced Variability

Post-acquisition data pre-processing is largely concentrated on other aspects of experimental error which may be more susceptible to manual control. Other aspects considered relate largely to the sample itself as opposed to the analytical process. Several effects are described which may alone, or in combination, contribute to generation of experimental errors in image data. The first of these effects occurs due to adduct formation and may be more evident in small molecule analysis.

5.1.3 Adduct Processes

During the MALDI process molecules may be ionised by proton addition or by cationization with alkali metal ions. The problem this raises in MALDI-MS imaging relates to the reproducibility of the adduct process between image spectra.[1]

Whilst the exact mechanism of the adduct process may remain elusive, its effects cannot be ignored when attempting to give a semi-quantitative representation of analyte abundance throughout the tissue. The common approach used to address this problem in MALDI-MS imaging tends to be to ignore the different adduct forms and to produce images of signals measured from the adduct that provides the highest response.

This approach may be acceptable where sample salt content is relatively homogeneous throughout the tissue. In detecting compounds from tissue presenting widespread variation in salt content however, this approach may provide a distorted representation of true analyte abundance. With large scale variation in tissue salt content, variability in adduct formation can be quite prominent. This effect is often observed to a greater extent in samples such as brain tissue, plant tissue and whole body sections which contain two or more fundamentally similar but not identical tissue types.

As the salt content changes from one tissue type to another, the observed ratio between adduct signals may change extensively. It is possible in imaging such samples that what might appear in the final ion image as a marked increase/decrease in analyte abundance, may on closer examination actually be a change in the ratio between adduct form signals. Whilst this issue is widely acknowledged, there are currently no reports of a suitable solution. The use of sample washing steps to remove tissue salts prior to matrix application has been introduced to facilitate effective matrix crystalisation. This method provides a general reduction in salt content, but may not improve the overall homogeneity of salt distribution. A method of post-acquisition data pre-processing that solves issues arising from adduct variation would be useful in MALDI-MS imaging research.

5.1.4 Matrix Coverage and Crystalisation

Further sample related issues associated with production of false images are attributed to the homogeneity of matrix coverage and variance in effective matrix crystalisation. As the MALDI process fundamentally dictates, ionisation occurs largely through energy interactions with matrix crystals. It is unsurprising therefore, that in regions where the abundance of matrix crystals is reduced, a general decrease in the ion intensity of spectra is observed. Clearly, when determining relative analyte abundance, a change in the overall ion intensity scale also results in reduced signal for analytes in those areas. In images it would appear that less analyte is present in these compromised regions of the sample.

Variation in the ion intensity scale may arise as a result of poor matrix application, where matrix is unevenly distributed across the sample surface; or through ineffective matrix crystalisation, in regions where the salt content of the tissue is high.

Since the advent of MALDI-MS imaging, much research has been devoted to matrix application. Various deposition devices and automated spotting systems have been developed to regulate the matrix application process. The 'ImagePrep' station (Bruker Daltonik GmbH, Bremen, Germany) uses vibrational vapourisation to gently deposit small matrix droplets onto the tissue surface under controlled conditions.[2]

The Portrait 630 reagent multi-spotter provided by Labcyte (California, USA) allows matrix application via acoustic droplet ejection. This device can deposit volumes of 170 pL onto the sample surface.[3] Shimadzu Biotech (Kyoto, Japan) has developed the CHIP1000 chemical printer that can deposit 100 pL volume droplets of solutions onto a sample surface using piezo-electric technology.[4]

These systems have resolved the issue of normalising the volume of matrix applied over the tissue and also aid in preventing extensive analyte spreading. The systems fail however, to address the problem of variance in matrix crystalisation which is associated with high abundance of salts in the tissue. As a result the main attribute of these systems is in retention of the distribution of analytes as opposed to resolving ion intensity scale variation.

Further work has been published in the hope of assessing the crystalisation issue, here a technique involving a two-stage matrix application is described, where samples are 'seeded' with a small amount of matrix by airspray deposition before automated matrix spotting is carried out. It is reported that this method of application provides homogeneous matrix spots across the sample surface. These seeded matrix spots are said to be abundant in minute matrix crystals which improve peak intensity and signal to noise ratio.[5]

Sample washing may be found to reduce salt content of tissues considerably, however this does not resolve the adduct variation issue completely. Moreover, in some cases washing may result in the removal of analytes as well as salts.[6] Also, with residual salts left in the tissue after washing, adduct process variation remains a problem.

5.1.5 MALDI-MS Image Normalisation

Initial publications regarding pre-processing of MALDI-MS acquired image data have concentrated on reducing spectrum to spectrum intensity scale changes alone. This work has formerly been related to the analysis of high mass analytes, where variation in adduct processes are often less important. For the purpose of small molecule analysis however, it is important that adduct process variation is taken into account as well.

The simplest means of over-riding matrix abundance issues is to normalise image spectra against a recorded ion intensity value. This may be carried out exclusively against an ion signal at a specific mass to charge ratio, or alternatively against the total or average ion count for the entire spectrum.[7]

Currently, there is widespread disagreement as to which normalisation approach is the most appropriate. Arguments against normalising spectra intensities to a single peak signal relate to concerns that ion intensity changes associated with ion suppression are not taken into account. Just as an area of low matrix abundance may reduce an observed ion signal irrespective of the compound's abundance, normalising against an ion which is subject to a varying degree of suppression could lead to a similar effect. For this reason many researchers choose to normalise against total ion count.

The experiments described in this chapter aim to assess the benefits and disadvantages of single ion count (SIC) versus total ion count (TIC) normalisation. Statistical evaluation has been carried out to assess each method in the hope of providing some resolution to the uncertainty over normalisation procedures.

5.2 Materials and Methods

5.2.1 Materials

Sample spectra were acquired from two different image datasets, the first being a H460 human tumour xenographt. The tumour analysed was excised from a mouse previously treated with AQ4N. It was flash frozen immediately upon excision and stored at -80°C until required.

Tumour cryosections were produced at 12 μm thickness at an operating temperature of -20 °C. Sections were placed directly onto disposable aluminium sheets and coated in α-CHCA matrix (25 mg/mL in ethanol, 1.0% TFA) by air-spray depostition.

The second set of sample data was obtained from an indirect tissue image of hydrocortisone treated porcine skin tissue. The skin was treated over a defined 6mm circular area with a generic hydrocortisone formulation (0.1% w/w active ingredient) and incubated for 1 hour at 37°C. An imprint of the skin was made on a cellulose membrane using the solvent assisted blotting approach. An ethanol soaked membrane was air dried for 60 seconds. The membrane was then applied to the surface of the treated skin tissue under defined pressure for 90 seconds. The resulting tissue blot was coated in approximately 5 mL of α-CHCA in ethanol, 0.1% TFA in preparation for analysis.

Images were acquired at 200 μm increments using a laser power of 3.2 μJ with a laser ablation time of approximately 3 seconds at each position. A beta test version of the Applied Biosystems/MDS Sciex 'Dynamic Pixel' imaging mode was used during acquisition of the AQ4N tumour data to move the laser within the user-defined voxel dimensions at each point. This is employed in address to the sensitivity issue associated with using a Gaussian beam profile Nd:YaG laser.[8]

Sample spectra were taken from both sets of image data using Analyst QS 1.1 software (Applied Biosystems/MDS Sciex, Ontario, Canada).

AQ4N tumour data was obtained by selecting 10 sequential pixel spectra spanning across the width of the tissue slice. The 10 spectra were saved as text files and imported into the Markerview statistical analysis package (Applied Biosystems/MDS Sciex, Ontario, Canada) using import settings of 0.1 amu mass tolerance, 0.1 minimum ion intensity response and a maximum total of 2000 peaks.

The hydrocortisone blot data was obtained by randomly selecting 6 spectra from across the image sample. The 6 spectra were saved as text files and imported into the Markerview statistical analysis package using import settings of 0.1 amu mass tolerance, 0.1 minimum ion intensity response and a maximum total of 2000 peaks.

The purpose of using Markerview was two-fold. With the Markerview data import features it is possible to align spectra according to mass to charge ratio in a table format and to remove background noise (i.e. m/z values with an ion signal response <0.1) from the data. The maximum total number of peaks was set to 2000 to fit within the confines of data capacity and processing power of Microsoft Excel. The data table was exported from Markerview in text file format and further normalisation and statistical analysis was carried out using Microsoft Excel.

5.2.2 Methods

5.2.2.1 Single Ion Count Normalisation

Single ion count (SIC) normalisation was carried out using the ion counts for the protonated form of the α-CHCA matrix molecule (m/z 190). A group average spectrum was created by working out the average ion count for each m/z value across all sample spectra. The ratio between the average ion count at m/z 190 and individual spectra ion counts for m/z 190 was then calculated by dividing the average spectrum m/z 190 value by the individual sample spectra m/z 190 value. The ratio determined in relation to each spectrum was used as multiplying factor for all ion signal responses within its own spectrum.

5.2.2.2 *Total Ion Count Normalisation*

Total ion count (TIC) normalisation was carried out using the total ion count values for each spectrum. A group average spectrum was created by working out the average ion count for each m/z value across all sample spectra. The total ion count was calculated for each of the sample spectra as well as the group average spectrum. The ratios between the total ion count of the group average spectrum and the total ion count of the sample spectra were then calculated by dividing the average spectrum TIC by the individual sample spectra TIC. The ratio determined in relation to each spectrum was used as multiplying factor for all ion signal responses within its own spectrum.

5.2.2.3 *TIC Normalisation followed by SIC normalisation*

TIC normalisation was carried out as previously described. A new group average spectrum was calculated for the TIC normalised data and the TIC normalised spectra were then subject to the SIC normalisation procedure formerly described.

5.2.2.4 *SIC Normalisation followed by TIC normalisation*

SIC normalisation was carried out as previously described. A new group average spectrum was calculated for the SIC normalised data and the SIC normalised spectra were then subject to the TIC normalisation procedure formerly described.

5.2.2.5 *Ion Species Specific Normalisation*

A further method of normalization was evaluated for the hydrocortisone data which functions to normalize all ion species separately against the respective ion species of the matrix. In this method of normalization, referred to here as ion species specific (ISS) normalization, the ion intensities in each spectrum were normalised to the corresponding matrix species.

Ion species specific normalisation was carried out after assignment of ion species (i.e., protonated molecule, Na^+/K^+ adduct) to peaks in the image spectra. The assignment of ion species was carried out in Microsoft Excel by manually searching through m/z values and comparing the masses with predicted m/z values for possible adducts. This is explained in more detail in figure 5.1.

Where a group of related ion species could be defined, the relevant ion species were assigned. The ion intensities in each spectrum were normalised to the corresponding matrix species, i.e., peaks presumed to be non-alkali metal containing were normalised to the α-CHCA $[M+H]^+$ ion at *m/z* 190 and others to the $[M+Na]^+$ ion at *m/z* 212 or the $[M+K]^+$ ion at *m/z* 228 as appropriate.

Normalisation factors were calculated specifically for each ion species within each spectrum. For instance, normalization factors for [M+H]+ ion species were calculated by taking the average ion intensity for the protonated molecule of the matrix (m/z 190) and dividing it by the recorded ion intensity for the protonated molecule of the matrix in each spectrum. Each normalisation factor obtained was then used as a multiplier for all protonated molecule intensities within its own spectrum.

This was repeated in the same way for the sodium adducts, using the sodium adduct of the matrix (m/z 212) to calculate the normalization factors and again for the potassium adducts using the potassium adduct of the matrix (m/z 228) to calculate the normalization factors.

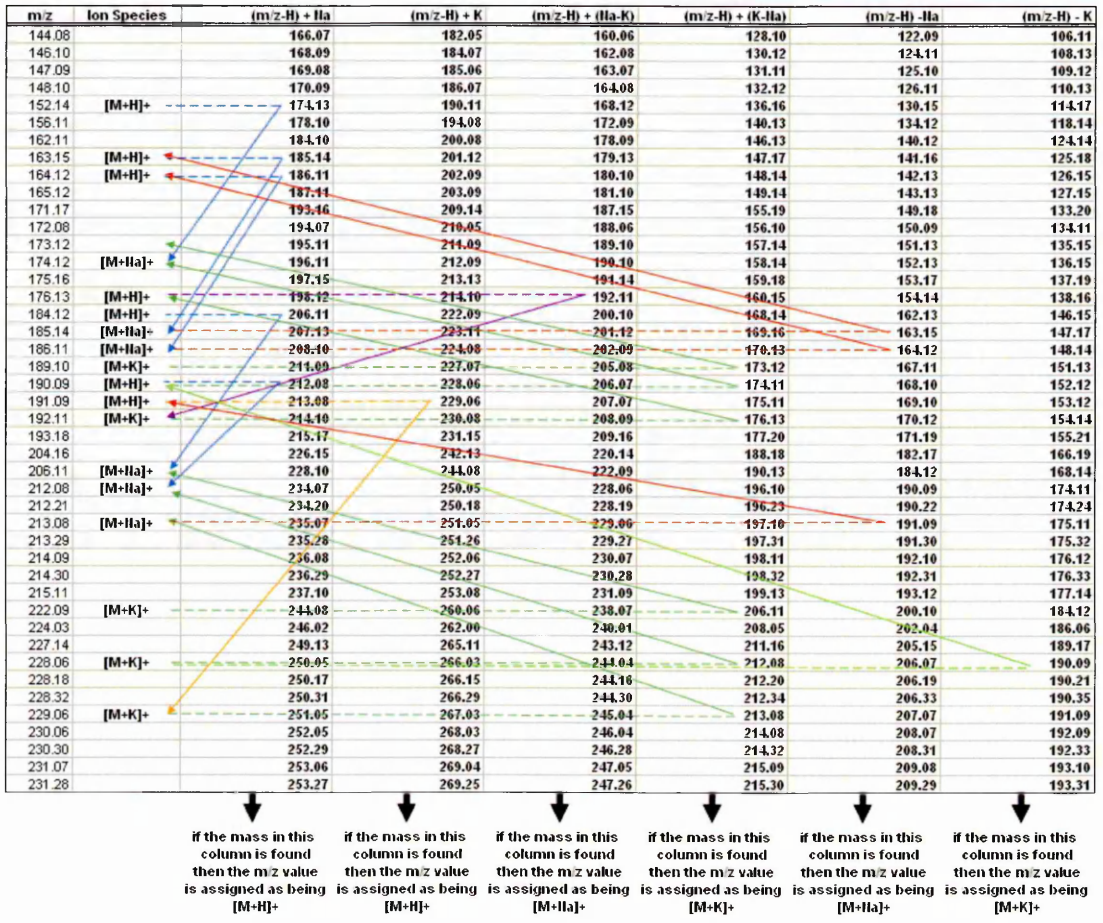

m/z	Ion Species	(m/z-H) + Na	(m/z-H) + K	(m/z-H) + (Na-K)	(m/z-H) + (K-Na)	(m/z-H) -Na	(m/z-H) - K
144.08		166.07	182.05	160.06	128.10	122.09	106.11
146.10		168.09	184.07	162.08	130.12	124.11	108.13
147.09		169.08	185.06	163.07	131.11	125.10	109.12
148.10		170.09	186.07	164.08	132.12	126.11	110.13
152.14	[M+H]+	174.13	190.11	168.12	136.16	130.15	114.17
156.11		178.10	194.08	172.09	140.13	134.12	118.14
162.11		184.10	200.08	178.09	146.13	140.12	124.14
163.15	[M+H]+	185.14	201.12	179.13	147.17	141.16	125.18
164.12	[M+H]+	186.11	202.09	180.10	148.14	142.13	126.15
165.12		187.11	203.09	181.10	149.14	143.13	127.15
171.17		193.16	209.14	187.15	155.19	149.18	133.20
172.08		194.07	210.05	188.06	156.10	150.09	134.11
173.12		195.11	211.09	189.10	157.14	151.13	135.15
174.12	[M+Na]+	196.11	212.09	190.10	158.14	152.13	136.15
175.16		197.15	213.13	191.14	159.18	153.17	137.19
176.13	[M+H]+	198.12	214.10	192.11	160.15	154.14	138.16
184.12	[M+H]+	206.11	222.09	200.10	168.14	162.13	146.15
185.14	[M+Na]+	207.13	223.11	201.12	169.16	163.15	147.17
186.11	[M+Na]+	208.10	224.08	202.09	170.13	164.12	148.14
189.10	[M+K]+	211.09	227.07	205.08	173.12	167.11	151.13
190.09	[M+H]+	212.08	228.06	206.07	174.11	168.10	152.12
191.09	[M+H]+	213.08	229.06	207.07	175.11	169.10	153.12
192.11	[M+K]+	214.10	230.08	208.09	176.13	170.12	154.14
193.18		215.17	231.15	209.16	177.20	171.19	155.21
204.16		226.15	242.13	220.14	188.18	182.17	166.19
206.11	[M+Na]+	228.10	244.08	222.09	190.13	184.12	168.14
212.08	[M+Na]+	234.07	250.05	228.06	196.10	190.09	174.11
212.21		234.20	250.18	228.19	196.23	190.22	174.24
213.08	[M+Na]+	235.07	251.05	229.06	197.10	191.09	175.11
213.29		235.28	251.26	229.27	197.31	191.30	175.32
214.09		236.08	252.06	230.07	198.11	192.10	176.12
214.30		236.29	252.27	230.28	198.32	192.31	176.33
215.11		237.10	253.08	231.09	199.13	193.12	177.14
222.09	[M+K]+	244.08	260.06	238.07	206.11	200.10	184.12
224.03		246.02	262.00	240.01	208.05	202.04	186.06
227.14		249.13	265.11	243.12	211.16	205.15	189.17
228.06	[M+K]+	250.05	266.03	244.04	212.08	206.07	190.09
228.18		250.17	266.15	244.16	212.20	206.19	190.21
228.32		250.31	266.29	244.30	212.34	206.33	190.35
229.06	[M+K]+	251.05	267.03	245.04	213.08	207.07	191.09
230.06		252.05	268.03	246.04	214.08	208.07	192.09
230.30		252.29	268.27	246.28	214.32	208.31	192.33
231.07		253.06	269.04	247.05	215.09	209.08	193.10
231.28		253.27	269.25	247.26	215.30	209.29	193.31

Figure 5.1 Determining Ion Species

The assignment of ion species was carried out by predicting m/z values of other adducts of the same molecule. Calculations used to predict m/z values were carried out using the mass differences calculated between the protonated molecule (m/z 190.09), sodium adduct (m/z 212.08) and potassium adduct (m/z 228.06) of α-CHCA in this spectrum.

5.2.2.6 *Statistical Evaluation of Normalisation Procedures*

Assessing Linearity of Normalised Data

One of the main objectives in normalising image data is to correct spectrum to spectrum ion intensity scale variation associated with matrix coverage and matrix crystalisation issues. The success of normalisation in reducing ion intensity scale variation has been assessed in this experiment by investigating the linear relationship between each sample spectrum and the group average spectrum.

A scatter plot of group average spectrum ion intensities (x) versus the sample spectrum ion intensities (y) was created for each sample spectrum. In displaying the ion intensities in a Cartesian plane in this way, a linear function equation ($y=mx+c$) can be applied in determining the overall gradient of the trend of points plotted between sample and group average spectra. In terms of applying this equation to the assessment of normalisation in this case, gradients approaching a value of 1 would show a low level of spectrum ion intensity scale variation comparable to the group average spectrum.

In calculating the gradient (m) in these calculations, the intercept (c) was uniformly set to a value of zero to ensure that the gradient of the line was unaffected by inequality in the scale of the axis for the two sets of spectrum intensities.

The gradient value was obtained for all samples prior to normalisation and after each of the different types of normalisation. The average gradient was then determined for each specific type of normalisation and the standard error of the mean calculated for each data set of gradient values.

Assessing Correlation of Spectra after Normalisation

Determination of the gradient of points in a Cartesian plane can be used to indicate the overall linear trend of x,y values. It does not, however, provide indication as to the strength of the linear relationship between each sample and the group average spectrum (i.e. how closely the points on the scatter plot fall to the line). In terms of fully assessing the linear relationship between spectra the Pearson product-moment correlation (r) has been employed. The formula of r is shown in equation 5.1.

$$r = \frac{\sum ZxZy}{n-1}$$

Equation 5.1 The Pearson Product-moment Correlation Coefficient.

The Pearson product-moment correlation coefficient is defined as the sum of the products of the standard scores of the two measures divided by the degrees of freedom. The Z score is determined through subtraction of the population mean from an individual score followed by division of the difference by a measure of the spread of the values. In this equation standard deviation is used as a measure of the spread of values.

The Pearson product-moment correlation coefficient can be used as a measure of the correlation between two variables (x and y). It indicates the tendency of the variables to increase or decrease together. The coefficient may range from a value of -1.0 to 1.0, with a score of 1.0 indicating a perfect and positive linear relationship.

A score of zero indicates that variables are completely unrelated and a score of -1.0 indicates a perfect negative linear relationship. [9] The r^2 value can also be determined to provide the fraction of variability in y that can be explained by the variability in x by their linear relationship. This equation has not been applied to this data as it results in a loss in the negative aspect of the Pearson formula.

A perfect positive linear relationship would imply that all points of the scatter plot fall on a straight line. This would rarely be the case when comparing multivariate data such as spectra. However, the more points that tend to fall along a straight line the stronger the linear relationship would be.

In this experiment the Pearson product-moment correlation has been used to determine the strength of the linear relationship between each sample spectrum and the group average spectrum. This has been applied to untreated data as well as to data after each different type of normalisation. The average PMCC value was then determined for each specific type of normalisation and the standard error of the mean calculated for each data set of PMCC values.

Assessing Variation in Adduct Processes after Normalisation

The effect of different types of normalisation have been assessed as to whether each may carry benefits toward the issue of resolving variation in adduct processes in image data.

In assessing the relationship between adduct form intensities the coefficient of determination r^2 has been employed. Clearly, if in theory adduct form ratios ought to remain stable in the absence of salt interference, a global fit between the adduct form ion intensities pattern across spectra should be observed (i.e. an increase in the protonated form should be reflected by an increase in both the sodium and potassium adduct forms).

The r^2 equation builds on Pearson's correlation coefficient and therefore is also determinate of the correlation of the variance of y with changes in x and the linear relationship between x and y. The r^2 equation is used in interpretation of the Pearson's correlation coefficient to define the fraction of variability in y that can be explained by changes in x and their linear relationship.[9] The scale of the r^2 coefficient ranges from zero to 1.0, where a coefficient of 0.90 indicates that approximately 90% of variance in the y variable can be explained by, but is not dependant upon, the x variable. As such, this equation is conventionally used to provide a measure of the association between x and y. The formula for r^2 is shown in equation 5.2.

$$r^2 = \frac{S_{y'}^2}{S_y^2}$$

Equation 5.2 The Coefficient of Determination r^2

For each value (x) from within the dataset, the equation calculates estimated values for y in relation to the specific related values of x, thus the total variability of y from the predicted values can be calculated and divided by the sum variability of y about its mean.

The phosphatidylcholine head group has been used as a model compound to assess variation in adduct processes before and after each method of normalisation. Phospholipids are abundant in many biological tissues and as such form ideal candidates for assessing the normalisation of adduct processes in the tumour image data. For each of the data sets (untreated and normalised), r^2 values were calculated using the ion intensities across all 10 spectra for the sodium adduct of the phosphatidylcholine head group (y) at m/z 206 and the ion intensities for the protonated molecule (x) at m/z 184. This was repeated in the same way using the ion intensities for the potassium adduct of the phophotidylcholine head group (y) at m/z 222.

5.3 Results

5.3.1 Normalisation of AQ4N Tumour Image Data

5.3.1.1 Assessing Linearity of Normalised Data

In assessing the intensity scale variation between AQ4N tumour image spectra, the gradients of the straight line plots generated from x,y scatterplots of ion intensity measurements for single spectra plotted against the group average spectrum have been calculated. Representative data from a single selected spectrum before and after each different method of normalisation is shown in figure 5.2. From these data it would appear that SIC normalisation provides the greatest level of success in normalising ion intensity scale variation between spectra as both SIC and TIC-SIC normalisation of this spectrum provides the gradient value closest to 1.0 (i.e.1.04). However, on examination of the average gradients and standard deviation of full data sets, it is found that this may not be the case.

Figure 5.3 shows a graphical representation of the average gradients of the 10 spectra, both before and after each type of normalisation. In these results it can be seen that although the average gradient does not change, the reproducibility (defined by the standard deviation) within data sets does alter significantly. The level of reproducibility appears to relate directly to the final normalisation step employed.

The gradient values for SIC and TIC-SIC normalisation are found to have a standard deviation of 0.45, whereas TIC and SIC-TIC normalisation have a standard deviation of 0.15. The raw data carries a standard deviation of 0.16, therefore only normalisation procedures concluding in TIC normalisation appear to reduce ion intensity scale variation between spectra. It should be noted here that this observed improvement is quite small and the overall benefit of TIC normalisation remains inconclusive in the absence of further evaluation of the data. Furthermore, it appears from these results that the inclusion of SIC normalisation alters the overall scale of ion intensities from between zero and ~1400 to between zero and ~2000. This implication of this effect is further evaluated in later sections of this chapter.

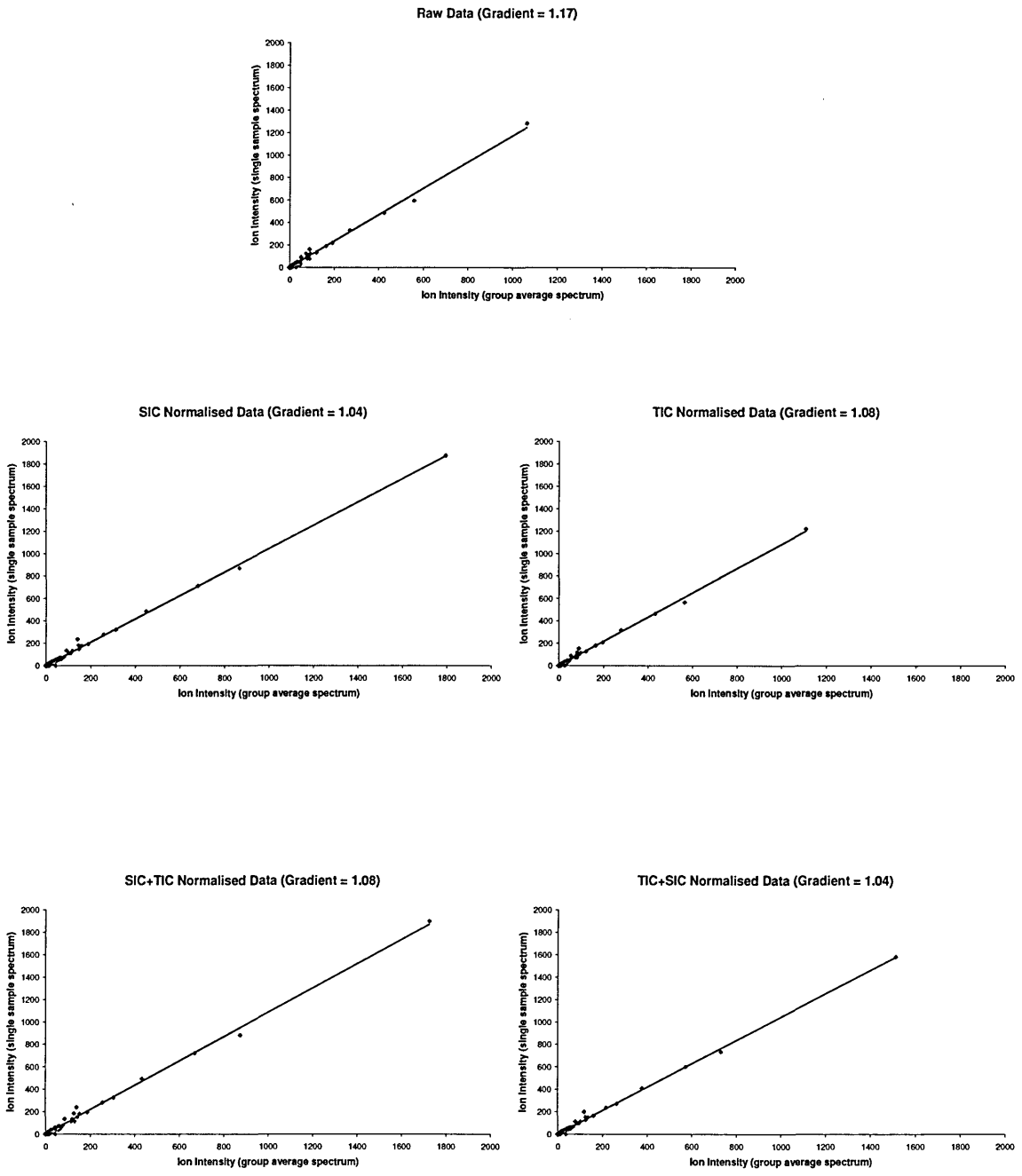

Figure 5.2 Representative x,y Scatter plots for the Assessment of the Linearity of Normalised AQ4N Tumour Data

Plots are shown of the ion intensity values of the group average spectrum versus the ion intensity values for a single sample spectrum before and after each type of normalisation. SIC normalisation appears to have the greatest influence in increasing the degree of linearity between spectra.

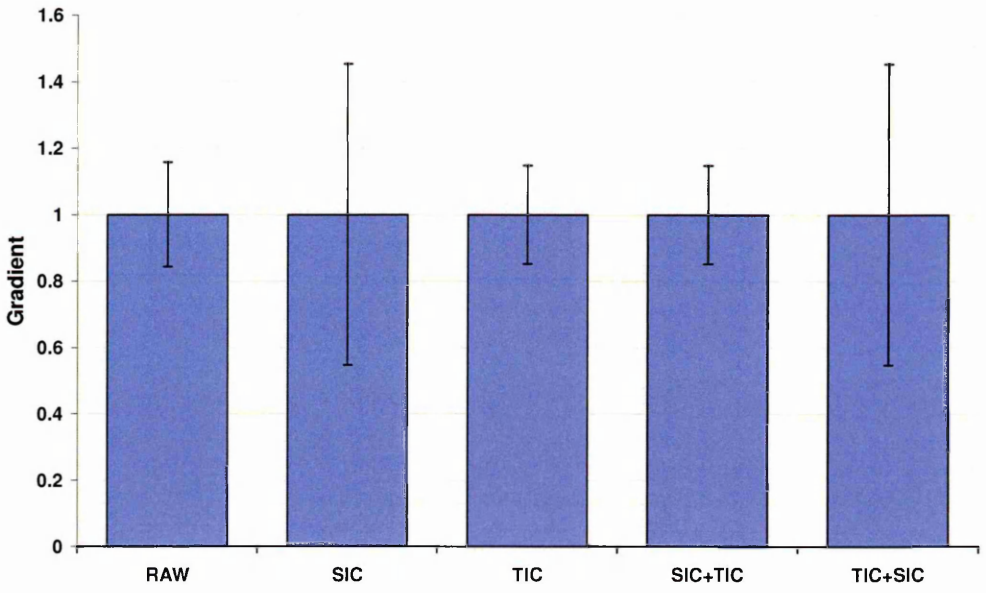

Figure 5.3 Average Gradients of AQ4N Tumour Spectra before and after Normalisation

The average gradient values determined for the sets of spectra before and after normalisation are shown with error bars displayed as the standard deviation (SD) for each data set. All data sets provide an average gradient of 1.0, however, the degree of error within each dataset varies (Raw SD = 0.16; SIC SD = 0.45; TIC SD = 0.15; SIC-TIC SD = 0.15; TIC-SIC SD = 0.45).

5.3.1.2 *Assessing Correlation of Spectra after Normalisation*

In determining the most appropriate form of normalisation the Pearson's product-moment correlation coefficient has been used to assess the effects of normalisation on the correlation of spectra. It is important that in normalising data, the relationship between spectral patterns is not significantly altered. Reduction in the correlation of spectral patterns would indicate distortion of spectra during the normalisation process, a possibility which may prove to complicate image interpretation further still.

The results of the PMCC evaluation are shown in figure 5.4. From the values obtained it can be seen that the PMCC for each type of normalisation is comparable to that of the raw data and that the degree of error (defined as the standard deviation) within groups remains small. This would indicate that negligible change in the correlation of spectra is induced through normalisation. This is further evaluated in assessing the effect of normalisation on variation of adduct processes.

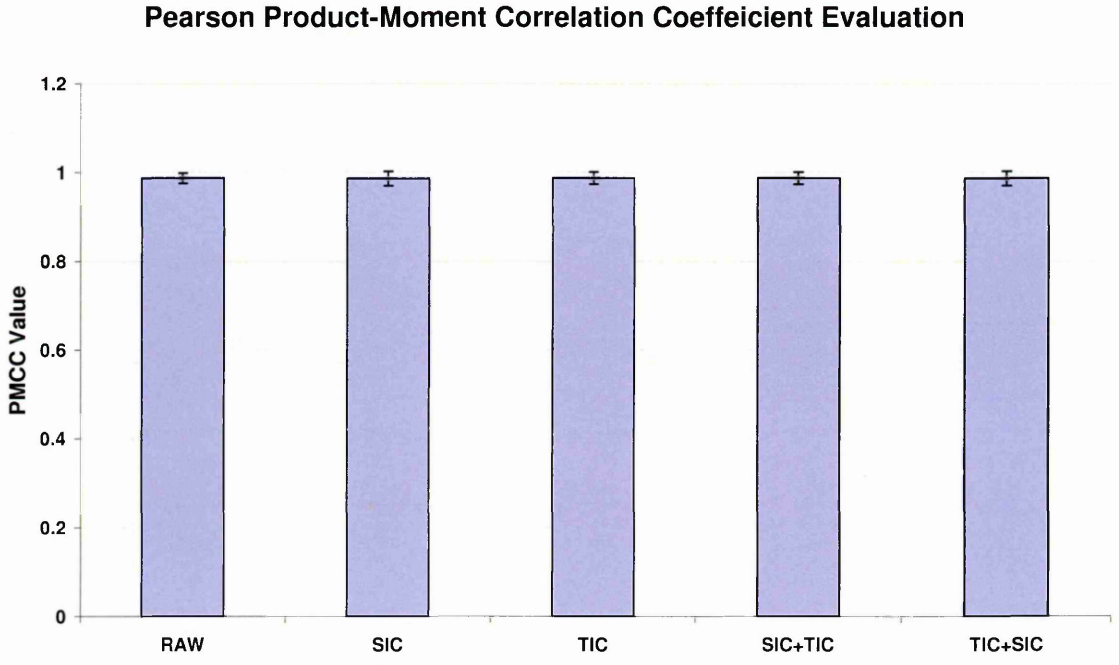

Figure 5.4 Pearson Product-Moment Correlation Coefficient Evaulation of AQ4N Tumour Data

The average PMCC values are displayed with error bars shown as the standard deviation for each dataset. The PMCC values determined for each of the datasets as well as the degrees of error are highly comparable with the results given for raw data. This would indicate that for each type of normalisation, negligible change to the correlation of spectra is induced.

5.3.1.3 *Assessing Adduct Relationships after Normalisation*

Variation in adduct ion relative intensities has been assessed using ions arising from the phosphatidylcholine head group as a model ($[M+H]^+$ at m/z 184, $[M+Na]^+$ at m/z 206 and $[M+K]^+$ at m/z 222). Figure 5.5 shows the r^2 values obtained for both the sodium and potassium adduct intensities across the 10 spectra in relation to the observed intensities for the protonated molecule.

High correlation is found with raw data as would be expected in the absence of severe salt variations. In normalising the data it would be hoped that this level of correlation would be maintained. It has been found, however that with both TIC and SIC-TIC normalisation a drastic reduction in the correlation between adduct ion intensities with the protonated molecule intensities is induced. Whilst it appears in this figure that the correlation is maintained in SIC and TIC-SIC normalisation, further assessment of the effects of normalisation may generate cause for concern. Figure 5.6 further assesses the effect of normalisation on the pattern of observed intensities.

In Figure 5.6 it can be seen in raw data that whilst the ion intensities of the various adduct forms of phosphatidylcholine correlate with one another, they also correlate with the average ion count and the ion intensities of the protonated molecule of the matrix. This indicates the degree of dependence of the total ion count (represented here as an average) on the presence of matrix. It also shows a correlation between ion intensity variation for phosphatidylcholine throughout the spectra in accordance with the amount of matrix present. This is a prime example to illustrate the necessity for normalisation.

Normalisation should in theory reduce the correlation between analyte signals and total ion and/or matrix ion counts. In this sense, observed ion intensity changes associated with analyte signals may be attributed to actual analyte abundance as opposed to the presence of matrix crystals and the efficiency of ionisation.

After SIC normalisation, phosphatidylcholine signals remain relative to the average ion count, yet their relationship to the matrix signal is reduced. The correlation between phosphatidylcholine adduct forms remains strong (with r^2 values of >0.6), but variation in average ion intensity (i.e. ion intensity scale) measurements has increased (from between ~500-1200 in raw data to between ~300-1900 in SIC normalised data).

After TIC normalisation there is a loss in the relationship between phosphatidylcholine signals and the average ion count, as well as the matrix response. This is coupled by a loss in correlation between the ion intensities for the various phosphatidylcholine adduct forms across the spectra.

The results of two stage normalisations appear to be largely defined by the final stage of normalisation. SIC-TIC normalisation provides a similar scenario to that found with TIC normalisation, but the average ion count is increased from ~700 to ~1100. TIC-SIC normalisation generates similar results to those found with SIC normalisation, but the average ion count variation is reduced from ~300-1900 to ~300-1700.

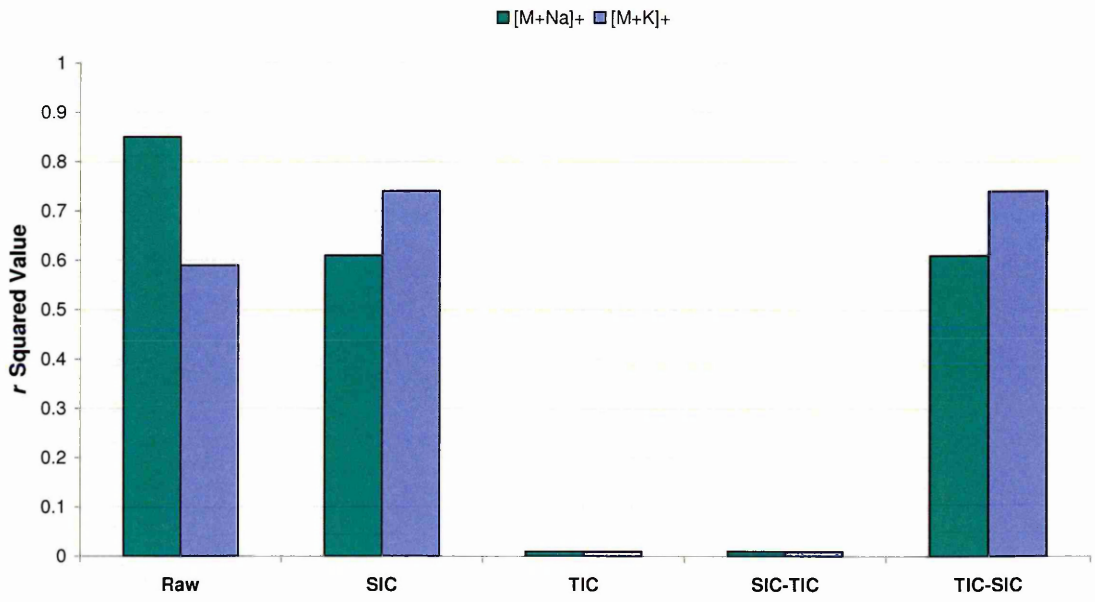

Figure 5.5 Assessing the Relationship Between Adduct Processes in AQ4N Tumour Data

The r^2 value for both the sodium adduct [M+Na]+ and potassium adduct [M+K]+ ion intensity patterns of the phosphatidylcholine head group in relation to the observed ion intensity pattern of the protonated molecule are shown. Both SIC and TIC-SIC normalisation show comparable levels of correlation of variance with the intensities recorded for the protonated molecule. The low r^2 values for TIC and SIC-TIC normalisation indicate that there is little correlation between the intensities recorded for the various adduct forms after these types of normalisation.

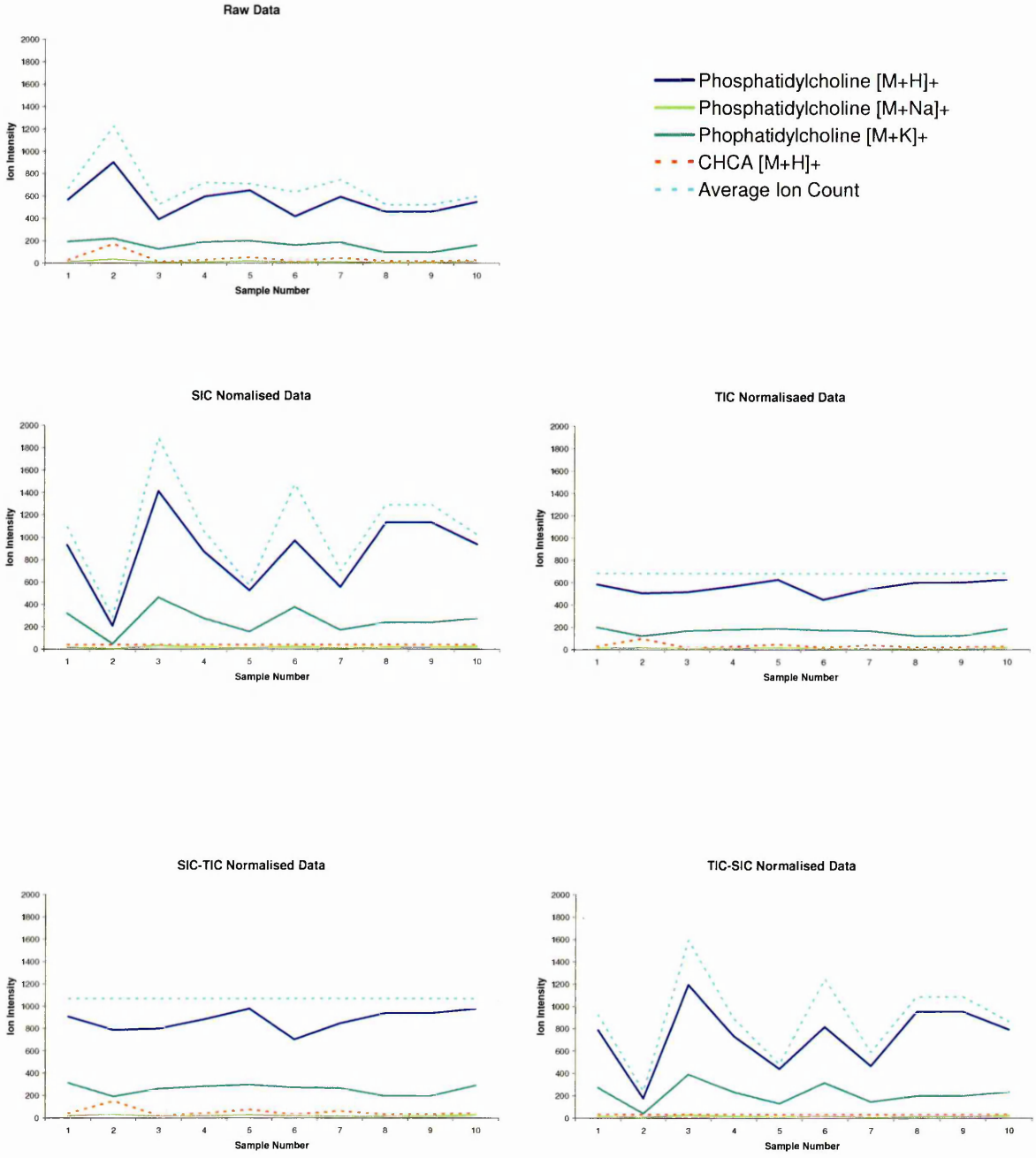

Figure 5.6 Assessing Ion Intensity Patterns for Phosphatidylcholine Adducts in AQ4N Tumour Data

The ion intensities across all 10 sample spectra are shown before and after each type of normalisation for phosphatidylcholine [M+H]+, [M+Na]+ and [M+K]+, α-CHCA [M+H]+ as well as the average ion count. It is shown that TIC normalisation significantly alters the general pattern of ion intensities and the relationships between [M+H]+, [M+Na]+ and [M+K]+ ion intensity patterns specifically.

5.3.2 Normalisation of Hydrocortisone Treated Skin Image Data

5.3.2.1 Assessing Linearity of Normalised Data

To assess the intensity scale variation between hydrocortisone treated skin image spectra, the gradients of the straight line plots generated from x,y scatterplots of ion intensity measurements for single spectra plotted against the group average spectrum have been calculated. A representation of the results for a single selected spectrum before and after each different method of normalisation is shown in figure 5.7. From these data it appears that ISS normalisation provides the greatest level of success with regards to normalising ion intensity scale variation between spectra. Closer examination of the full data sets further supports this.

Figure 5.8 shows a graphical representation of the average gradients of the 6 spectra, both before and after each type of normalisation. The results obtained for SIC and TIC normalised data are similar to those presented from the normalisation of the AQ4N tumour data in section 5.3.1.1 of this chapter. In the figures presented here it can be seen that although the average gradient does not change, the degree of error within data sets (defined as the standard deviation) does alter in accordance with the normalisation procedure employed.

As with the AQ4N tumour data, SIC normalisation is found to increase the degree of error from a standard deviation of 0.035 in raw data to 0.299 in SIC normalised data. Similarly again to the AQ4N data, TIC normalisation is shown to slightly decrease the degree of error to a standard deviation of 0.018. ISS normalisation, however, is found to reduce the degree of error further to a standard deviation of 0.006.

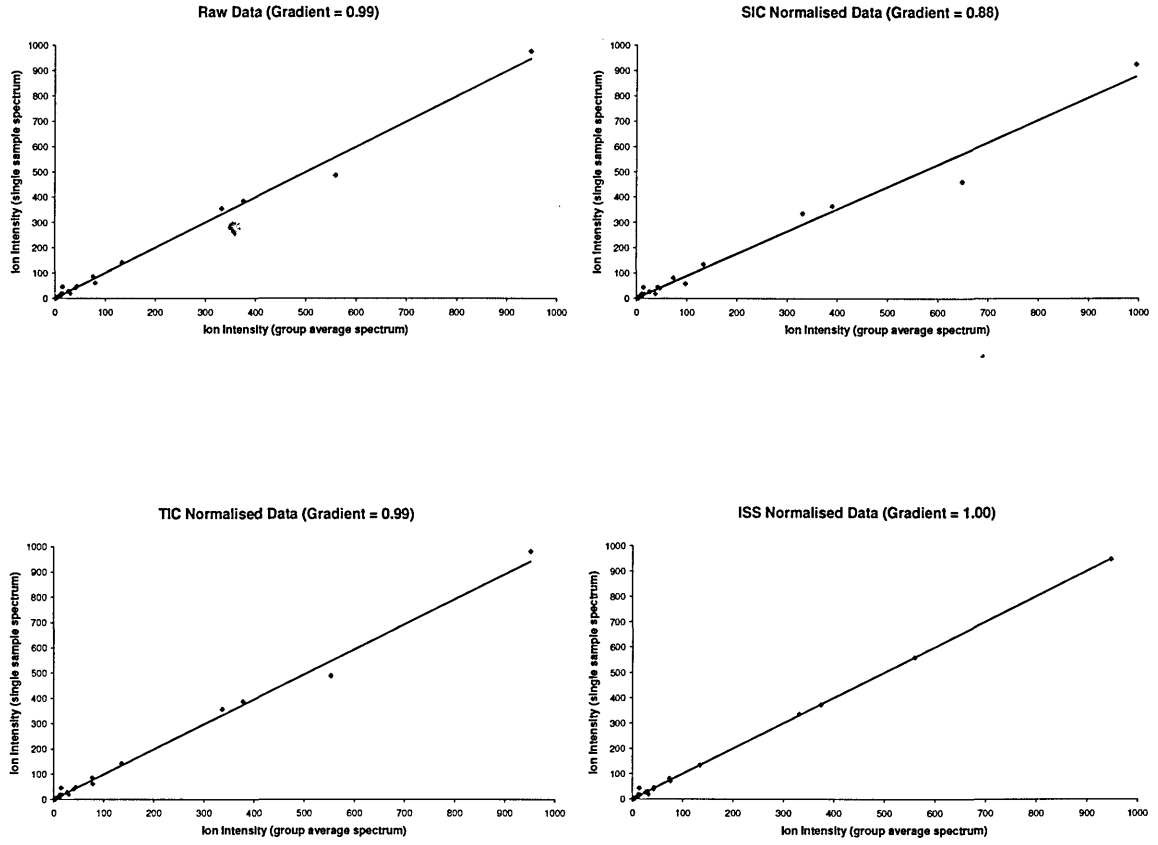

Figure 5.7 Representative x,y Scatter plots for the Determination of Linearity of Hydrocortisone Treated Skin Data

Plots are shown of the ion intensity values of the group average spectrum versus the ion intensity values for a single sample spectrum before and after each type of normalisation. ISS normalisation shows the greatest increase in linearity between spectra.

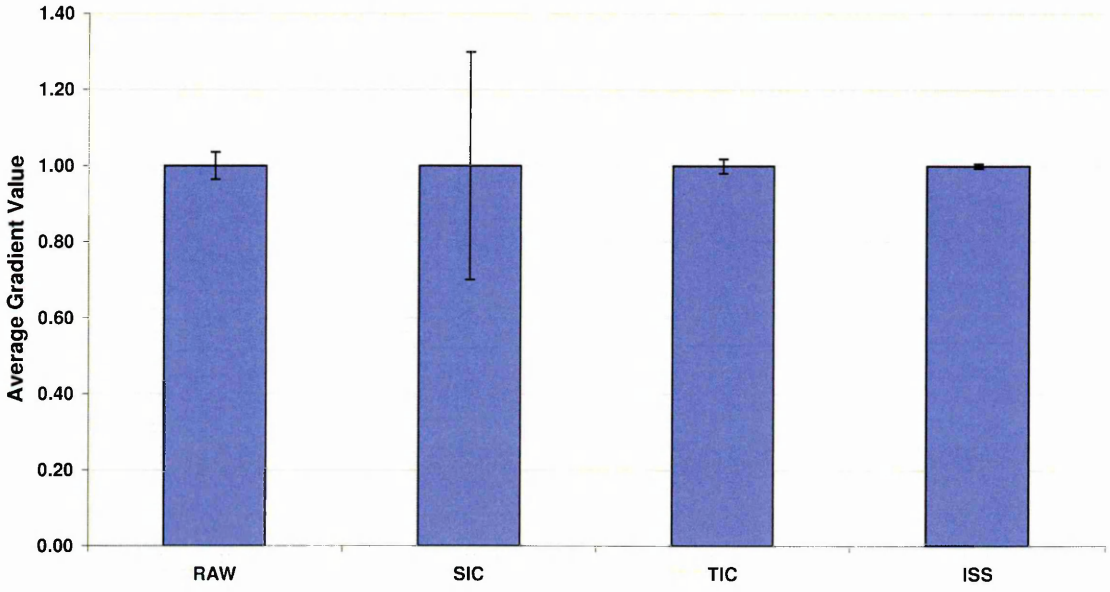

Figure 5.8 Average Gradients of Hydrocortisone Treated Skin Spectra before and after Normalisation

The average gradient values determined for the sets of spectra before and after normalisation are shown with error bars displayed as the standard deviation (SD) for each data set. All data sets provide an average gradient of 1.0, however, the degree of error within each dataset varies (Raw SD = 0.035; SIC SD = 0.299; TIC SD = 0.019; ISS SD = 0.006).

5.3.2.2 *Assessing Correlation of Spectra after Normalisation*

In assessing the effects of normalisation on the correlation of spectra, the Pearson product-moment correlation coefficient has been applied to untreated and normalised hydrocortisone data. Again this equation has been used as opposed to r^2 to prevent loss of the negative aspect of the equation.

The results of the PMCC evaluation are shown in figure 5.9. After SIC and TIC normalisation it can be seen that the correlation of spectra remains comparable to that of the raw data. ISS normalisation is found to enhance the degree of spectral correlation from a PMCC value of 0.982 (in raw data) to 0.999 in the ISS normalised data. Furthermore, it is shown that although the PMCC for each type of normalisation is not found to be reduced in comparison to that of the raw data, the degree of error within groups (defined as the standard deviation) alters in accordance with the type of normalisation employed.

As with the AQ4N tumour data, the reproducibility within groups does not alter significantly between raw, SIC and TIC normalised data, with standard deviations of 15.3×10^{-3}, 8.8×10^{-3} and 14.1×10^{-3} being recorded respectively. With ISS normalisation, however, there is a noted decrease in the standard deviation to a value of 0.7×10^{-3}. This would indicate that ISS normalisation provides more than a 10 fold increase in the reproducibility of ion intensity scale in correlation of spectra when compared to either of the other normalisation techniques.

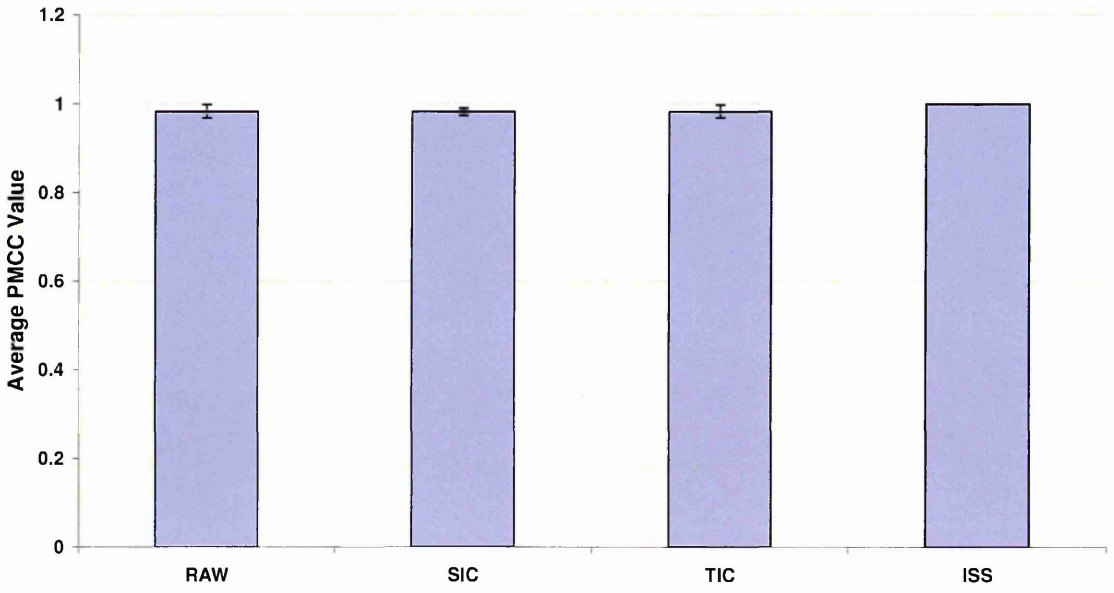

Figure 5.9 Pearson Product-Moment Correlation Coefficient Evaluation of Hydrocortisone Treated Skin Data

The average PMCC values are displayed with error bars shown as the standard deviation for each dataset. The PMCC values determined for SIC and TIC normalisation as well as the degrees of error are highly comparable to the results given for raw data. The PMCC value for ISS normalisation is visibly higher than that of the raw data and either of the other normalised datasets and the degree of error is also significantly lower.

5.3.2.3 *Assessing Adduct Relationships after Normalisation*

For the sake of consistency, the distortion of adduct ion relative intensities in hydrocortisone treated skin data has been assessed in the same way as with the AQ4N treated tumour data in section 5.3.1.3 of this chapter, using the phosphatidylcholine head group associated ions as a model. Figure 5.10 shows the r^2 values obtained for both the sodium and potassium adduct intensities across the 6 spectra in relation to the observed intensities for the protonated molecule.

High correlation between adduct forms is found with raw data as would be expected in the absence of severe salt variations. As with the AQ4N data, TIC normalisation results in a loss in correlation between the adduct forms. However, in contrast to the AQ4N data normalisation, the SIC normalisation applied in this experiment is found to enhance correlation between the adduct forms.

The results obtained for ISS normalisation are of particular interest, not only is the correlation between adduct forms shown to be increased overall, but from the r^2 values obtained it now appears that the sodium and potassium adduct form intensities are equally related to the protonated molecule intensities.

This is illustrated further in figure 5.11. It can be seen that with ISS normalisation, both the sodium and adduct forms display matched intensities. Furthermore, whilst SIC and TIC normalisations produce constant intensities throughout the spectra for either the protonated molecule of the matrix or the average ion count respectively, ISS normalisation manages to combine constant intensities for both.

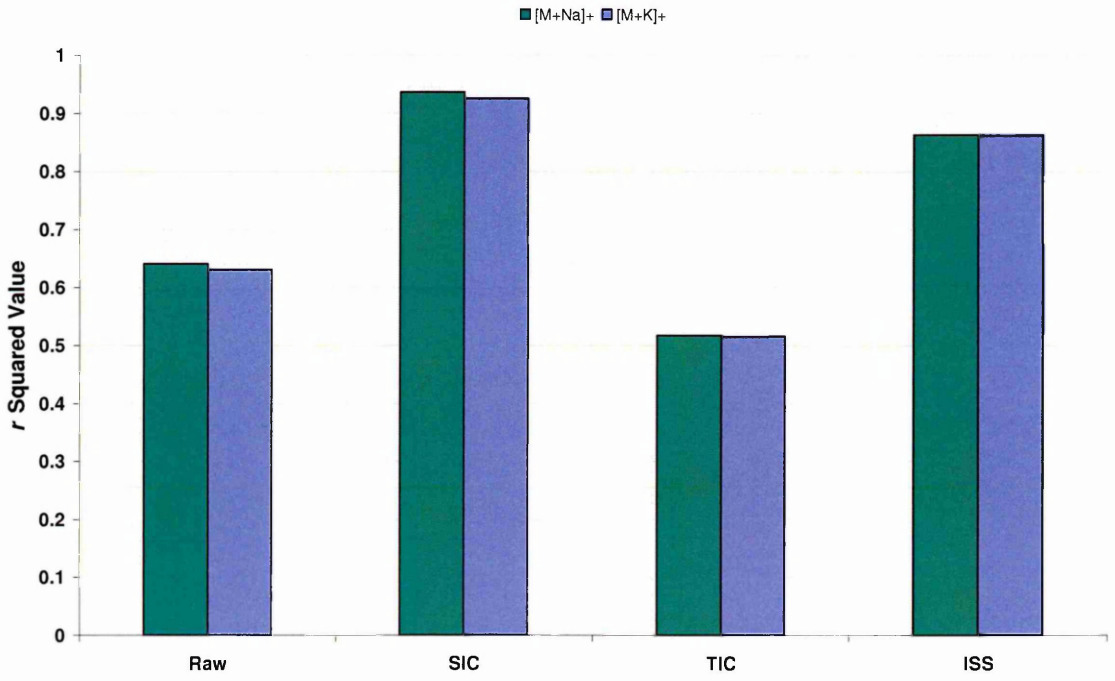

Figure 5.10 Assessing the Relationship Between Adduct Processes in Hydrocortisone Treated Skin Data

The r^2 value for both the sodium adduct [M+Na]+ and potassium adduct [M+K]+ ion intensity patterns of the phosphatidylcholine head group in relation to the observed ion intensity pattern of the protonated molecule are shown. Both SIC and ISS normalisation show increased levels of correlation of variance with the intensities recorded for the protonated molecule. ISS normalisation shows complete correlation of [M+Na]+ and [M+K]+ ion intensity patterns throughout spectra. The low r^2 value for TIC normalisation indicates that there is little correlation between the intensities recorded for the various adduct forms after this type of normalisation.

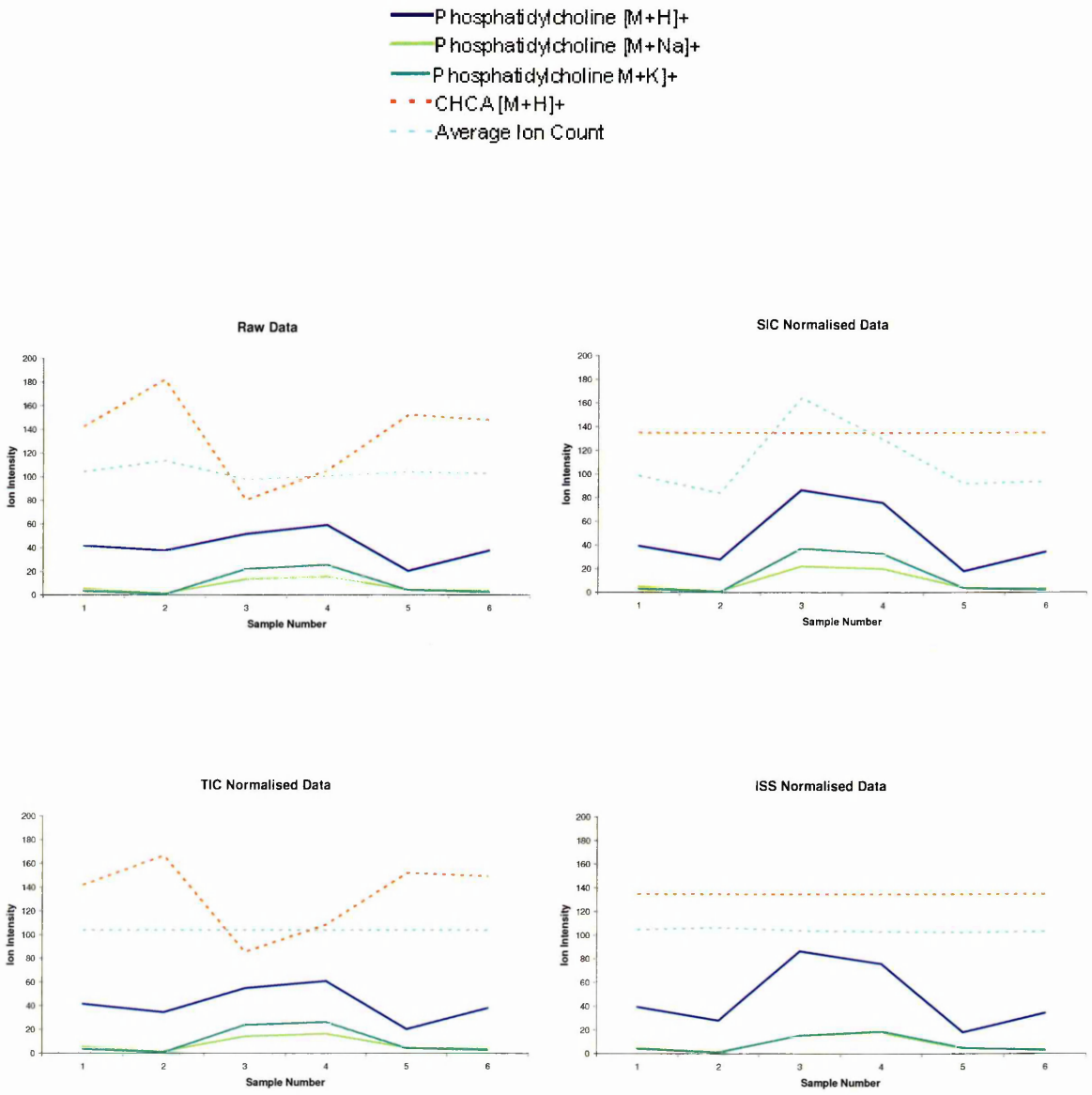

Figure 5.11 Assessing Ion Intensity Patterns for Phosphatidylcholine Adducts in Hydrocortisone Treated Skin Data

The ion intensities across all 10 sample spectra are shown before and after each type of normalisation for phosphatidylcholine [M+H]+, [M+Na]+ and [M+K]+, α-CHCA [M+H]+ as well as the average ion count. ISS normalisation is shown to reduce variation in spectral patterns associated with matrix coverage and total ion counts.

5.4 Conclusion

In the data presented in this chapter, it has been shown that ISS normalisation holds great potential as a method of increasing the reproducibility of ion intensity scale between image spectra. Furthermore, in assessing distortion of alkali metal adduct ion relative intensities, ISS normalisation is found to be more suitable than the other types of normalisation evaluated.

Whilst neither SIC nor TIC normalisation (either used singularly or in combination) appear to deteriorate the degree of correlation between sample spectra and the relative group average spectrum, it is found that with SIC normalisation the reproducibility of ion scale intensity between spectra is considerably reduced. In contrast, where SIC normalisation appears to reduce the distortion of alkali metal adduct ion relative intensities, TIC normalisation appears to increase the distortion effect.

In conclusion, from the data presented here, it may be assumed that ISS normalisation is the most appropriate method for reducing spectrum to spectrum ion intensity scale changes and distortion of adduct ion relative intensities simultaneously. In terms of MALDI-MS image analysis, this would dictate that normalisation of ion images against the respective matrix ion species is a valid means of data manipulation to be adopted in the reduction of both ion intensity scale variation and alkali adduct ion relative intensity distortion.

5.5 References

1. MORTIER, K.A., ZHANG, G., VAN PETEGHEM, CARLOS H. and LAMBERT, W.E., 2004. Adduct formation in quantitative bioanalysis: effect of ionization conditions on paclitaxel. *Journal of the American Society for Mass Spectrometry,* **15**(4), pp. 585-592.

2. SCHUERENBERG, M., LUEBBERT, C., DEININGER, S., KETTERLINUS, R. and SUCKAU, D., 2007. MALDI tissue imaging: mass spectrometric localization of biomarkers in tissue slices. *Nature Methods,* **4**, pp 3-5.

3. HANS-RUDOLF AERNI, R.M., CORNETT, D.S. and CAPRIOLI, R.M., 2006. Automated acoustic matrix deposition for MALDI sample preparation. *Analytical Chemistry,* **78**(3), pp. 827-834.

4. SHIMADZU BIOTECH. Chemical Inkjet Printing, CHIP-1000. Last updated 2007. Available: http://www.shimadzu-biotech.net/pages/products/2/chip.php. Last accessed September 7th 2007.

5. SUGIURA, Y., SHIMMA, S. and SETOU, M., 2006. Two-step matrix application technique to improve ionization efficiency for matrix-assisted laser desorption/ionization in imaging mass spectrometry. *Analytical Chemistry,* **78**(24), pp. 8227-8235.

6. ALTELAAR, A.F.M., TABAN, I.M., MCDONNELL, L.A., VERHAERT, P.D.E.M., DE LANGE, R.P.J., ADAN, R.A.H., MOOI, W.J., HEEREN, R.M.A. and PIERSMA, S.R., 2007. High-resolution MALDI imaging mass spectrometry allows localization of peptide distributions at cellular length scales in pituitary tissue sections. *International Journal of Mass Spectrometry,* **260**(2-3), pp. 203-211.

7. NORRIS, J.L., CORNETT, D.S., MOBLEY, J.A., ANDERSSON, M., SEELEY, E.H., CHAURAND, P. and CAPRIOLI, R.M., 2007. Processing MALDI mass spectra to improve mass spectral direct tissue analysis. *International Journal of Mass Spectrometry,* **260**(2), pp. 212-221.

8. HOLLE, A., HAASE, A., KAYSER, M. and HÖHNDORF, J., 2006. Optimizing UV laser focus profiles for improved MALDI performance. *Journal of Mass Spectrometry,* **41**(6), pp. 705-716.

9. ZOU, K.H., TUNCALI, K. and SILVERMAN, S.G., 2003. Correlation and simple linear regression. *Radiology,* **227,** pp 618-622.

CHAPTER 6

Multivariate Analysis in MALDI-MS Imaging

6 Multivariate Analysis in MALDI-MS Imaging

6.1 Introduction

Manual interpretation of scientific data can be extremely laborious and time-consuming. With datasets containing large numbers of discrete variables the task becomes more challenging still. In a study carried out on several thousand samples where each of those samples contains thousands of distinct variables, it is unrealistic to imagine that any useful information might be gained by attempting to correlate such data by hand.

A MALDI-MS image file may contain upward of 1000 sample spectra and (depending on the mass range of the experiment) each sample spectrum may contain literally thousands of ion signals. The recorded intensity for each of these signals may vary from one spectrum to the next, either dependently or independently from other ion signals within the spectra. In a blind study it would be unfeasible to assume that any correlation of ion signal variance could be determined by simply sifting through the image spectra manually. Less likely still is the possibility of defining a specific ion as accounting for a tangible degree of variance between discrete groups of sample spectra from within the image.

The data produced in MALDI-MS imaging may contain vast amounts of valuable information. Aside from the target analytes of the experiment, there may be any number of other hidden variables that could also prove pivotal to the research. Currently, most MALDI-MS imaging experiments are directed toward determining distributions of known analytes. The remaining data that are acquired is often disregarded.

In terms of fully utilising the wealth of information provided by MALDI-MS image analysis, a method is required which will allow the user to determine ions of interest from within these large multidimensional datasets. As these ions of interest are likely to be associated with variance in spectral patterns, statistical approaches may be adopted to mathematically sort through the data.

Some statistical approaches have already been tested in their application for assisting MALDI-MS image data evaluation. These primarily include principal components analysis (PCA) and hierarchical cluster analysis (CLA) methods. To date methods have been used to classify image pixels by spectral similarity, largely for the purpose of enhancing image quality and for defining spectral patterns associated with various tissue types.[1]

In this form of statistical approach, it is the spectral patterns rather than specific ions that are proven to be associated with defined image pixels. By no means may any of the ions assigned in a spectral pattern be regarded as being definitive of a particular tissue type.

As yet there are few reports of these statistical approaches being applied in a more refined manner, for example, for the direct determination of latent variables as tissue specific ions or ions which are present at elevated abundance in a certain tissue type. A method which could singularly pinpoint ions accounting for variance within an image would reduce the workload for analysts considerably.

Principal components analysis has been applied for the evaluation of MS data in a range of different studies. It has been used in the classification of edible oils based on their triacylglycerol composition determined by fast atom bombardment FAB-MS[2] as well as for the investigation of gasoline adulteration by gas chromatography GC-MS.[3] In more detailed biological studies developed to determine biomarkers using liquid chromatography (LC) MS, PCA has been shown to be a useful tool for discriminating between serum samples of variable protein concentration.[4]

In this chapter the use of PCA is investigated for its ability to define ions of interest from within MALDI-MS image datasets. Whereas previously this statistical approach has been applied to MALDI-MS image data solely for data reduction purposes (as a preliminary step toward further statistical evaluation), it is intended here that its use alone may provide the ability to pinpoint ions that may be confined to (or present elevated abundance in) defined regions within an image.

PCA is conventionally used as a means of reducing multidimensional data into lower dimensions of space, as such it is a useful technique for finding patterns in data of high dimensionality.[5] The end result is that highly complex data can be presented in a format that is more amenable to examination by the analyst. With the correct experimental ethos and view towards interpretation, PCA may provide greater insight as to which ions may be specific to certain tissue types or defined tissue regions within an image.

PCA is achieved through orthogonal linear transformation, where computation of the eigenvalue decomposition of a dataset allows transformation of the data onto a new coordinate system in relation to variance. Rather than having to assess ion intensity variability by comparing spectrum to spectrum differences one by one, the variables are themselves sorted into those presenting the greatest amount of influence in spectral variance between samples. The samples as well as the variables are aligned into graphical representations which can be interpreted to show which variables relate best to which samples.

The first coordinate (or the first principal component) is determinate of the greatest variance by any projection of the data. With mass spectrometry data this relates to ions accounting for the greatest variance between all spectra. The second coordinate (the second principal component) would be determinate of the second greatest variance, and so on, until negligible variance can be applied.

Each variable (in this case an *m/z* value and its associated ion intensity) is given a loading in respect to its own influence in each principal component assignment. These loadings are presented on the relevant principal component axis. Variables may then be displayed in a Cartesian plane between two principal component axis, where the *x* and *y* values for any given variable are provided by the computed loading of that variable with respect to each principal component axis selected.

In order to relate this information back to the original samples, a second plot of the scores for each sample (in this case each spectrum) can be displayed. The score values assigned to each sample indicate the weighting that a selected principal component carries within that sample. For example, samples presenting a positive PC1 score are likely to carry high ion intensity signals for ions with positive PC1 loading; samples presenting a negative PC1 score are, by comparison, likely to carry low ion intensity signals for ions with positive PC1 loadings. Again these sample scores can be presented in a Cartesian plane between two principal component score axis.

6.1.1 Determining Principal Components to Separate Sample Groups

A clearly defined separation of sample groups in the PCA scores plot is useful for determining hidden variables. This may be achieved by manually searching through the different principal components to determine which variables best distinguish one group of samples from another.

Figure 6.1 illustrates the PCA results found for two sets of sample spectra. In this experiment 10 spectra were taken from an image of a Viagra tablet and a further 10 spectra were taken from a similar placebo tablet. It would be expected on the basis of sample scores with respect to one or more principal components that these spectra could be separated into the relevant tablet image groups.

As can be seen from the scores plot in figure 6.1 (a) the sample groups are clearly defined by their PC1 score. Sample spectra taken from the Viagra tablet image present positive PC1 scores. In contrast, sample spectra taken from the placebo tablet show negative PC1 scores.

On closer examination of the loadings plot in figure 6.1 (b) it would appear that the ion at *m/z* 475.3 accounts for a large proportion of the variance between the samples. This ion presents a positive PC1 loading which would indicate that this variable may be found at elevated levels in the Viagra tablet samples and represents the protonated molecule of sildenafil(1-[4-ethoxy-3-(6,7-dihydro-1-methyl-7-oxo-3-propyl-1*H*-pyrazolo[4,3-*d*]pyrimidin-5-yl)phenylsulfonyl]-4-methylpiperazine citrate)) which is the active component of the Viagra tablet. Graphical representation of the ion intensities recorded for this ion across both groups of sample data (figure 6.1 c) shows that this is indeed the case.

This simple representation illustrates the benefits of PCA in defining specific ions of interest. Whilst in this experiment the two groups of spectra are shown to be separated completely, with the high levels of mass spectral complexity found in biological tissue data, this is rarely the case. A more likely scenario would be a complex scores plot, in which the sample groups are less clearly defined. Moreover as the number of sample groups investigated rises or where the tissue types are highly biologically related, the level of overlap between group scores may increase significantly.

The principal components indicate the ions associated with the largest degree of variance between all samples rather than those accounting for the largest variance between defined sample groups. As such, there is currently some ambiguity surrounding which principal components to concentrate on in determining ions of interest in this application. Clearly, if the wrong principal components are selected, this produces problems in determining ions which may be specific to or elevated in a certain image region or tissue type. Part of this chapter is aimed at investigating a novel approach of interpreting PCA scores plots such that predictions can be made with regards to which principal components are likely to best separate the sample groups.

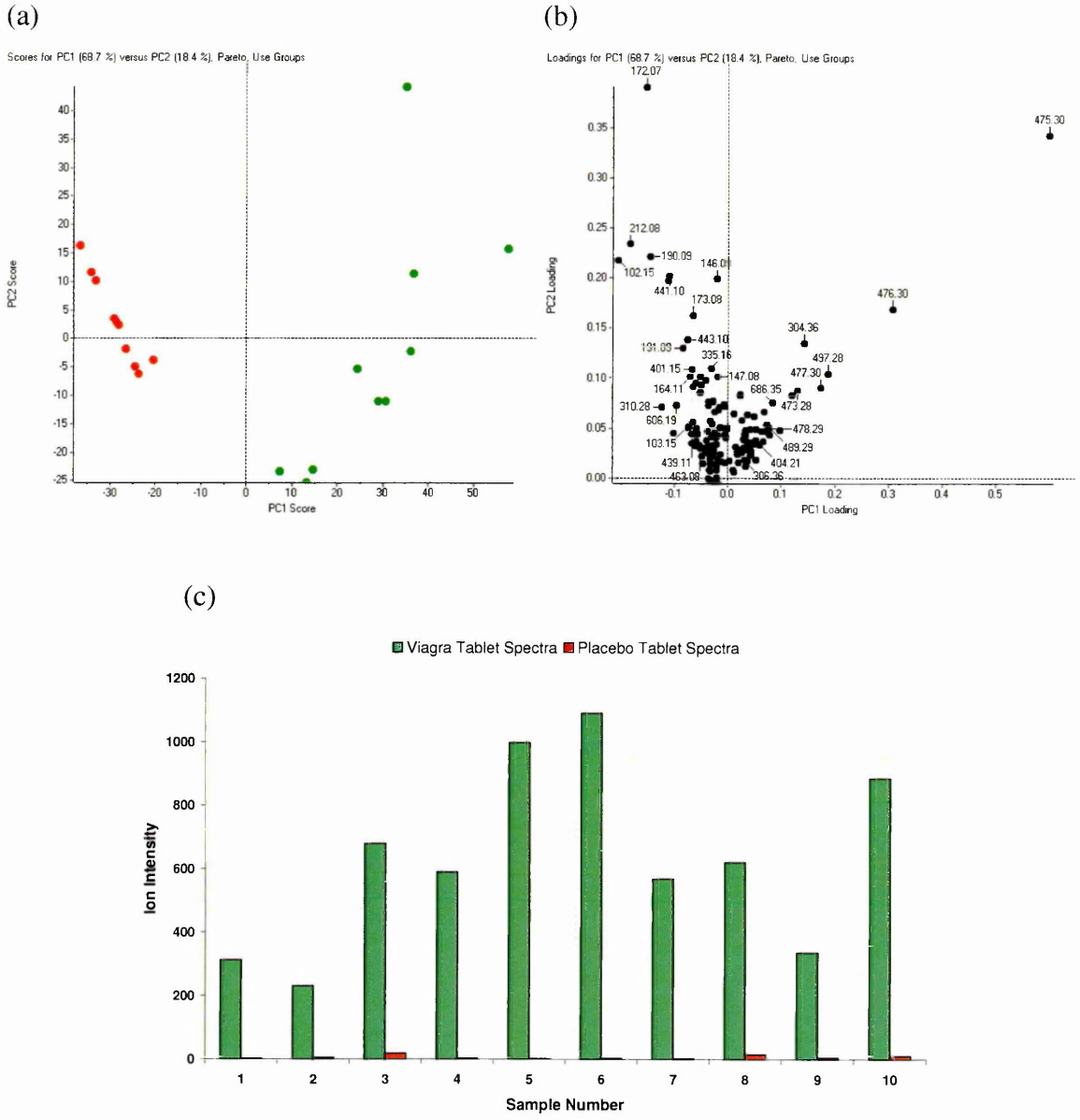

Figure 6.1 PCA of Viagra and Placebo Tablet Data

The PCA scores plot (a) shows clear separation of the sample groups. Viagra tablet (green) spectra uniformly present highly positive PC1 scores and placebo tablet (red) spectra uniformly present highly negative PC1 scores. This would indicate that in the loadings plot (b), ions showing highly positive PC1 loadings would be found at elevated levels in the Viagra tablet (green) spectra.

The graph (c) representing the ion intensities for the *m/z* 475.30 ion across both Viagra and placebo tablet spectra clearly shows that this ion is highly elevated in Viagra tablet spectra in comparison to placebo tablet spectra.

6.1.2 Data Pre-processing for Statistical Image Data Evaluation

As well as the innate complexity of biological systems data, the MALDI-MS imaging process is found to generate unwanted complexities of its own. These relate to the induced experimental errors addressed in chapter 5 of this thesis.

The introduction of experimental error may not only prove to invalidate images, but can also in some circumstances have negative effects on statistical evaluation of the data as well. This effect is less prevalent in cases where spectral patterns vary significantly, for example in defining differences between highly distinctive tissue types. In the determination of small scale changes in spectral pattern however, PCA may prove inadequate in resolving sample groups in the presence of other more extreme variants (such as variability introduced during the experimental process).

A particular instance in which this problem may become relevant is in the analysis of a drug treated tissue. Whilst a relatively uniform tissue would predict that the spectral pattern may remain relatively constant throughout the sample, the presence of a pharmaceutical compound ought to change the spectral pattern sufficiently that drug treated regions can be easily defined using PCA. Clearly, in consideration of the low concentrations of pharmaceutical compound that may be present, the change in spectral pattern would be quite small. With the addition of experimentally induced sample variability (such as variation in matrix coverage) it is possible that this small change in the spectral pattern might not be apparent in PCA results.

This problem may seem of little importance in evaluating drug distribution study data, with PCA not being required when the analyst has prior knowledge of the compound being analysed. The issue, in this instance, does not relate to defining sample groups for the purpose of distinguishing a single unknown variant as described before, but rather to finding the separation of groups based on a known variant such that ions of correlated variance can be determined. This approach may find application in determining a correlated distribution of other compounds in the tissue. These compounds may be drug metabolites, or perhaps more importantly, may be related to changes in the tissue instigated by the presence of the administered compound (i.e pharmaco-dynamic markers)

The second part of this chapter is aimed at assessing the benefits of post-acquisition data pre-processing (as investigated in chapter 5 of this thesis) for the purpose of revealing more information in the PCA.

6.2 Materials and Methods

6.2.1 Materials

The use of PCA in distinguishing ions of interest from MALDI-MS image data has been assessed using data derived from a rat brain sagittal tissue section MALDI-MS image data set. This sample was chosen due to the diverse yet fundamentally similar nature of this tissue type.

Brain tissue exhibits distinction between grey and white matter. The grey matter, consisting primarily of neuron cell bodies; glial cells; capillaries; and short nerve cell processes, is responsible for processing, relaying and re-routing of sensory and motor stimulus in order to create response. White matter consists of myelinated nerve cell processes and is responsible for communication between the grey matter regions. Due to the high level of communication between white and grey matter, these different tissue types are locally inter-related and many regions of the brain contain both white and grey matter in some form. In these experiments the aim is to determine differences in lipid distributions throughout the brain tissue.

Assessment of the effects of data pre-processing for PCA was carried out on data derived from an indirect MALDI-MS image of hydrocortisone treated porcine skin. This sample was chosen due to the relative homogeneity of the tissue to assess whether PCA would be capable of defining drug treated regions of the tissue from untreated regions of the tissue.

The methodology used in preparing the sample for MALDI-MS analysis as well as the method used in extracting the data for PCA is explained below.

6.2.1.1 Sample Preparation of the Sagittal Rat Brain Section

The rat brain sagittal tissue section MALDI-MS image data was provided by a colleague, Paul Trim, of the Sheffield Hallam University Biomedical Research Centre.

To prepare the sample for MALDI-MS image analysis the brain tissue was removed from the rat using standard procedures. The tissue was snap-frozen in liquid nitrogen cooled isopentane immediately after excision and was then stored at -80°C prior to sectioning.

Sagittal sectioning of the brain tissue was performed using a Leica CM1550 cryostat (Leica Microsystems, Wetzlar, Germany). Sections were produced at 12 µm thicknesses in the absence of embedding medium under a cryostat operating temperature of -18°C. The sections were thaw mounted onto disposable aluminium plates in preparation for ethanol washing and matrix application.

Washing of tissue sections was carried out in order to reduce tissue salt content by immersion of the sample plate in several gradients of ethanol. The samples were subject to 30 second washes in 50:50, 70:30 and 90:10 ethanol:water solutions, followed by a final immersion in pure ethanol solvent.

All images were run at 100 µm resolution with a laser power of 30% using a beta test version of the Applied Biosystems/MDS Sciex 'Dynamic Pixel' imaging mode as described in chapter 2 of this thesis.

6.2.1.2 Sample Preparation of the Drug Treated Porcine Skin

The hydrocortisone treated porcine skin image data was derived from a sample presented in chapter 3 of this thesis. The sample preparation methodology and data acquisition parameters are defined in chapter 3 of this thesis.

6.2.2 Methods

Sample spectra were obtained directly from image data to evaluate the potential of PCA in determining ions of interest from within MALDI-MS image data sets. A method of determining the principal components that best define sample groups was evaluated and the results of the PCA were assessed against their correlation with the relevant ion images.

6.2.2.1 Extracting Sample Spectra for PCA

In selecting sample spectra for PCA, the o-MALDI server imaging software was used to define pixel co-ordinates from with the image file.

A total of 10 pixel spectra were selected at random from each of 6 defined tissue regions of the brain sagittal section image. The brain regions examined were the cerebral cortex; the hippocampal formation; the grey cerebellar cortex; the corpus capsulum; the thalamus; the ophthalmic bulb and the white cerebellar cortex.

From the hydrocortisone treated porcine skin image data a total of 10 pixel spectra were selected randomly from within the drug treated region of the tissue. A further 10 pixel spectra were randomly selected from within the untreated region of the tissue.

Analyst QS software was then used to select the defined pixel spectra from the image-file data. The pixel spectra were saved as text files for further use in PCA.

6.2.2.2 Principal Components Analysis

All PCA was carried out using a beta test version of the Markerview™ statistical analysis package (Applied Biosystems/MDS Sciex, Ontario, Canada). Text spectra were imported using a mass tolerance of 0.1 amu and a minimum response of 4.0 ion counts. A mass window of 500-1000 amu was used to reduce interference of matrix on the results of the PCA. PCA was carried out using pareto scaling and the principal component scores and loadings calculated for the data were exported into Microsoft Excel for further analysis.

6.2.2.3 Separation of Sample Groups Based on PCA Scores

The key to determining variants that might be specifically related to a group of samples is to ensure the best separation of groups in the PCA scores plot. In determining the ideal principal component values to plot to allow the best separation of sample groups in a scores plot, the PCA scores for each principal component have been investigated.

The use of conventional statistical methods in determining grouping of sample scores is hindered by the fact that these approaches require that within each sample group a normal distribution of values should be observed. Preliminary investigation of the PCA scores of sample groups showed that a normal distribution was rarely present within the data. As a result experiments have been carried out to assess a new method of determining principal components that provide the best separation of sample groups.

In these experiments the separation of the sample groups has been assessed by looking at the difference in average score for each group versus the standard deviation of the scores within each group. This has been done for all the sample group scores with respect to each separate principal component. The principal components providing the greatest difference in mean score between groups as well as the lowest level of deviation from the mean score within a single group ought to define the principal components which most clearly define the sample groups.

For the best separation of sample groups to occur, the distance between the group mean scores ought to exceed the standard deviation of the scores within each group. Clearly if the standard deviation of scores within a group was to be greater than the distance between group mean scores, overlap of sample groups in the scores plot would be observed. It is unlikely however, in the context of these experiments that complete separation of groups would occur. As these samples are heavily related in many aspects, a certain degree of overlap will most likely be found.

To minimize the degree of overlap between sample groups, principal components chosen to display the data should be those which provide the most positive response in relation to the spread of group mean scores versus the deviation of scores within the group.

For each group of samples the mean PCA score was calculated. The standard deviation of scores within each sample group was also calculated. The average standard deviation of all the group scores was calculated and this was then subtracted from the standard deviation of the group mean scores. This was repeated for the group PCA scores for each principal component.

6.2.2.4 Determining Latent Variables in MALDI-MS Image Data

The information gathered in evaluation of the separation of sample groups based on PCA score was used as a means of selecting principal components to define ions that best distinguish between the groups of sample spectra. The ions which were found to account for the largest degree of variation between the two sample groups were selected and used in creating ion images to demonstrate the potential of PCA in selecting ions of interest from MALDI-MS image data.

6.2.2.5 *Assessment of Data Pre-processing for PCA*

In comparing the effects of normalisation on the results of PCA, the image data from the hydrocortisone treated porcine skin tissue was used. PCA results are compared for the raw data versus data normalised using the ion species specific normalisation procedure illustrated in chapter 5 of this thesis.

In this experiment the aim was to determine first of all whether PCA was capable of grouping spectra taken from treated and untreated regions of the tissue and secondly whether it was capable of defining the hydrocortisone related ions as accounting for the variance between sample groups.

Several sample spectra were taken from the hydrocortisone treatment area of the image and several sample spectra were taken from the untreated tissue regions of the image. PCA was carried out before and after ISS normalisation and the results were compared.

6.3 Results

6.3.1 Determining Ions of Interest by PCA

PCA has been evaluated in its ability to determine ions of interest within data taken from a MALDI-MS image of a rat brain sagittal section.

The separation of sample groups based on evaluation of PCA scores was carried out. In this experiment the sample groups were defined by grey or white matter regions of the brain. The results are shown as a graphical representation in figure 6.2. From this evaluation it would appear that PC1 is the only viable principal component capable of clearly defining the two sample groups. Looking at the distribution of the sample scores for each group with respect to each principal component (figure 6.3), it would appear that the calculations used do indicate the separation of groups quite clearly. Based on these data it is thought that this method of assessing the separation of groups of data on PC scores may be useful in determining the optimum principal components to plot.

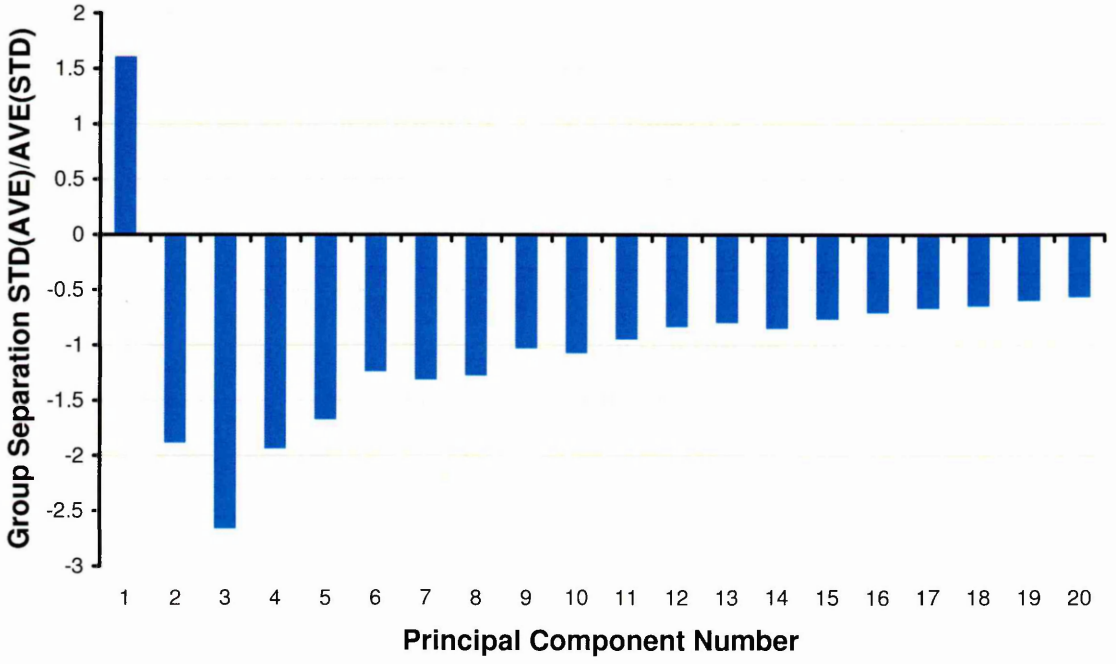

Figure 6.2 Principal Components Separating Sample Groups

From the results shown it would appear that PC1 provides the most positive response in separating the groups of sample spectra taken from the grey and white matter regions of the brain tissue section image.

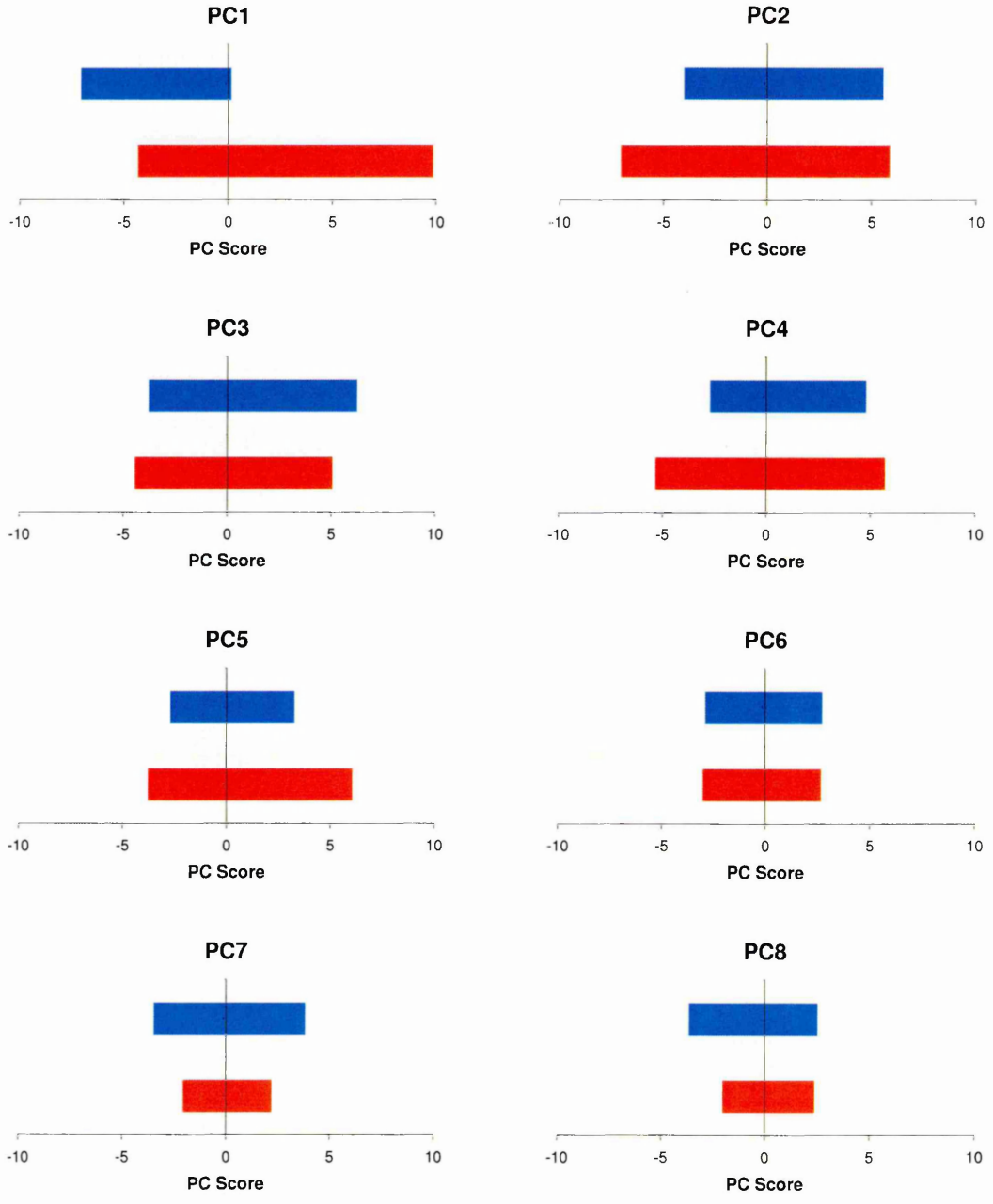

Figure 6.3 Assessing Separation of Groups by PC Score Range

The range of the PC scores within each group of sample spectra are shown for PC1 to PC8. The range of PC scores for the grey matter sample spectra are shown in red and the range of PC scores for the white matter sample spectra are shown in blue. From these data it can be seen that PC1 scores provide the greatest degree of separation of these two groups of data, as predicted by the results of the calculations presented in figure 6.2.

6.3.2 Determining Latent Variables in MALDI-MS Image data by PCA

The PCA scores and loadings plots from this analysis are shown in figure 6.4. From the scores plot it is clear to see the distinction between grey and white matter regions of the brain in relation to the PC1 score. Sample spectra taken from the grey matter regions of the brain have a predominantly negative PC1 score and sample spectra taken from the white matter regions of the brain have a predominantly positive PC1 score. Using this information to interpret the loadings plot shown in figure 6.5, it may be assumed that ions presenting a negative PC1 loading will present elevated abundance in the grey matter regions of the brain. In contrast, ions present a positive PC1 score ought to be elevated in white matter regions of the brain. The two ions which appear to be accounting for the highest level of variance between the grey and white matter spectra are *m/z* 734.57 (predicted to be elevated in grey matter) and *m/z* 788.62 (predicted to be elevated in white matter).

The ion images presented in figure 6.6 represent the distribution of the two ions (*m/z* 734.57 and *m/z* 788.62) which appear to be accounting for the greatest degree of variance in ion signal between the grey and white matter regions of the brain. From these images it is clear that the PCA has been successful in defining ions which correlate with elevated signals in the respective regions of the brain.

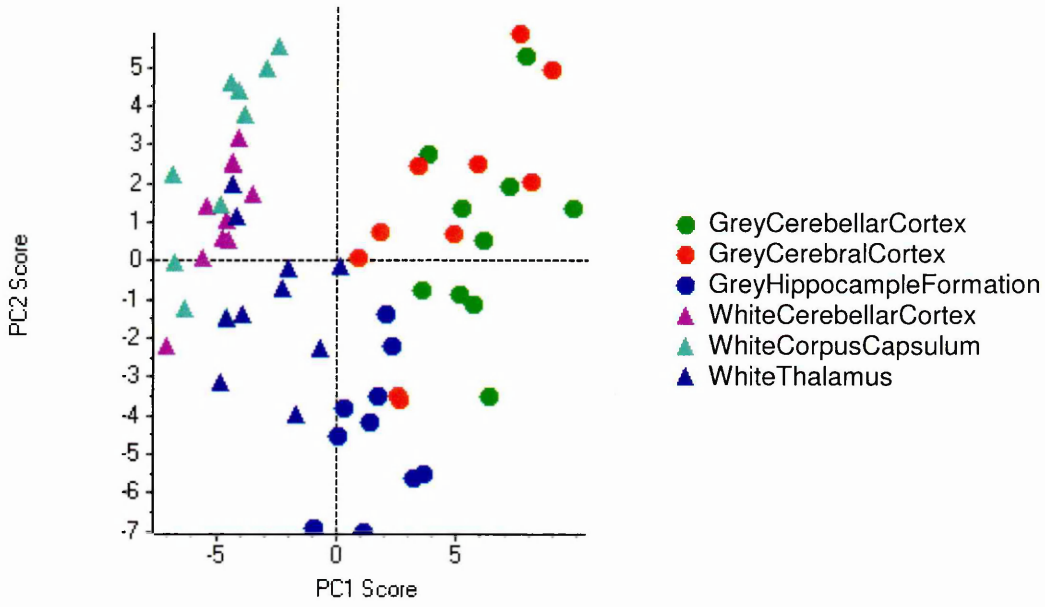

Figure 6.4 Principal Components Scores Plot for the Brain Image Data

The principal components scores plot shows clear separation of the sample spectra taken from the grey and white matter regions of the rat brain image on the PC1 axis. Grey matter sample spectra present predominantly positive PC1 loading whist white matter sample spectra present a predominantly negative PC1 loading.

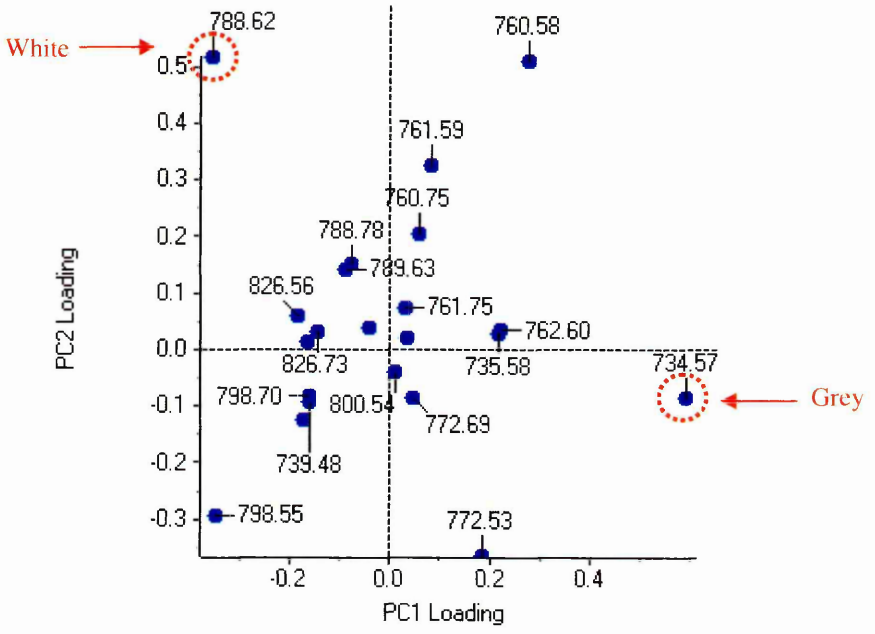

Figure 6.5 Principal Components Loadings Plot for the Brain Image Data

The principal Components loadings plot indicates the influence of each ion in the principal components. As the separation of the sample spectra was found to be related to PC1 score, PC1 loadings of the ions are used for defining ions of interest. The grey matter sample spectra presented predominantly positive PC1 in the scores plot, therefore it may be assumed that ions presenting a positive PC1 loading would be elevated in the grey matter regions of the brain. As white matter sample spectra presented a predominantly negative PC1 loading, it may be assumed that ions presenting a positive PC1 loading would be elevated in the white matter regions of the brain. Ions which appear to be accounting for the largest degree of variance between the grey and white matter sample spectra are indicated.

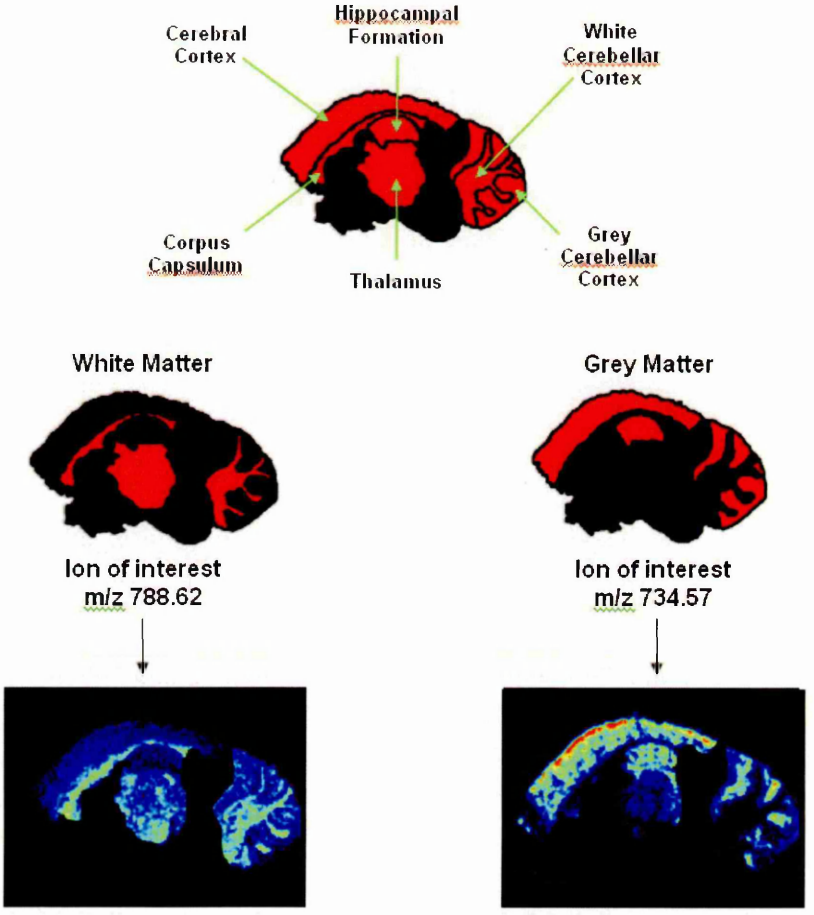

Figure 6.6 Distribution of Ions of interest in the Rat Brain Sagittal Section

Schematic diagrams of the brain show the areas from which sample spectra were selected. These are separated in to the grey and white matter regions defined by the PCA. The images of the distribution of the ions accounting for the largest degree of variance between grey and white mater regions are displayed. The ions are found to present elevated in the corresponding regions of grey and white matter.

6.3.3 Assessment of Hydrocortisone Treated Skin MALDI-MS image

In the following experiment the ion which may be thought to account for the largest degree of variance by PCA was hydrocortisone, the protonated molecule of which exists at *m/z* 363.2. PCA was carried out on the raw and ion species specific (ISS) normalised data to determine what effect this normalisation procedure had on the results of the PCA, both in terms of sample grouping in the scores plot and in defining hydrocortisone as a variant between the sample groups.

6.3.3.1 Evaluating Separation of Sample Groups by PCA

The separation of sample groups based on evaluation of PCA scores was carried out for both the raw and ISS normalised hydrocortisone data. The results are shown as a graphical representation in figure 6.7. The results obtained for the raw and ISS normalised data are identical. This would indicate that ISS normalisation does not distort MALDI-MS image data. From these evaluations it would appear that PC3 is the only viable principal component capable of clearly defining the two sample groups. Based on these data further evaluation of the effects of ISS normalisation on PCA results has been carried out using plots of PC3 versus PC1.

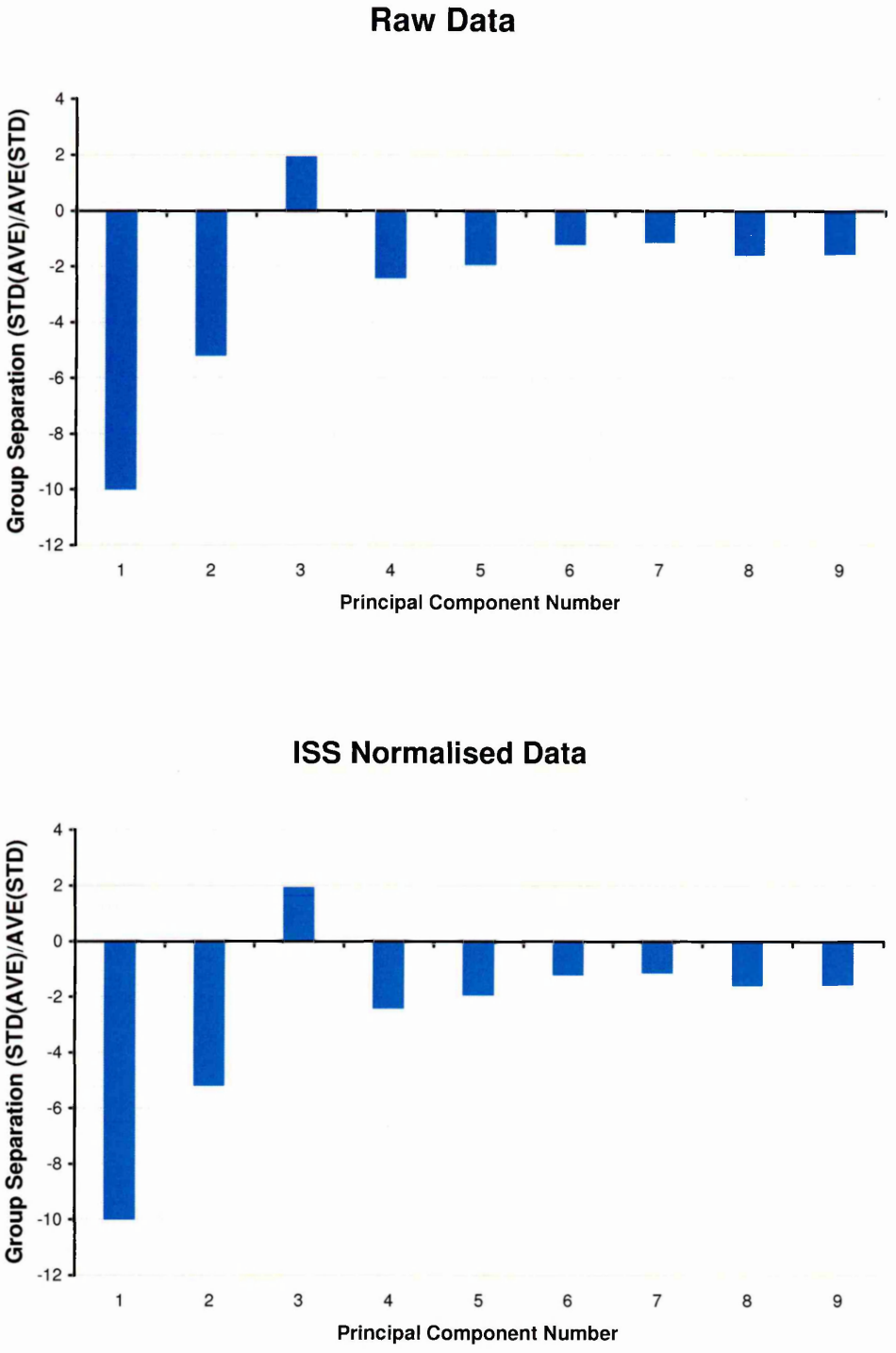

Figure 6.7 The Effects of ISS Normalisation on Sample Grouping

Sample grouping appears to be unaffected by ISS normalisation. This may further validate that MALDI-MS image data is not negatively affected by this type of normalisation.

6.3.3.2 *Assessing the Effects of ISS Normalisation on PCA Results*

The effects of ISS normalisation on PCA results are shown in figure 6.8. As predicted by the calculations carried out to determine the effects of ISS normalisation on sample grouping, samples appear to maintain a similar group configuration in the PCA scores plots both before and after ISS normalisation.

The PCA loadings plots for the raw and ISS normalisation may initially appear to be quite different. For the raw data, all ions present a positive PC1 loading. The ions are divided by positive and negative loading in relation to PC3. The PCA results obtained from the ISS normalised data produced a loadings plot where the ions appear to have been grouped in clusters.

Raw Data

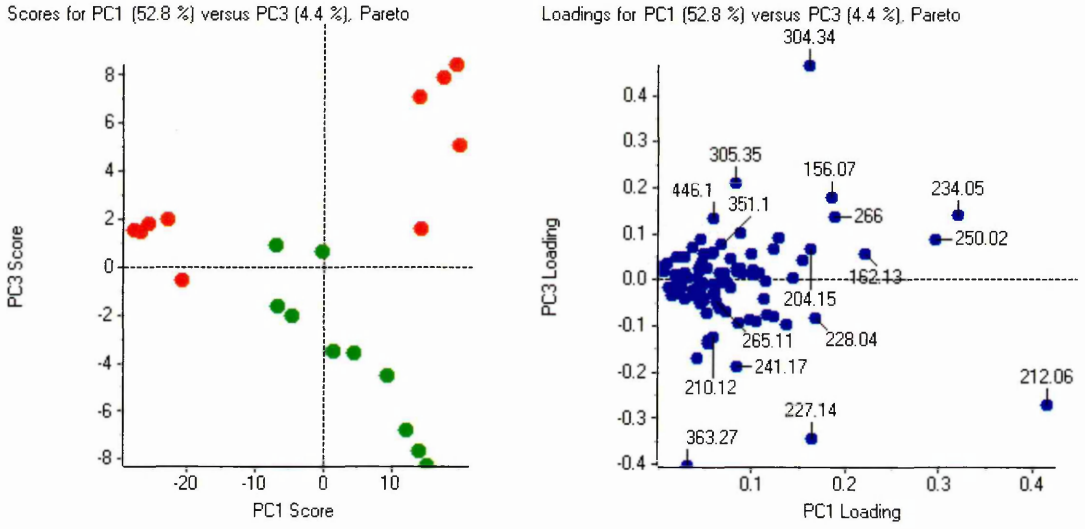

ISS Normalised Data

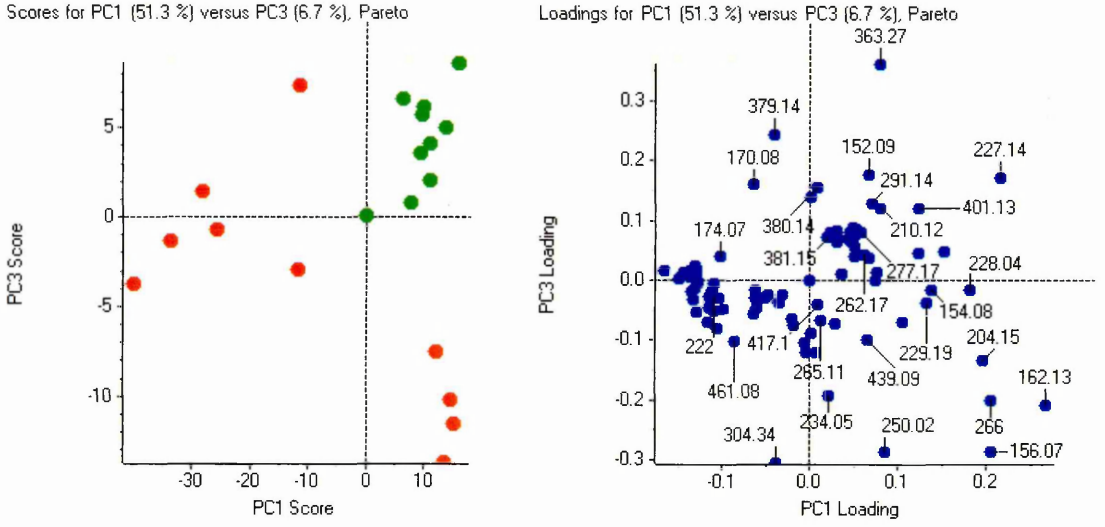

Figure 6.8 The Effect of ISS Normalisation on PCA Results

The PCA scores and loadings plots are shown for PC1 versus PC3, as PC3 was found to provide the best separation of sample groups based on PCA scores. The PCA results indicate that ISS normalisation has little effect on sample grouping as predicted by the results presented in figure 6.7. ISS normalisation does, however significantly alter the loading of ions with respect to each principal components. After ISS normalisation grouping of ions in the loadings plot may also be observed.

6.3.3.3 *Extracting Useful Information form PCA*

The loadings plots of the raw and normalised data have been used to determine ions which may be present at elevated levels in the drug treatment region of the skin image (i.e. in areas where hydrocortisone is most abundant). Ions whose distribution correlates with the distribution of hydrocortisone ought to be found in a similar position of the loadings plot as the molecular ion of hydrocortisone (*m/z* 363.2). Figure 6.9 highlights the areas on each of the loadings plot where these ions may be found.

In assessing the PCA results from the raw and normalised data, it can be seen that the same ions are found to correlate with hydrocortisone distribution irrespective of whether normalisation is carried out or not. This would indicate that prior normalisation of data is not essential for successful PCA.

The only difference observed in these data is that in the PCA loading plot generated from the raw data *m/z* 228 distribution appears to correlate with hydrocortisone distribution. As *m/z* 228 is the potassium adduct of the matrix, it appears that the only effect that ISS normalisation prior to PCA has is the removal of matrix interference from the PCA results. Figure 6.10 shows the MALDI-MS images of the distribution of the protonated molecule of hydrocortisone at *m/z* 363.27 as well as the images of the distribution of ions *m/z* 152.09 and *m/z* 291.14. There is a remarkable similarity between the distribution hydrocortisone and the distribution of these ions through out the sample.

(a)

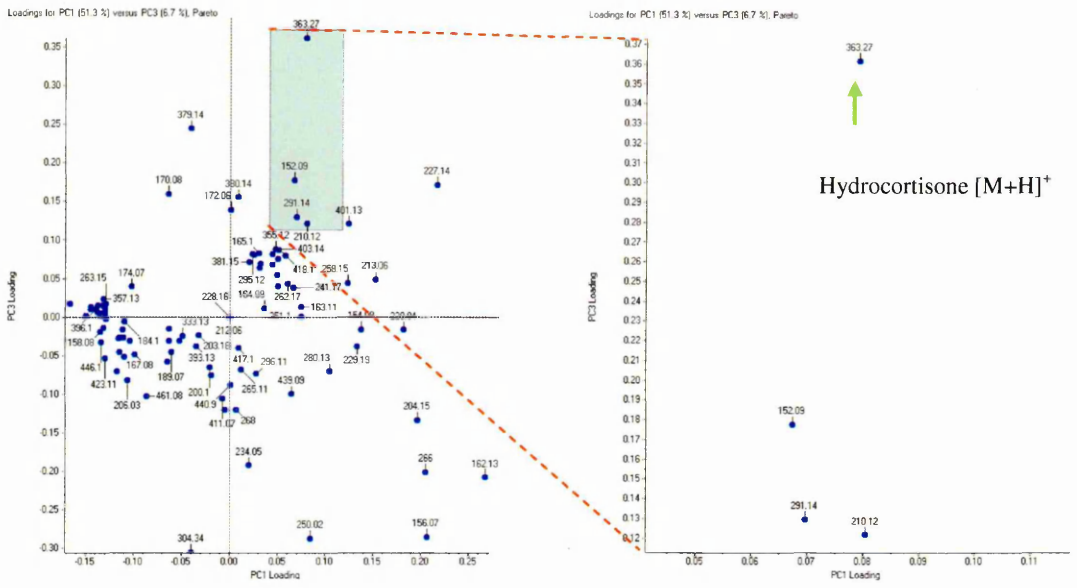

(b)

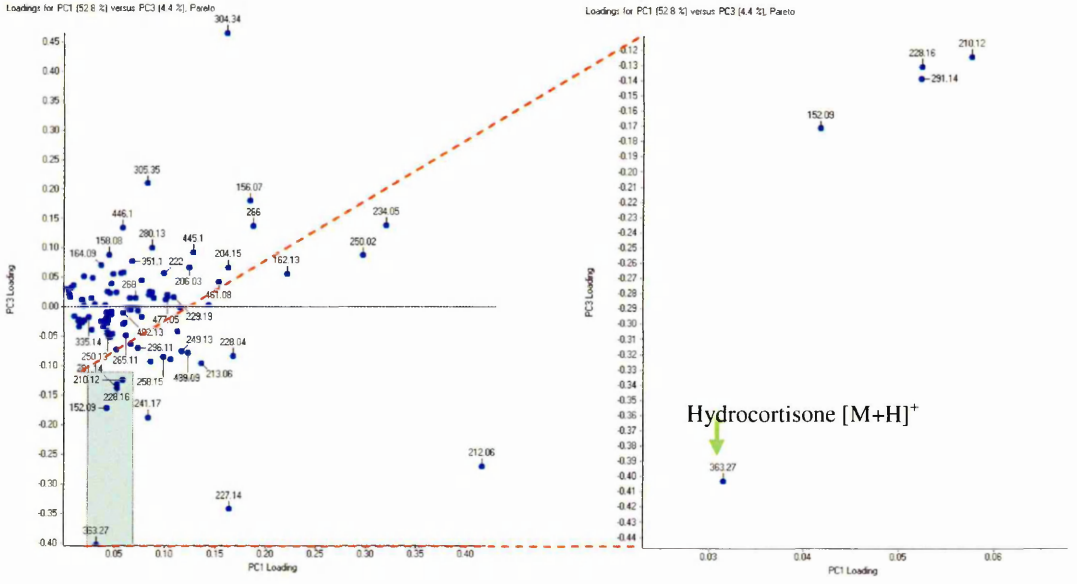

Figure 6.9 Selecting Ions of Interest by PCA

Ions of interest in this experiment are those which may be related to the presence of hydrocortisone in the sample. Ions that are localised around the molecular ion of hydrocortisone (*m/z* 363.27) in the loadings plot are likely to have a similar distribution throughout the sample.

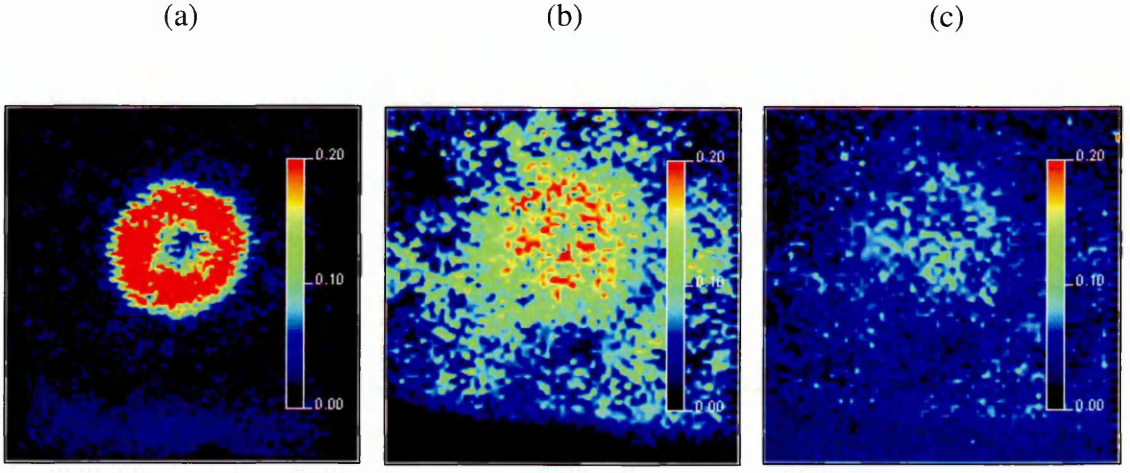

Figure 6.10 Images of Ions of Interest Selected by PCA

Images of the distribution of (a) the molecular ion of hydrocortisone at *m/z* 363.27, (b) *m/z* 152.09 and (c) *m/z* 291.14 are shown as normalised against the relevant matrix ions species. Both ion *m/z* 152.09 and ion *m/z* 291.14 show a similar distribution to hydrocortisone.

6.4 Conclusions

Principal components analysis has been shown to be a useful tool in reducing the amount of data to be searched when determining ions of interest from MALDI-MS image data. PCA was successful at defining ions which may account for differences in lipid distributions between the grey and white matter regions of the brain.

Evaluation of the effects of data normalisation as a data pre-treatment step before PCA showed that it may not necessarily be a required step in defining ions of interest in MALDI-MS image data. PCA was still successful in determining ions which correlated with the distribution of hydrocortisone in the treated skin samples, and the ions indicated were the same as those found when PCA was carried out on ISS normalised data. Although the PCA scores and loadings plots looked different for the raw versus ISS normalised data, the sample grouping calculations for each principal component turned out to be identical for raw and normalised data.

6.5 References

1. McCombie, G., Staab, D., Stoeckli, M. & Knochenmuss, R., 2005. Spatial and spectral correlations in MALDI mass spectrometry images by clustering and multivariate analysis. *Analytical Chemistry* **19**, pp 6118-6124.

2. LAMBERTO, M. and SAITTA, M., 1995. Principal component analysis in fast atom bombardment-mass spectrometry of triacylglycerols in edible oils. *Journal of the American Oil Chemists' Society,* **72**(8), pp. 867-871.

3. SKROBOT, V., CASTRO, E., QUIOV.R., PEREIRA, R.C., PASA, V., NYAM.D. and FORTES, I.P., 2007. Use of Principal Component Analysis (PCA) and Linear Discriminant Analysis (LDA) in Gas Chromatographic (GC) Data in the Investigation of Gasoline Adulteration. *Energy Fuels,* **21**(6), pp3394-3400.

4. GOVORUKHINA, N.I., REIJMERS, T.H., NYANGOMA, S.O., VANDERZEE, A.G.J., JANSEN, R.C. and BISCHOFF, R., 2006. Analysis of human serum by liquid chromatography–mass spectrometry: Improved sample preparation and data analysis. *Journal of Chromatography A,* **1120**(1-2), pp. 142-150.

5. Jolliffe, I. T. Principal Components Analysis. (2002). *2nd Edition.* USA. Springer.

CHAPTER 7

Conclusions and Suggestions for Future Work

7. Conclusions and Suggestions for Future Work

The evaluation of the high repetition rate laser produced some interesting results with regards to the laser beam profile. In contrast to the expected Gaussian profile, a speckled beam profile was observed. Nitrogen lasers are conventionally applied in MALDI-MS imaging experiments and also have a speckled laser profile. However, rather than a static speckle pattern, as is observed with the Nd:YAG laser, the nitrogen laser naturally modulates the light pattern such that the hot spots (i.e. high energy areas of the laser spot) are moved around within the laser spot.

Applied Biosystems/MDS Sciex have overcome the static speckle pattern profile problem by altering the imaging software such that the laser spot moves around in a figure of 8 within each image pixel. This method, known as 'dynamic pixel image mode' has significantly improved the sensitivity of the Nd:YAG laser. The only problem found with the dynamic pixel imaging mode is that there is a limitation on the resolution of images that can be acquired. As the image resolution approaches 50 μm, the ion signals observed become extremely low. Clearly as the pixel size becomes smaller than the laser spot size, laser movement is inhibited.

Bruker Daltonics (Massachusetts, USA) have an alternative solution to the sensitivity issues of Nd:YAG lasers. They have developed the Smartbeam™ laser which has the characteristics of the Nd:YAG laser (i.e. high laser energy, long laser lifetime and high repetition rates) combined with the performance of the nitrogen laser.

In this thesis a method has been developed in which the laser profile of an Nd:YAG laser is modulated by simply moving/vibrating the fibre optic feed. This not only enhances sensitivity of the Nd:YAG laser, but also allows imaging at resolutions higher than 50μm. Further work needs to be carried out to determine the exact limitations for image resolution, but based on the results observed so far it is thought that resolutions <20μm are attainable. However, this would be highly dependant upon the abundance of the analyte(s) being observed.

Direct and indirect imaging methods have been evaluated for the analysis of different compounds and tissues. The solvent assisted indirect imaging approach was found to be useful in cases where analytes were difficult to analyse directly form the tissue. In this case it was the skin tissue that was difficult to analyse due to poor matrix crystalisation on the skin surface.

This indirect imaging approach may also be useful in instances where there is a high level of ion suppression occurring within a sample. Selectively extracting the target compound(s) out of the tissue containing the suppressant ought to allow for a more sensitive analysis.

Sample preparation has been proven to be an important factor in MALDI-MS image analysis, where the analysis of the active metabolite of the prodrug AQ4N (AQ4) was found to be dependant upon the pH of the matrix.

Both chapters 2 and 3 illustrate the importance of optimisation of the sample preparation procedure and show how this should be specifically tailored toward tissue type as well as the properties of the target compound(s).

The method of ion species specific normalisation appears to hold potential as a resolution to the many variables observed in MALDI-MS image data. The method appears to be able to simultaneously resolve variation in ion signals associated with the distribution of salts and matrix crystals throughout tissue sections. Additionally this method resolved spectrum to spectrum changes in the ion intensity scale, a feature previously attributed solely to total ion count normalisation.

It was thought that ISS normalisation may be a useful means of pre-treating data prior to statistical analysis. In chapter 6, principal components analysis of ISS normalised image data is compared with the PCA results observed from the raw data. In contrast to the expected findings (i.e. a much clearer interpretation of the hyperspectral data) it was found that ISS normalisation of data prior to PCA had little effects other than to remove matrix interference from the data.

In consideration of the assessment of ISS normalisation in chapter 5 this is possibly not so remarkable, as ISS normalisation out-performed both single ion count and total ion count modes of normalisation in each area assessed. One interpretation of this result is that ISS normalisation provides reduction in the variability that can distort ion images, but that ISS normalisation does not significantly alter the actual relationships between ion intensities within the image spectra.

The results presented in this thesis draw to a number of interesting conclusions from which further research may be carried out. In terms of the findings of the evaluation of the high repetition rate laser, it is suggested that further research should be carried out with regards to the use of adapting the laser for use in static imaging mode by incorporation of a vibrating mechanism to vary the speckle pattern in the profile of the laser.

The method of ion species specific normalisation may be of particular benefit to MALDI-MS imaging. It is suggested that further evaluation should be carried out to ensure that the normalisation process is not affected by different levels of ion suppression between the protonated molecule and sodium and potassium adducts.

Principal components analysis appears to hold potential for use as a tool for determination of biomarkers within tissues. It would be useful to validate this method with a comparison between healthy and diseased tissue (e.g. tumour and normal tissue).

CHAPTER 8

Publications and Posters

8 Publications and Posters

Publications

1. ATKINSON, S.J., PRIDEAUX, B., BUNCH, J., WARBURTON, K.E. and CLENCH, M.R., 2005. Imaging matrix assisted laser desoprtion ionisation mass spectrometry: A new technique for drug distribution studies. *Chimica-Oggi-Chemistry Today,* **23**, pp 5-8.

2. PRIDEAUX, B., ATKINSON, S.J., CAROLAN, V.A., MORTON, J. and CLENCH, M.R., 2007. Sample preparation and data interpretation procedures for the examination of xenobiotic compounds in skin by indirect imaging MALDI-MS. *International Journal of Mass Spectrometry,* **260**(2), pp243-251.

3. ATKINSON, S.J., LOADMAN, P.M., SUTTON, C., PATTERSON, L.H., and CLENCH, M.R., 2007. S Examination of the distribution of the bioreductive drug AQ4N and its active metabolite AQ4 in solid tumours by imaging matrix-assisted laser desorption/ionisation mass spectrometry. *Rapid Communications in Mass Spectrometry,* **21**(7), pp 1271-21276.

4. EARNSHAW, C.J., ATKINSON, S.J., BURRELL, M.M. and CLENCH, M.R., 2007. Matrix assisted laser desorption ionisation mass spectrometry imaging. *Metabolomics, Metabonomics and Metabolic Profiling,* Ed. Griffiths, W., RSC Publishing, Cambridge. pp 234-251.

Poster and Oral Presentations

1. Investigating Hydrocortisone Uptake in Porcine Tissue Using a Solvent Extraction Method for Indirect Analysis by Imaging MALDI MS. Poster presentation at the American Society for Mass Spectrometry Annual Conference, San Antonio, Texas, US, 2005; the Royal Society of Chemistry Analytical Research Forum, Plymouth, UK, 2005; and the British Mass Spectrometry Conference, York, UK 2005.

2. Examining the Distribution of the Bioreductive Drug AQ4N and its Metabolites in Treated Tumours by Imaging MALDI-MS. Poster presentation at the American Society for Mass Spectrometry Annual Conference, Seattle, US, 2006; and the Internaltional Mass Spectrometry Conference, Prague, Czech Republic, 2006.

3. Examining the distribution of the bioreductive drug AQ4N and its cytotoxic metabolite AQ4 in solid tumours by Imaging Matrix Assisted Laser Desorption/Ionisation Mass Spectrometry. Poster presentation at the Sanibel Imaging Symposium, Sanibel Island, Florida, US, 2007; and the Royal Society of Chemistry Analytical Research Forum, Glasgow, UK 2007.

4. Optimising MALDI-MS Imaging for Small Molecule Pre-Clinical Applications. Oral presentation at the British Mass Spectrometry Conference, Edinburgh, UK, 2007.